

COMPUTATIONAL AND EXPERIMENTAL STUDY OF TRAILING VORTICES

by

Heehwan Lee

Dissertation submitted to the Faculty of the
Virginia Polytechnic Institute and State University
in partial fulfillment of the requirements for the degree of
DOCTOR OF PHILOSOPHY
in
Aerospace Engineering

APPROVED:

J. A. Schetz, Chairman

J. F. Marchman, III

C. H. Lewis

A. K. Jakubowski

W. E. Kohler

April, 1983
Blacksburg, Virginia

ACKNOWLEDGEMENT

First of all, the author wishes to express his deep gratitude to his advisor, Dr. J. A. Schetz. In addition to the enlightening guide and constant encouragement without which this work would never be completed, he taught the author the importance of seeing the woods. The author is still lost among the trees, but the lesson is clearly inscribed on his mind.

The author is greatly indebted to each member of his advisory committee: to Dr. J. F. Marchman whose early works on vortices pointed the right direction, to Dr. C. H. Lewis whose numerical courses were valuable experiences, to Dr. A. K. Jakubowski for his expert help in experimental work, and to Dr. W. E. Kohler who showed the beautiful world of partial differential equations.

Help came from everywhere. Especially from D. Pelletier on numerical matters, from S. Swaminathan and M. Kim on computational matters, and from F. Shelor, R. Frazier and G. Stafford on mechanical matters.

Special thanks are due to Dr. and Mrs. Kelley for their affection for my undescribable family.

TABLE OF CONTENTS

	<u>Page</u>
LIST OF TABLES	v
LIST OF FIGURES	vi
NOMENCLATURE	ix
I. INTRODUCTION	1
II. EXPERIMENTAL STUDY OF THE NEAR-WAKE	13
2.1 Apparatus and Instrumentation	13
2.1.1 Wind Tunnel	13
2.1.2 Model	14
2.1.3 Probes	15
2.2 Test Procedure	17
2.2.1 Preliminary Study	17
2.2.2 Mean Flow Measurements	18
2.2.3 Turbulent Flow Measurements	23
2.3 Results and Discussion	27
2.3.1 Vortex Center Location	29
2.3.2 Vortex Structure	30
2.3.3 Vortex Age Consideration	35
2.3.4 Axial Turbulent Intensity	36
III. COMPUTATIONAL STUDY OF THE FAR-FIELD	39
3.1 Governing Equations for Mean Motion	41
3.2 Modeling of Turbulent Transport	47
3.3 Numerical Formulation	55

3.4 Results and Discussion	57
IV. CONCLUSIONS	65
REFERENCES	68
TABLES	72
FIGURES	77
APPENDICES	
A: Calibration of the Yaw-Head Probe	120
B: Program Listing for Yaw-Head Data Reduction	130
C: Experimental Data in The Near-Wake	136
D: Program Listing for Far-Field Computation	168
VITA	172
ABSTRACT	

LIST OF TABLES

	<u>Page</u>
1. Location of Vortex Centers	72
2. Vortex Core Radius	73
3. Maximum Tangential Velocity	74
4. Axial Velocity at Vortex Center	75
5. Axial Turbulence Intensity at Vortex Center	76

LIST OF FIGURES

	<u>Page</u>
1. Structure of Trailing Vortices	77
2. Model Description	78
3. Coordinate System for Experimental Study	79
4. Description of Yaw-Head Probe	80
5. Arrangement of Hot-Wire Anemometer System	81
6. Location of Vortex Centers	82
7. Typical Axial Velocity Profiles	83
8. Typical Radial Velocity Profiles	84
9. Typical Tangential Velocity Profiles	85
10. Asymmetry in Axial Velocity Profiles at $x/c = 3$...	86
11. Symmetry in Axial Velocity Profiles at $x/c = 3$	87
12. Effect of Downstream Distance on Tangential Velocity for $V_\infty = 30$ fps	88
13. Effect of Downstream Distance on Tangential Velocity for $V_\infty = 95$ fps	89
14. Effect of Downstream Distance on Tangential Velocity for $V_\infty = 220$ fps	90
15. Effect of Angle of Attack on Tangential Velocity for $\alpha = 5^\circ$	91
16. Effect of Angle of Attack on Tangential Velocity for $\alpha = -10^\circ$	92
17. Effect of Imprecise Center Measurement	93

18.	Core Radius vs. Vortex Age	94
19.	Maximum Tangential Velocity vs. Vortex Age	95
20.	Axial Velocity at Center vs. Vortex Age	96
21.	Maximum Tangential Velocity/Axial Velocity at Center vs. Vortex age	97
22.	Axial Turbulence Intensity Profiles at $x/c = 6$	98
23.	Axial Turbulence Intensity Profiles at $x/c = 3$	99
24.	Axial Turbulence Intensity Profiles for $V_\infty = 220$ fps	100
25.	Axial Turbulence Intensity Profiles for $V_\infty = 95$ fps	101
26.	Typical Mean Axial Velocity Profiles by Hot-Wire ..	102
27.	Axial Turbulence Intensity at Center vs. Downstream Distance	103
28.	Maximum Tangential Velocity Correlation by Iversen (Ref. 7)	104
29.	Axial Velocity Decay for $V_\infty = 95$ fps with Constant Eddy Viscosity Coefficient	105
30.	Radial Velocity Decay for $V_\infty = 95$ fps with Constant Eddy Viscosity Coefficient	106
31.	Tangential Velocity Decay for $V_\infty = 95$ fps with Constant Eddy Viscosity Coefficient	107
32.	Axial Velocity Decay for $V_\infty = 95$ fps with Axially Varying Eddy Viscosity Coefficient ...	108
33.	Tangential Velocity Decay for $V_\infty = 95$ fps with Axially Varying Eddy Viscosity Coefficient ...	109

34. Effect of Eddy Viscosity Coefficient	
on W_{max} Decay for $V_\infty = 95$ fps	110
35. Axial Velocity Decay for $V_\infty = 220$ fps	111
36. Tangential Velocity Decay for $V_\infty = 220$ fps	112
37. Effect of Reynolds Number on W_{max} Decay with	
Axially Varying Eddy Viscosity Coefficient ...	113
38. Growth of Core Radius	114
39. Axial Turbulence Intensity Decay for $V_\infty = 95$ fps ..	115
40. Axial Turbulence Intensity Decay for $V_\infty = 220$ fps .	116
41. Decay of Effective Eddy Viscosity	117
42. Axial Shear Stress Decay for $V_\infty = 220$ fps	118
43. Tangential Shear Stress Decay for $V_\infty = 220$ fps	119
A-1. Yaw Coefficient vs. Pitch Coefficient:	
New Calibration Result	124
A-2. Yaw Coefficient vs. Pitch Coefficient:	
Old Calibration Result (from Ref. 18)	125
A-3. Yaw Coefficient vs. Yaw Angle for Zero Pitch	126
A-4. Pitch Coefficient vs. Yaw Angle for Zero Pitch	127
A-5. Total Pressure Coefficient vs. Yaw Angle	
for Zero Pitch	128
A-6. Static Pressure Coefficient vs. Yaw Angle	
for Zero Pitch	129

NOMENCLATURE

AR	aspect ratio
b	wing span
c	mean aerodynamic chord of lifting surface
C	eddy viscosity coefficient
C'	constant for axially varying eddy viscosity coefficient
C_D	dissipation coefficient
C_θ	non-isotropic eddy viscosity coefficient
C_p pitch	pitch coefficient
C_p static	static pressure coefficient
C_p total	total pressure coefficient
C_p yaw	yaw coefficient
e	r.m.s. output in hot-wire anemometry
E	d.c. output in hot-wire anemometry
f	function of vortex Reynolds number by Iversen
G	pitch factor for hot-wire
H	yaw factor for hot-wire
k or TKE	turbulent kinetic energy
L	dissipation length scale
p_s	static pressure
p_t	total pressure
p_1, p_2, p_3, p_4, p_5	pressure readings from yaw-head probe
q	freestream dynamic pressure in wind tunnel

r, θ, x	radial, circumferential and axial coordinate used in computational study
Re_c	Reynolds number based on c
S_x	swirl number
w_{max}	maximum tangential velocity
S	linearization factor in hot-wire anemometry
S_x	swirl number
u, v, w	axial, radial and tangential velocity used in computational study
v	mean velocity vector
v_e	effective cooling velocity for hot-wire
v_x, v_y, v_z	axial, horizontal and vertical velocity used in experimental study
v_∞	freestream velocity
x, y, z	axial, horizontal and vertical coordinate used in experimental study

GREEK LETTERS

α	angle of attack of lifting surface
Γ_o	circulation at large r
δ	angle of attack of yaw-head probe
ε	isotropic eddy viscosity (kinematic)
ε_e	effective viscosity (kinematic)
ε_θ	non-isotropic eddy viscosity (kinematic)
ζ	a similarity variable in Lamb vortex
ϑ	flow pitch angle

ι	hot-wire yaw angle
κ	hot-wire pitch angle
ν	laminar kinematic viscosity
ξ	circumferential vorticity
ρ	density of air
σ_k	a Prandtl number for TKE
σ_θ	non-isotropy constant
ϕ	bank angle of yaw-head probe
Φ	dissipation function in TKE equation
ψ	flow yaw angle
Ψ	stream function

SUPERSCRIPTS

'	fluctuating quantity
—	Time average of fluctuating quantity

SUBSCRIPTS

r	partial differentiation w.r.t. r
x	partial differentiation w.r.t. x
θ	pertaining to non-isotropic eddy viscosity

Chapter I

INTRODUCTION

Vortices, which have been a classical part of the study of fluid dynamics, occur in a wide variety of conditions: in the flows past sharp-edged bodies set at angles to streams, in hurricanes and tornadoes, in bathtubs and pipes, and even in galaxies. The flow mechanisms leading to the formation of various kinds of vortices are well explained, if not always quantitatively. For example, in the so-called leading-edge vortices, the flow separates near the leading edge of a slender delta wing at incidence forming a free shear layer, which curves upward and inboard and eventually rolls up into a core of high vorticity. The fascinating and sometimes highly hazardous features of vortex cores have been widely observed. The main source of the ghastly destructive power of a tornado is very strong updrafts produced by very low pressure in the core, whereas in the core (eye) of a hurricane a calm and peaceful atmosphere exists. Some vortices break down as soon as they emerge, while others display amazing persistence. In calm air, vortices trailing from wing-tips can be found a few miles behind an aircraft (it was reported that wing-tip vortices persisted up to 15 miles behind the C5A aircraft). But, the most surprising feature of vortices is their ability to

self-induce extremely high rotational velocities (30,000 RPM is not unusual) in their cores.

Although all these are sufficient to make vortices one of the most interesting phenomena in nature, the apparent lack of applications has deterred many detailed investigations. However, since the introduction of the "Jumbo Jet" class of aircraft in the early seventies, some serious effort¹ has been directed to investigations of trailing vortices in order to minimize the wake hazard to smaller aircraft. Also leading-edge vortices are gaining detailed attention, since the obvious advantages of a delta wing over a conventional wing for future aircraft were recognized.

This work is a study of the behavior of tip vortices such as trail from wings or control surfaces on airplanes, surface ships or undersea vehicles. Before stating the scope of the problem in more detail, it would be preferable to have a general idea of the flow field and to review some important studies conducted so far in this area.

It is by now customary to divide a wing-tip vortex into three downstream regions: roll-up, plateau, and decay region (Fig. 1). The roll-up region lies immediately behind the wing tips where the vorticity shed by the lifting surface

¹ So far two symposiums were held: "Symposium on Aircraft Wake Turbulence" held in Seattle in 1970 (Ref. 31), and "NASA Symposium on Wake Vortex Minimization" held in Washington, D.C. in 1976 (Ref. 32).

rapidly rolls up to produce a pair of trailing vortices which move slowly inboard, until at a distance of several chord lengths downstream, they begin to travel parallel to the free stream. Wake character is fully elliptic and vortex structures are changing very rapidly because of self-induced distortions. The whole process of roll-up usually takes less than three span-lengths. The plateau region of typically 10 span lengths follows, where the vortex has a nearly constant structure or undergoes very small decay. The highly 3-dimensional vortex structure in the roll-up region now turns nearly axi-symmetric, and it displays "solid body rotation" type behavior inside the core and " $1/r$ potential" type behavior outside. The existence of this region was confirmed only in the mid-seventies by Ciffone and Orloff (Ref. 1) in water tunnel tests. Farther downstream, the wake assumes a fully parabolic character, and vortex decay is approximately inversely proportional to the square root of downstream distance. Here, caution must be taken in that the decay in the plateau region is slower than the far-field decay only in the functional sense, not in absolute magnitude. Turbulence is believed to be in equilibrium in this region and therefore similarity is expected to hold, whereas the characteristics of the plateau region may be at least partly due to nonequilibrium turbulence.

Vortex bursting or breakdown can occur in any of these three regions when vortices are subjected to strong disturbances such as gusts, very high atmospheric turbulence, or abrupt maneuvers of the vehicle. However, the main dispersion mechanism in a calm atmosphere is the inherent instability of vortex pairs. The resulting breakdown occurs at a great distance downstream in most cases. The vortex cores recede and draw together in a wavy pattern until they connect at the nearer points to form a train of vortex rings, and the wake quickly disintegrates into a harmless turbulent state. In his remarkable work, Crow (Ref. 2) was able to explain the cause of the instability and calculated the preferred wavelength (by atmospheric turbulence) as about 8.6 times the distance between the vortices.

Another point of importance in describing trailing vortices is that they are self-induced, unlike the externally-excited swirl flows such as swirling jets and propeller wakes. For those swirling flows, turbulence enhances the decay, and the wake length is usually less than one hundred times the wake width. The situation is totally different for trailing vortices in that turbulence decays very rapidly and the wake can persist around ten thousand times the wake width in a calm atmosphere. Even the rotational velocity which is the main reason why some

workers, if not all, have assumed these two flows to be similar, takes different profiles. For ordinary swirl, the radial build-up of circumferential velocity takes about the same length required for decay, whereas in vortices $1/r$ decay is so slow that the wake width is more than ten times the core size. Quite a lot of analyses have been produced for swirling jets and propeller wakes. However, direct adaptation of these to the trailing vortex problem is not possible due to the different physics involved, even though some of the ideas developed in those works give helpful suggestions.

In the study of trailing vortices the near-wake (roll-up and plateau region) received earlier attention, because any analysis of the far-field would require a complete description of the near-wake to provide initial conditions. The roll-up process itself has never been described in detail except by experimental simulation, since the highly elliptic and complicated flow characteristics precludes simple theoretical approaches. However, once roll-up is completed the rotational velocity profiles have been estimated with moderate accuracy by several methods, of which the most frequently used is the early work by Betz (Ref. 3). His theory is based upon the conservation equations for inviscid, two-dimensional vortices and relates

the circulation in the fully developed vortex to the span loading on the wing. As more experimental data were accumulated, it became desirable to relate the vortex structure backward to the span loading. This led to the so-called inverse-Betz method of Rossow (Ref. 4) which is based on the same basic equations and assumptions as the direct-Betz method. However, at about the same time, Donaldson (Ref. 5) showed that the swirl velocity distributions calculated by the direct-Betz method compared most favorably with measurements, and Bilanin and Donaldson (Ref. 6) extended the Betz model to include the axial velocity in the wake, thereby coupling the wake structure to both wing lift and drag distributions. So far, it has not been determined which gives the better result, but both have shown that the roll-up process can be approximated quite well by inviscid analyses, even though excessively high velocities are often predicted inside the core as a result of the inviscid assumption.

Various wing geometries such as the shape of tip and the aspect ratio were found to have significant influences on vortex formation. Further, wake character is seriously affected by Reynolds number and atmospheric turbulence throughout the entire flow field. However, these effects have not been studied except in a few scattered experiments, and so far comprehensive descriptions are not available.

When this limited theoretical success along with the extreme difficulty of actual flight tests in the near-wake is considered, experimental simulation in ground facility remains as the sole means to accurately describe an individual vortex pair in the near-wake. This is especially true for the present problem since, in addition to the inherent complexity in the near-wake, the flow field is expected to be highly 3-dimensional due to the small aspect ratio considered. So far, most investigations of trailing vortices have been associated with high aspect ratio wings, and few studies have been directed toward small aspect ratio situations.

The near-wake behavior of the vortices trailing from low aspect ratio lifting surfaces mounted on either side of a larger, non-lifting, streamlined strut was investigated in a wind tunnel. The simulation of trailing vortices by small-scale model testing in wind tunnels and towing tanks presents a severe problem, since the history of vortices is known to be quite sensitive to Reynolds number in most cases. The present test program was designed to obtain as high a Reynolds number as possible in a given size facility, by using a large-scale model of only a part of a complete vehicle configuration. The portion selected is representative of control surfaces on a typical vehicle. The rest of the vehicle was "simulated" by mounting the

model on the floor of the wind tunnel. At a tunnel speed of 220 fps, this gives an Re_c (Reynolds number based on mean aerodynamic chord) of 1.5×10^6 , which is much greater than those in the usual tests with complete vehicle configurations in wind tunnels and towing tanks. Tests were also conducted at $Re_c = 2.1 \times 10^5$ and 6.7×10^5 to clarify the important question of Reynolds number dependence.

The experiment is divided into three types of measurements: (1) flow visualization study by a tuft grid, (2) mean flow properties by a five-port, yaw-head probe, and (3) axial turbulence intensity by a straight, hot-wire anemometer. Due to the complex flow mechanism expected, special efforts were made in the selection and calibration of the probes as well as in refinements of the test procedures.

Another problem of major concern is the persistence or downstream variation of the far-field, that is, the decay region. The experimental verification in this region is far more difficult since flight testing, which is at best crude, is the only way of data acquisition. Some theoretical approaches have been made, but most works have been directed toward data interpretation through parameter studies. Ciffone and Orloff (Ref. 1) achieved reasonable success in this, and confirmed the existence of the plateau region.

However, it was Iversen (Ref. 7) who finally succeeded in correlating the maximum swirl velocity data obtained in ground-based facilities and in flight into a single curve (cf. Fig. 28), using a correlation function from the solution of a similarity differential equation with a variable eddy viscosity model.

The problem of axial flow is of equal importance as the rotational flow, even though it has drawn less attention. In most studies, axial velocity has been assumed to be constant to avoid the treatment of the pressure, which is usually quite cumbersome. Although the detailed mechanism is not known, the existence of axial flow is believed to have some effect on the vortex stability. For example, Hall (Ref. 8) argued that the magnitude of the axial velocity decides the onset of vortex breakdown for a given circulation. Another problem of concern is the usual velocity deficit in the core confirmed by experiment in direct contrast to the velocity excess prescribed by inviscid theory. In the absence of viscous effects, fluid particles entering the core should be accelerated, since the pressure is lower in the core. The role of viscosity was studied by Batchelor (Ref. 9) who showed that the viscosity indeed causes an axial velocity deficit in the far-field. However, Moore and Saffman (Ref. 10) studied axial flow in the near-wake and concluded that it is inside the core where

viscosity plays a major role, and viscous effects are almost negligible outside the core. They confined their study to laminar flow, but the situation in turbulent flow is considered to be the same, since predictions of circumferential velocity outside the core using various inviscid methods yield good agreement with experiments even for highly turbulent cases.

The presence of turbulence, which has not been taken into account in classical models of trailing vortices, was found to play an important role in deciding initial conditions for the decay region. The measurements of turbulence intensities in the near wake typically show low intensities outside the cores (about 1%), but maximum values at vortex centers can be more than 10% for high angle of attack cases. These relatively high values of turbulence intensity would normally be associated with high rates of decay that would act against the persistence of the vortices. However, in view of their well-known perseverance, it can only be concluded that the high rotational velocity confines the turbulence to a small region around the center, i.e., the core and leads to rapid decay of turbulence.

Some effort has been made to account for the effect of turbulence in vortex decay by employing an eddy viscosity concept in which turbulent diffusivity is simply assumed to be proportional to molecular viscosity. Although some

improvement was achieved by giving axial variation to the eddy viscosity in an integral approach by Fernandez and Lubard (Ref. 11), it is obvious that radial variation is indispensable to adequately describe both the highly turbulent region in the core and the nearly inviscid outside region at the same time. Iversen (Ref. 12) used a radially varying eddy viscosity model and succeeded in explaining the existence of the plateau region, but axial flow (hence pressure) and turbulent intensities were not treated.

The direct calculation of turbulent shear was tried by Donaldson (Ref. 13) who applied his method of invariant modeling to the decay problem. In fact, he did predict the existence of the plateau region, but the method requires modeling of three turbulent intensities and axial Reynolds stress, and detailed experimental data for these quantities are almost non-existent. Also, axial flow was not included in the analysis.

Flight testing techniques are still very crude and costly, if not impossible in the far-field. A method which is comprehensive enough to describe the whole flow character including axial flow and turbulence, but not too sophisticated as to require unverifiable assumptions or modeling, has to be developed in order to adequately describe the far-field, and this is the main objective in the computational part of the present study. The decay of

an isolated vortex in the far-field was predicted with the axi-symmetric Navier-Stokes equations written in terms of vorticity and the stream function. The equations were parabolized and a simple explicit finite difference scheme was employed. Initial conditions were provided directly by the near-wake experimental data in the form of three velocity components and axial turbulence intensity. Turbulent transport was modeled through the turbulent kinetic energy and a general Prandtl-type representation to give an eddy viscosity. This is the most widely accepted technique for turbulent wake problems, and serves very well for the present problem since the additional required modeling is not great.

To avoid the confusion expected to arise when experimental and computational approaches are described simultaneously, the experimental study of the near-wake will be presented first. It is hoped that this investigation will not only provide realistic insight into the flow mechanisms of wing-tip vortices, but also help set the basis for future studies of this kind.

Chapter II

EXPERIMENTAL STUDY OF THE NEAR-WAKE

2.1 APPARATUS AND INSTRUMENTATION

2.1.1 Wind Tunnel

The tests were conducted in the Virginia Tech 6 ft \times 6 ft subsonic stability tunnel. The facility is of a continuous, closed and single return type, and it has a 28 ft long test section. The airstream has a very low turbulence factor of 1.08 and the tunnel's capability for continuous running allows very long sampling times which is almost a necessity for this type of investigation.

All tests were done in the straight closed test section. Originally, an open test section was designed, since the walls in the closed test section might be too close to the vortices and therefore confine their development enough to change their characteristics. An air scoop was built on the receiving end and a floor section was provided to simulate the hull and serve as a working platform. But, tests produced severe flutter of the air scoop above tunnel speeds of 110 fps, which rendered its use impossible at higher speeds. Besides, tuft grid surveys in both the open and closed test section at lower speeds did not produce any appreciable changes in vortex locations and core sizes, and no further tests were conducted in the open test section.

A Validyne digital barometer (Model DB 99) was used to measure the atmospheric pressure, and the freestream temperature was monitored by a Digitemp temperature sensing probe mounted on the tunnel wall. A Barocel electric manometer was used to read the dynamic pressure from a Pitot-Static tube mounted 10 in. from the wall. During the high speed runs (tunnel speed of 220 fps), a maximum fluctuation of 1 fps was observed. A horizontal and vertical traverse of the empty test section with the yaw-head probe revealed an average variation in the mean velocity of less than 0.5%. The axial pressure gradient was also determined to be negligible throughout the test section.

2.1.2 Model

Figure 2 shows the configuration and the dimensions of the model. Blockage considerations on maximum model cross-sectional area permitted a model 27 in. high. The maximum cross-sectional area was 8% of the test section area, which could be considered large. However, no signs of a blockage problem were observed at any test speed. The aspect ratio of the lifting surfaces was 2.7.

The model was constructed mainly with styrofoam and balsa wood. The strut housed an aluminium box-section, to which an iron tube (3/4 in. × 24 in.) was attached to accommodate

the lifting surfaces. Two styrofoam blocks were glued and shaped except at the trailing edge where balsa wood was used. The strut was bolted to the tunnel floor, using two L-beams which were in turn bolted to the box-section. Two removable lifting surfaces, which were also made of balsa wood (for wing roots and trailing edges) and styrofoam, had slotted pipes inside, and these were attached to the pipe from the strut with hose-clamps. The model was spackled and painted twice with glossy and non-glossy paints to make the surface sturdy enough for the handling and maintenance. It also helped thin tape which was used at all junctures to further assure a smooth final contour adhere better.

2.1.3 Probes

Figure 3 describes the coordinate system used in the experimental study, as well as definitions of the flow pitch (ϑ) and yaw (ψ) angles. A straight, 3-D yaw-head probe manufactured by United Sensor was used to obtain the mean-flow measurements. The probe had a blunted conical nose with five pressure ports as shown in Fig. 4. The probe stem was sufficiently long so as to extend the tip out of any interference caused by the supporting apparatus. The pressure signals were fed to a scanivalve pressure transducer located immediately outside the test section in order to reduce the lag time. The signal was displayed on a digital voltmeter (HP 3476B).

For the axial turbulence intensity measurements, a single-normal hot-wire (TSI-1210) was used. The wire was made of tungsten with a thin platinum coating. This gave the sensors good resistance to the wind load and prevented oxidation. The diameter and length of the wire were 1.5×10^{-4} in. and 0.05 in., respectively. The prong supporting the wire was made of gold-plated stainless steel. Fig. 5 shows the anemometer system. The constant temperature hot-wire anemometer (TSI Model 1050) has a very low noise (0.007% equivalent turbulent intensity) and high frequency response (500 KHz). The voltage output was linearized with the flow velocity by a signal linearizer (TSI Model 1052) to render the measurement more convenient. The advantages and disadvantages of using the linearizer are discussed in Ref. 14. A digital integrating voltmeter (TSI Model 1076) was used for the mean flow quantities and an r.m.s. voltmeter (DISA Model 55D35) served for reading the fluctuating quantities.

It is well known that vortices are extremely difficult to measure with probes, since they may react to the placement of any object in their cores. The interference mechanism and its effect on the accuracy of probing are only poorly understood. However, Mason and Marchman (Ref. 15) found that a small probe moving slowly would not perturb the vortex seriously enough to affect the velocity profiles significantly.

Both the mean and turbulent measurement probes were supported in the wind tunnel by a mechanized traverse stand, which could be moved and positioned to within 0.01 in. horizontally and 0.04 in. vertically.

2.2 TEST PROCEDURE

2.2.1 Preliminary Study

Flow visualization was attempted with a tuft grid to observe the variation in location and size of the vortex cores as a function of lifting surface setting angle and tunnel speed (and thus Reynolds number). The data did not indicate a strong sensitivity to Re_c in terms of location and core size. Although these data are not reported in detail, they served very well later to help find the exact location of the cores, and thus reduce overall run time considerably.

Originally, test speeds were chosen as 20, 95 and 220 fps, following the rationale given in the Introduction, but during the preliminary probing, fluctuations as large as the signal itself were observed at the low test speed of 20 fps, and relatively reliable data could not be obtained until the speed was increased to 30 fps. Further, at the high test speed of 220 fps, severe fluctuations in pressure readings along with vibrations at the tip of yaw-head probe were observed. It was not clear whether these fluctuations came

from tip vibration or from the inherent turbulence of the flow itself. A stiffer mechanical traverse was used for later tests and the situation was alleviated considerably, which showed that the turbulence did not play a major role in producing the fluctuations. As a reference, the axial turbulence intensity around the core at this speed was found to be 4 to 6%. Finally, the test speeds were selected to be 30, 95 and 220 fps.

It was decided to hold positive angle of attack of the lifting surfaces to 5° for fear of possible influence from the tunnel floor. At this angle of attack, the cores were located about 14 in. above the floor. Second angle of attack was chosen to be -10° .

Measurements were made at three stations; 3.5, 7.0 and 10.5 ft behind the trailing edge of the lifting surfaces. The last station corresponded to $x/c = 9$, where x is the downstream distance and c is the mean aerodynamic chord.

2.2.2 Mean Flow Measurements

The yaw-head probe was used to fix the location of vortex centers. Due to the poor repeatability around the centers, and also to the crude spatial resolution of the mechanical traverse in the vertical direction (0.04 in.), it was very difficult to fix the center locations precisely. Therefore, the usual method of zeroing the flow angularities in both

directions was not used. Instead, the simple procedure of tracing the lowest pressure readings from the center hole of yaw-head probe (p_1) was adapted. This was found to be sufficiently accurate. Both horizontal and vertical scans were conducted through each vortex center. The scans usually reached 2 to 4 in. from the center in both directions. Although these were never far enough to reach the free stream or the model centerline to get the whole picture, a scan with 15 points usually took about 90 minutes due to the slow response of the integrating voltmeter and the necessarily slow movement of the probe. For this reason, scans were terminated when all five pressure readings showed relatively small changes.

Treaster and Yocum (Ref. 16) described the calibration procedure for the type of yaw-head probe used in present study, which employs four non-dimensional pressure coefficients. This procedure made it possible to determine the mean flow quantities regardless of the magnitude of the angularity. The calibration procedure introduced by Winternitz (Ref. 17) is, although simpler, valid for large flow angles in one direction only and therefore is not suitable to describe the highly complicated flow field of the present study. Treaster and Yocum suggested that the two angularity coefficients and total pressure coefficient

are essentially unaffected by Reynolds number variation, whereas a measurable change in the static pressure coefficient can be expected. Since the only available calibration at the beginning of this work had been conducted at one speed only (115 fps) in the Virginia Tech 3 ft tunnel (Ref. 18), a calibration check was attempted to verify the above statement and also to decide whether a new calibration would be necessary. The results showed that the static coefficient is hardly affected by Reynolds number variations (cf. Fig. A-6), which is contradictory to the observation by Treaster and Yocom. Another important finding was that the static pressure coefficients taken in the 3 ft tunnel differed significantly from those of stability tunnel, and this was mainly due to the open test section in the 3 ft tunnel.

In any event, it was found that due to the highly 3-dimensional characteristics near the lifting surfaces, some data points were out of the old calibration range. Consequently, a new calibration was unavoidable to describe the flow field with reasonable accuracy. However, individual calibration at each test speed was not necessary due to the insensitivity to Reynolds number variation discussed above, and calibration was done at the speed of 95 fps in the Virginia Tech 3 ft tunnel. The actual flow measurements were, of course, conducted in the 6 ft

stability tunnel and the resulting difference in the static coefficient was accounted for in the data reduction procedure. Instead of using flow pitch (β) and yaw angle (ψ) as practiced by Treaster and Yocom (Ref. 16), probe angle of attack (δ) and bank angle (ϕ) were directly employed during calibration and this resulted in considerable reduction of the amount of work needed not only for calibration but also for data reduction. The procedure and results of the new calibration are discussed in detail in Appendix A, together with the experimental errors involved in the yaw-head measurement.

The data reduction procedure is as follows. First, dimensionless pressure coefficients, C_p pitch and C_p yaw, are computed with five pressure readings.

$$C_p \text{ pitch} = (p_4 - p_5)/A \quad (2.1)$$

$$C_p \text{ yaw} = (p_2 - p_3)/A \quad (2.2)$$

where $A = p_1 - (p_2 + p_3 + p_4 + p_5)/4$. These are used to determine probe angle of attack and bank angle from the calibration curves (Fig. A-1) through 2-dimensional interpolation. These angles are, in turn, used to find the static and total pressure coefficients. Now,

$$p_t = p_1 - A C_p \text{ total} \quad (2.3)$$

$$p_s = p_1 - A (1 + C_p \text{ static}) \quad (2.4)$$

and from the incompressible Bernoulli's equation,

$$p_t - p_s = (\rho V^2 + \rho \overline{V'^2})/2 \quad (2.5)$$

The turbulence term can be neglected as the expected error in the velocity corresponding to such an assumption is approximately 1% for turbulence intensity as high as 14% (Ref. 19). Therefore the magnitude of the total velocity vector is determined as:

$$|V| = \sqrt{2(p_t - p_s)/\rho} \quad (2.6)$$

Further, the relations between the angles involved are given as (cf. Appendix A),

$$\sin\psi = \sin\delta \sin\phi \quad (2.7)$$

$$\tan\vartheta = \tan\delta \cos\phi \quad (2.8)$$

Therefore, the velocity components are:

$$V_x = |V| \cos\vartheta \cos\psi \quad (2.9)$$

$$V_y = |V| \cos\vartheta \sin\psi \quad (2.10)$$

$$V_z = |V| \sin\vartheta \quad (2.11)$$

A computer program was written for this procedure, using the 2-dimensional interpolation subroutine IBCIEU in the International Mathematical and Statistical Libraries (IMSL). The listing is given in Appendix B.

2.2.3 Turbulent Flow Measurements

Axial turbulence intensity was measured with the straight, hot-wire anemometer. A constant temperature anemometer was selected, as it allowed for signal linearization as well as good frequency response. It is well known that the hot-wire signal is very sensitive to the angle between the velocity vector and wire. The following two situations summarize this problem. If the velocity vector lies in the wire-prong plane, the effective cooling velocity past the wire is expressed as,

$$V_e^2 = |V|^2(\cos^2\kappa + G^2\sin^2\kappa) \quad (2.12)$$

where κ is the angle between the normal to the wire and the mean velocity vector, and G is the pitch factor, which is typically small (usually less than 0.2). Now, if the velocity vector does not lie in the wire-prong plane but normal to the wire, the effective cooling velocity is

$$V_e^2 = |V|^2(1 + H^2\sin^2\iota) \quad (2.13)$$

where ι is the angle between the velocity vector and the wire-prong plane, and H can be called the yaw factor, and its usual value is about 1.1 to 1.4. For the present study, if the wire is placed vertically,

$$\kappa = \vartheta \quad (\text{if } \psi = 0) \quad (2.14)$$

$$\iota = \psi \quad (\text{if } \vartheta = 0) \quad (2.15)$$

The situation is reversed when the wire is placed horizontally. Now, if we have a completely axi-symmetric vortex, the flow yaw angle ψ will be nearly zero during a horizontal scan through the center, since radial velocity is very small compared to circumferential velocity. For a vertically placed wire, $\kappa = \vartheta$, and from eqns (2.9) and (2.12),

$$V_e^2 = V_x^2(1 + G^2 \tan^2 \vartheta) \quad (2.16)$$

If we are to assume $V_e \approx V_x$, the associated error is about 0.7% for $\vartheta = 30^\circ$. But if the wire is placed horizontally, $\kappa = \vartheta$, and from eqns (2.9) and (2.13),

$$V_e^2 = V_x^2(1 + H^2 \sin^2 \vartheta) / \cos^2 \vartheta \quad (2.17)$$

And the corresponding error would be at least 31%. Consequently, the wire was placed vertically during a horizontal scan and horizontally during a vertical scan.

Since the signal was linearized, the following approximations were used to obtain axial velocity and axial turbulence intensity.

$$V_x \approx V_e = E/S \quad (2.18)$$

$$\sqrt{\bar{u'}^2} / V_x \approx e/E \quad (2.19)$$

where S is the linearizaton factor, E is d.c. output and e is r.m.s. output.

The errors associated with these approximations were fairly large especially around the vortex centers, since a slightly misaligned scan would produce large flow angles in this region. For instance, flow yaw angles of about 30° were found around the center during a scan at the first axial station ($x/c = 3$) with $V_\infty = 220$ fps, and the corresponding error in axial velocity was estimated to be about 13%.

For all these, the real difficulty in hot-wire probing of vortices lies in the fact that the dimension of a conventional hot-wire is too big compared to the core size of a vortex produced in ground facilities. In the present study a typical core radius is about 0.4 in. which is only about 8 times the wire length, and better resolution is required to properly account for the rapidly changing flow characters in the core. Also, this dimensional problem may explain the axial velocity excess in the core usually measured by hot-wires, in direct contrast to the deficit measured with pressure probes. The wire is subject to severe non-uniformity and therefore, such assumptions as discussed above can not account for the additional cooling effect. Consequently, a velocity excess can be indicated. For these reasons, minimization of hot-wire size is very desirable.

However, this will not alleviate another inherent difficulty, that is occasional fluctuations in r.m.s. readings caused by unsteady movement of the vortex itself. This is especially the problem when probing inside the core, since any slight movement of the vortex would be reflected instantaneously on r.m.s. readings due to the rapidly varying flow characters in this region. For pressure probes, this fluctuation is believed to be damped by slower response, and the problem is not so severe as long as the amplitude of vortex swerving is small. For these reasons, a seemingly stable vortex when measured by a yaw-head may show uncontrollable fluctuations in hot-wire readings, especially when the vortex is not strong. In the present study, occasional fluctuations of 30 to 50% were detected for the high angle of attack case, but repeated fluctuations up to 100% were observed around the vortex centers at $x/c = 6$ and 9 with the low angle of attack, which rendered the turbulent measurements impossible in those cases.

An overheat ratio of 1.8 was used to minimize the probe sensitivity to temperature variation. The elimination of the influence of temperature fluctuation using a calibration curve of voltage output is also a common practice. However, it would be superfluous since the errors discussed above are far greater than those associated with temperature variation.

2.3 RESULTS AND DISCUSSION

Mean flow surveys were successfully carried out at all test conditions with the exception of the low speed case ($V_\infty = 30$ fps) at $x/c = 9$, since the vortex center could not be located accurately due to very poor repeatability. This was believed to be caused by unsteady swerving of the vortex itself at this station, a mild form of which was observed at $x/c = 6$ (cf. section 2.3.1). Repeatability was not always satisfactory, especially near the centers where at least two readings were taken and averaged. Outside the cores, repeatability was good in general. Also the possible influence of probing direction was checked by performing the probing in either direction for some cases, and no significant effect was detected. The results are summarized in Table 1 to 4, and the axial and tangential velocity profiles are fully plotted in Appendix C. Radial velocity profiles are not reported since they showed irregular behavior throughout all the test conditions which is due to their susceptibility to experimental errors. The radial velocity would contain contributions from other velocity components, if a scan was not conducted perfectly along the centerline. Also, the magnitude of the radial velocity is very small compared to the axial or the tangential velocity.

Hot-wire surveys were conducted for all test conditions with $\alpha = -10^\circ$, except for the low speed case at $x/c = 9$, for

which yaw-head probing failed to provide the vortex center location because of vortex swerving. For $\alpha = 5^\circ$, measurements were taken only at $x/c = 3$ since the presence of severe and almost continuous fluctuations in r.m.s. readings at $x/c = 6$ and 9 rendered any measurements doubtful (cf. section 2.2.3). Axial turbulence intensity profiles are plotted in Appendix C, and maximum values at vortex centers are summarized in Table 5. It would be preferable if the extent of experimental errors can be indicated on the plots. However, the increased cooling effect from the swirl is not understood well, and a full investigation would be necessary on this subject alone, before a reasonable error estimation is possible. For this reason, the data was reported with no indication of the extent of errors. Axial velocity data are not reported since they showed very poor agreement with the yaw-head results. This is in contrast to satisfactory agreement reported for propeller swirl in a previous work by the author (Ref. 20), which is another indication of the difficulties involved in experimental study of trailing vortices.

Inviscid theories such as the Betz method can be used to predict the circumferential velocity profiles in the plateau region. However, they usually fail to give an accurate description inside the core. Besides, 2-dimensional type approximations are required which are not compatible at all

with the present model due to the small aspect ratio involved. For these reasons an inviscid analysis was not attempted. Another way to check these results is to utilize the findings of other experimental or correlational studies. So far, the most successful in these is the study by Iversen (Ref. 7), and this is discussed in the next chapter together with the computational results for the far-field.

2.3.1 Vortex Center Location

Table 1 and Fig. 6 describe the location of the vortex centers. Due to repeatability problems as well as the coarse spatial resolution of the traverse used, the errors were estimated to be up to 0.04 in. Definite grouping characteristics emphasized by the circles on Fig. 6, indicate that the path of a vortex is determined essentially by the angle of attack and the downstream distance. For $\alpha = 5^\circ$, there were only slight variations with changes in station. This was consistent with earlier work showing that the vortex travels parallel to the freestream after a distance of several chord lengths downstream. This was also the case for $\alpha = -10^\circ$, except that the alignment occurred more slowly due to greater vortex strength. The effect of Reynolds number variation was evident in that, for instance, the centers were located lower with increasing Re_c for $\alpha = -10^\circ$. No similar effect was found horizontally.

An interesting phenomenon was detected while locating the center at $x/c = 6$, with $V_\infty = 30$ fps and $\alpha = -10^\circ$. The vortex center was observed to swerve about half an inch on a vertical line (see the dotted line in Fig. 6) and when the hot-wire was mounted, the r.m.s. meter showed very unusual behavior. Axial turbulence intensity was about 2% for a while, and then suddenly moved to 10% range and stayed there for several minutes, until it moved down to zero intensity to last for about half a minute. Since the wake width was more than 4 inches, the hot-wire was well inside the vortex and the r.m.s. reading would not register zero intensity unless the flow turned laminar. This seemed to indicate that the flow was going through an intermittent transition which might be the reason for vortex swerving, but a more detailed study would be required for confirmation.

2.3.2 Vortex Structure

Velocity profiles of typical vortices are depicted in Fig. 7 to 9 with the results from horizontal scans at $x/c = 6$ with $\alpha = 5^\circ$. Good symmetry is exhibited and this indicates that the vortices were rolled-up almost completely at this station for all test speeds. However, this was not the case at $x/c = 3$ as evidenced by Fig. 10, where highly asymmetric axial velocity profiles were obtained on the vertical scans. Here, the excess side was closer to the

expected viscous wake behind the lifting surfaces (cf. Fig. 6), which might be one of the reasons for the asymmetry. Further, this asymmetry was not evident in horizontal profiles as can be seen on Fig. 11, which may suggest that the asymmetry of vortex structure during roll-up is mainly in the vertical direction.

Figure 8 serves to provide some insight into the experimental error involved. As mentioned before, the radial velocity would contain contributions from other velocity components, if a traverse was not made perfectly along the centerline. In spite of this, the tangential velocity profiles demonstrated remarkably good behavior at all test conditions (cf. Fig. 12 to 14), i.e., "solid body rotation" inside the cores and $1/r$ "potential" region outside. This is believed to be the result of relatively accurate calibration in angularity. Fig. 9 displays typical tangential velocity profiles. Maximum swirl velocities are seen to be about 0.4 to 0.6 V_∞ and corresponding pitch angles are 20° to 30° . The angularity profiles are almost identical to the corresponding velocity profiles, and they are not reported here.

The effect of Reynolds number variation is quite apparent, in that increasing Re_C corresponds to decreasing axial velocity defect (cf. Fig. 7) and increasing maximum swirl velocity (cf. Fig. 9). Further, this Reynolds number

effect was found to be greater than that of downstream distance, which is exhibited in Fig. 12 to 14 for the tangential velocity profiles at all test speeds. In contrast to its major role in determining vortex location, downstream distance had a minor effect on vortex structure and this has been observed in previous experiments such as conducted by Marshall and Marchman (Ref. 21). This is mainly due to the fact that the roll-up had been already completed at $x/c = 6$ as evidenced by the slight changes in tangential velocity profiles between $x/c = 6$ and 9 shown in Fig. 13 and 14.

Figures 15 and 16 demonstrate the influence of angle of attack on tangential velocity at $x/c = 3$. Only slight increases in maximum swirl velocity and thus in vortex strength, were achieved by doubling the angle of attack. This is at a glance quite surprising since, according to the potential theory, vortex strength should be proportional to lift and hence to angle of attack. The explanation may be that, due to the small aspect ratio of the lifting surfaces, the flow was strongly disturbed by the strut to result in premature flow separation, and this led to earlier onset of stall well before angle of attack of 12° which is the usual stall angle for an infinite wing with the same airfoil section. Also, the discontinuity near the lifting surface root (cf. Fig. 2) could aggravate the situation in the sense

that it might lead to leading edge stall. Further, it might be concluded the influence of small aspect ratio on vortex formation is not direct but through resulting wing characteristics.

Figure 17 illustrates the result of an imprecisely conducted scan at $x/c = 3$ with $\alpha = -10^\circ$. The tangential velocity profile at $V_\infty = 220$ fps shows a very high velocity pointing left at $z = 0$ (cf. Fig. 3). Since the vortex was rotating clockwise due to the negative angle of attack, it is evident that the actual vortex center lay about 0.15 inch higher than the assumed center. However, the axial velocity profile for the same case in Fig. 10 exhibits a maximum defect at about 0.1 in. lower than the assumed center. A similar situation was observed with $\alpha = 5^\circ$ at the same speed and station. This indicates that the maximum axial velocity defect does not always take place at the vortex center, which was also detected by Marshall and Marchman (Ref. 21). An explanation might be that the vortices were still at the beginning of roll-up due to small vortex age, and the vortex structure was highly 3-dimensional. This is also believed to render the measurements of center location inaccurate. The fact that these difficulties happened only in vertical scans strongly supports the conclusion made earlier in this section, that the asymmetry during roll-up is mainly in the vertical direction. Further, this explains why the maximum

swirl velocities at this speed were not much greater than those with $V_\infty = 95$ fps (Fig. 15 and 16), unlike the typical profiles shown in Fig. 9. Since the horizontal scan was made lower than the actual center line, the tangential velocity registered during the scan was lower than it should have been.

Another significant parameter in vortex development is the core radius. However, the values obtained from the horizontal and vertical scans were not consistent with each other, especially for the low test speed at $x/c = 3$ and for all test speeds at $x/c = 9$ (cf. Table 2). The major portion of these errors should be attributed to the coarse vertical resolution of the mechanized traverse. The two values were averaged and plotted against vortex age in Fig. 18. The point at the top right hand corner was considered to be erroneous because of the vortex swerving discussed before. The trend seemed to support the conclusion made by Rorke and Moffitt (Ref. 22), that vortex age is the single most important parameter for vortex growth in the near-wake. This will be discussed next in detail.

One important point to be appreciated here is the smallness of the core sizes. For instance, at $x/c = 6$ with $\alpha = 5^\circ$, the core radius was about 0.32 in. and the corresponding maximum swirl velocity was about 52 fps. Therefore, the rotational speed in the core is more than

18,000 RPM, and this is what really makes the difference between self-induced vortices and externally excited swirl.

2.3.3 Vortex Age Consideration

Rorke and Moffitt suggested the use of vortex age, that is time of flight from wing-tip to the point under consideration, as the single parameter which governs core size, roll-up, peak swirl and mean axial velocity for a given lift coefficient (Ref. 22). Their report concluded that the growth and the decay of vortices are independent of Reynolds number, but are strongly dependent on vortex age. However, observations made by Marshall and Marchman (Ref. 21) indicate that freestream speed has a definite influence on vortex development, especially at high angles of attack, and thus concluded that vortex age is not a self-sufficient parameter for the description of vortex development. In an effort to clarify these uncertainties, measurements of some important parameters are summarized in Table 2 to 4 and plotted against vortex age in Fig. 18 through 21.

The growth of core size is plotted against vortex age in Fig. 18. As discussed before, the trend seems to support the conclusion of Rorke and Moffitt, especially since two different angles of attack did not yield large changes in lift coefficient due to the premature onset of stall (cf. section 2.3.2). However, this trend was not so apparent for

maximum tangential velocities and axial velocities at the center which are shown in Fig. 19 and 20, respectively. Again, the point on the bottom right corner in each plot is erroneous. It is obvious that freestream speed had an increasing influence on maximum tangential velocity and a decreasing influence on axial velocity defect. Furthermore, angle of attack showed increasing effects on both, and in spite of the premature onset of stall, the influence is seen to be as large as that of freestream speed. Another interesting parameter in vortex study is suggested here to be the ratio between maximum tangential velocity and the axial velocity at the center. This parameter can be used to describe the 3-dimensionality of vortex structure. Fig. 21 shows its variation, where the effect of Reynolds number is no longer evident, while angle of attack still shows an increasing influence.

In summary, it can be seen that the role of vortex age as a self-sufficient parameter in vortex study can not be fully supported, which was also the conclusion drawn by Marshall and Marchman (Ref.21).

2.3.4 Axial Turbulent Intensity

Typical profiles of axial turbulence intensity can be observed in Fig. 22. The asymmetry at low speed can be explained as the result of vortex swerving in the vertical

direction at this test condition (cf. section 2.3.1). Otherwise, good symmetry was achieved as evidenced by the profiles at $x/c = 3$ shown in Fig. 23. Maximum intensities of 4 to 10% are observed at the center and the intensities decrease rapidly until they stabilize at around 2% outside the core. The effect of Reynolds number is quite clear and in the direction of a decrease in intensity inside the core, but any effect is not apparent outside. The downstream distance was observed to have little influence on axial turbulence intensity. Fig. 24 is for the high test speed and a slight increase at $x/c = 9$ can be observed. On the contrary, a considerable decrease for $V_\infty = 95$ fps at the same station is shown in Fig. 25, and this suggests that the decay of turbulence already took place at this station due to larger vortex age, whereas the slight increase for the high test speed indicates that the vortex was not fully developed.

The axial velocity profiles obtained with the hot-wire for $\alpha = -10^\circ$ at $x/c = 3$ are shown on Fig. 26, where velocity overshoot is apparent for the high test speed. A quite contradictory situation is exhibited on Fig. 11, where the data was obtained with the yaw-head probe, and definite velocity defects are to be seen for all test speeds. This is believed to be the result of the hot-wire dimension problem which was discussed in section 2.2.3.

Table 5 and Fig. 27 summarize the findings from the hot-wire survey in the form of axial turbulence intensity at the vortex center. Values obtained in different scans display quite acceptable matches (Table 5) in spite of generally poor repeatability around vortex centers, except for $\alpha = -10^\circ$ and $V_\infty = 30$ fps at $x/c = 6$. This could be explained as the result of vortex swerving mentioned before. The average values are plotted on Fig. 27, where the Reynolds number has a definite decreasing influence except for the erroneous point on the bottom right corner. However, the effects of angle of attack and downstream distance are not obvious, if they exist.

Chapter III

COMPUTATIONAL STUDY OF THE FAR-FIELD

In the analysis of trailing vortices, a considerable simplification of the problem can be achieved by neglecting the presence of the conjugate vortex in the vicinity. This concept of an isolated vortex is not valid in the near-wake, since the vortex pair is related to each other by a thin strip of high vorticity (cf. Fig. 1). This is not true any more in the far-field, and each vortex assumes a quite independent and axi-symmetric structure, until the vortex pair is ultimately drawn so close to each other as to result in a breakdown by the inherent instability. However, the wavy deviation of the vortex center from the straight line grows exponentially (Ref. 2), which means that the trace of the vortex center can be safely assumed to be a straight line until just before the breakdown. This justifies the concept of an isolated vortex which is so useful for the far-field decay problem. The presence of atmospheric turbulence is found to be another important factor in the decay problem as well as in the stability problem. However, the accumulated knowledge so far in this field does not shed enough light to initiate an analysis, and the surrounding atmosphere was assumed to be turbulence-free for this analysis.

For all these, the most significant simplification of the problem in a computational sense is achieved by recognizing the parabolic characteristic of the far-field. However, the equations should be parabolized only after the full Navier-Stokes equations with proper representation of the Reynolds stress terms are given, to avoid unwitting omission of small, but important terms, which might be the case if the parabolization is carried out in the laminar sense only.

In most previous analyses (e.g. Ref. 12 and 13), mean axial and radial velocity, u and v , have been assumed to be zero (u is constant for a coordinate system fixed to the wing) to avoid the treatment of the pressure field. The continuity equation becomes trivial with this assumption. The radial velocity is usually so small (at least two orders of magnitude smaller than u or w for most of the flow field) that it might be considered superfluous to include it in the analysis. However, it should be included to treat the axial flow field properly. Another common assumption for fully turbulent flow is that the molecular (or laminar) contributions to the stresses are negligibly small. This is not the case for trailing vortices, since the high rotational velocity concentrates the turbulence in the small core, which results in a rapid decay of the turbulence. Furthermore, the flow field outside the core is nearly turbulence-free once the roll-up is completed.

The turbulent transfer of momentum was modeled through a non-isotropic eddy viscosity with the Prandtl-Kolmogorov hypothesis. A differential equation was derived to compute the turbulent kinetic energy (TKE) and the core radius was chosen to represent the length scale. These will be discussed in more detail later in the chapter when the momentum equations are fully established.

For the computational study, cylindrical coordinates x , r and θ replaced the cartesian coordinates x , y and z used for the experimental study. To simplify the presentation, subscripts are used throughout this chapter to indicate partial derivatives except θ , which is used for non-isotropic eddy viscosity.

3.1 GOVERNING EQUATIONS FOR MEAN MOTION

The steady, axi-symmetric Navier-Stokes equations with all three velocity components are time-averaged to produce the Reynolds momentum equations:

$$\begin{aligned} uu_x + vu_r &= - p_x/\rho + v(u_{xx} + u_{rr} + u_r/r) \\ &\quad - \overline{(u'^2)}_x - \overline{(ru'v')}_r/r \end{aligned} \quad (3.1)$$

$$\begin{aligned} uv_x + vv_r - w^2/r &= - p_r/\rho + v(v_{xx} + v_{rr} + v_r/r - v/r^2) \\ &\quad - \overline{(u'v')}_x - \overline{(rv'^2)}_r/r + \overline{w'^2}/r \end{aligned} \quad (3.2)$$

$$\begin{aligned} uw_x + vw_r + vw/r &= v(w_{xx} + w_{rr} + w_r/r - w/r^2) \\ &\quad - \overline{(u'w')}_x - \overline{(v'w')}_r - 2\overline{v'w'}/r \end{aligned} \quad (3.3)$$

The continuity equations are :

$$u_x + v_r + v/r = 0 \quad (3.4)$$

$$u'_x + v'_r + v'/r = 0 \quad (3.5)$$

The determination of the Reynolds stresses either by direct computation or by appropriate modeling is, of course, the main problem in predicting turbulent flows. For trailing vortices, direct computation was never attempted except by Donaldson (Ref. 13). He adapted his method of invariant modeling to the problem and predicted the existence of the plateau region. However, the applied boundary conditions for the stresses were:

$$\begin{aligned} \text{as } r \rightarrow 0 : \quad \overline{u'^2} &= a_1 + b_1 r^2 \\ \overline{v'^2} &= a_2 + b_2 r^2 \\ \overline{w'^2} &= a_3 + b_3 r^2 \\ \overline{v'w'} &= cr^2 \end{aligned} \quad (3.6)$$

$$\text{as } r \rightarrow \infty : \quad \overline{u'^2} = \overline{v'^2} = \overline{w'^2} = \overline{v'w'} = 0$$

where a's, b's and c are functions of time. The use of these time-dependent coefficients can not be verified experimentally due to the scarcity of accumulated stress data. With the situation as it is, the only reasonable way to proceed would be to employ the most successful idea for a wide range of turbulent problem: the Turbulent Kinetic Energy (TKE) model. For axi-symmetric flow,

$$\begin{aligned}
 -\overline{u'^2} &= 2\varepsilon u_x - 2k/3 \\
 -\overline{v'^2} &= 2\varepsilon v_r - 2k/3 \\
 -\overline{w'^2} &= 2\varepsilon v/r - 2k/3 \\
 -\overline{u'v'} &= \varepsilon(u_r + v_x) \\
 -\overline{v'w'} &= \varepsilon(w_r - w/r) \\
 -\overline{u'w'} &= \varepsilon w_x
 \end{aligned} \tag{3.7}$$

where $k = (\overline{u'^2} + \overline{v'^2} + \overline{w'^2})/2$ is the turbulent kinetic energy, and ε is the eddy viscosity (kinematic) which is a property of the flow, not of the fluid itself. This isotropic eddy viscosity works fairly well when only one Reynolds stress component (usually axial stress, $-\overline{u'v'}$) is of importance, as in the cases of non-swirling wakes and jets. However, experiments and predictions have disputed the isotropy assumption when several shear stresses are of importance and suggested that the eddy viscosity should be direction sensitive. For instance, axial and circumferential ($-\overline{v'w'}$) shear stresses are found to be of the same order of magnitude for flows with swirl (Ref. 23). For the present problem, experiment shows w_r is about an order of magnitude greater than u_r , and the circumferential shear stress would be estimated as much higher than the axial shear stress if the same eddy viscosity were used. Therefore, a modification to the circumferential shear stress model in eqn (3.7) should be in order, and this can

be done by simply introducing a non-isotropic eddy viscosity, ε_θ

$$-\overline{v'w'} = \varepsilon_\theta (w_r - w/r) \quad (3.8)$$

The others remain unchanged. With eqns (3.7) and (3.8), eqns (3.1) to (3.3) now take the form of:

$$\begin{aligned} uu_x + vu_r &= -p_x/\rho + (\nu + \varepsilon)(u_{xx} + u_{rr} + u_r/r) \\ &\quad + 2\varepsilon_x u_x + \varepsilon_r (u_r + v_x) - 2k_x/3 \end{aligned} \quad (3.9)$$

$$\begin{aligned} uv_x + vv_r - w^2/r &= -p_r/\rho + (\nu + \varepsilon)(v_{xx} + v_{rr} + v_r/r - v/r^2) \\ &\quad + 2\varepsilon_r v_r + \varepsilon_x (u_r + v_x) - 2k_r/3 \end{aligned} \quad (3.10)$$

$$\begin{aligned} uw_x + vw_r + vw/r &= (\nu + \varepsilon)w_{xx} + (\nu + \varepsilon_\theta)(w_{rr} + w_r/r - w/r^2) \\ &\quad + \varepsilon_x w_x + (\varepsilon_\theta)_r (w_r - w/r) \end{aligned} \quad (3.11)$$

To avoid direct treatment of the pressure terms, the equations were cast into a vorticity-stream function formulation. With circumferential vorticity component ξ ,

$$\xi \equiv u_r - v_x \quad (3.12)$$

the axial and the radial momentum equations are combined to give:

$$\begin{aligned} u\xi_x + v\xi_r - v\xi/r + 2ww_x/r &= (\nu + \varepsilon)(\xi_{xx} + \xi_{rr} + \xi_r/r - \xi/r^2) \\ &\quad + 2\varepsilon_x \xi_x + 2\varepsilon_r (\xi_r + \xi/2r) \\ &\quad + 2\varepsilon_{xr} (u_x - v_r) + (\varepsilon_{rr} - \varepsilon_{xx})(u_r + v_x) \end{aligned} \quad (3.13)$$

Increased computational efficiency is expected. Further, it is noted that the TKE gradient terms have been dropped. Therefore, the momentum equations would be related to TKE only through the eddy viscosity, if TKE is used in the eddy viscosity model. Now the stream function Ψ is defined as:

$$\Psi_r \equiv ru \quad (3.14)$$

$$\Psi_x \equiv -rv \quad (3.15)$$

Continuity is automatically satisfied, and the definition of vorticity now takes the form:

$$\Psi_{xx} + \Psi_{rr} - \Psi_r/r = r\xi \quad (3.16)$$

Upon parabolization of equations, the flow characteristic in the plateau region has to be carefully examined, since computation should start somewhere in this region for the initial conditions to be supplied by near-wake experimental data. The plateau region displays both an elliptic characteristic as evidenced by the non-equilibrium turbulence, and a parabolic characteristic indicated by slow axial decay in mean velocities. Therefore, parabolization would not seriously distort the result, as long as this non-equilibrium turbulence is taken into account by the turbulence model.

Now, the parabolic characteristic simply states $\partial^2/\partial r^2 \gg \partial^2/\partial x^2$ for all velocity components. This assumption should also be valid for the eddy viscosity, because radial variation of TKE is far greater than axial one. For the stream function, caution must be taken in that, Ψ_{xx} is only a first derivative of the radial velocity and therefore is not negligible in itself. However, with $u \gg v$ and $\partial/\partial r \gg \partial/\partial x$, we can safely assume

$$\Psi_{rr} - \Psi_r/r = ru_r \gg -rv_x = \Psi_{xx} \quad (3.17)$$

and eqn (3.16) is reduced to,

$$\Psi_{rr} - \Psi_r/r = r\xi \quad (3.18)$$

In fact this is same as $\xi = u_r$. Also, ε_{xr} term in eqn (3.13) is small compared to the others since $u_x \approx v_r$ by continuity. With all these, eqns (3.11) and (3.13) are parabolized to give:

$$\begin{aligned} uw_x + vw_r + vw/r &= (v+\varepsilon_\theta)(w_{rr} + w_r/r - w/r^2) \\ &\quad + \varepsilon_x w_x + (\varepsilon_\theta)_r (w_r - w/r) \end{aligned} \quad (3.19)$$

$$\begin{aligned} u\xi_x + v\xi_r - v\xi/r + 2ww_x/r &= (v+\varepsilon)(\xi_{rr} + \xi_r/r - \xi/r^2) \\ &\quad + 2\varepsilon_x \xi_x + 2\varepsilon_r (\xi_r + \xi/2r) + \varepsilon_{rr} \xi \end{aligned} \quad (3.20)$$

Thus are established the momentum relations. Continuity is ensured with eqns (3.14) and (3.15), and related to the momentum equations through eqn (3.18).

3.2 MODELING OF TURBULENT TRANSPORT

Many hypotheses have been proposed and practiced for the evaluation of the eddy viscosity. However, the only model proposed so far for tailing vortices is a mixing length model by Iversen (Ref. 12),

$$\varepsilon = a^2 r^2 |w_r - w/r| \quad (3.21)$$

where a is a constant. This model satisfies the vanishing of the only shear stress he considered ($-\overline{v'w'}$) at both boundaries. However, it gives zero eddy viscosity at the center, and the three normal stresses will become identical at the axis, which is not believed to be the case for axis-symmetric flow (cf. eqn (3.6) and (3.7)). In fact, this is a result of the implied assumption that the turbulence is in local equilibrium, which is the main shortcoming of the mixing length hypothesis. Therefore, it cannot account for the transport and history effects of turbulence and this leads to unrealistic simulations in many cases. It predicts a zero eddy viscosity whenever the velocity gradient is zero. A further disadvantage of the mixing length model is that effects on the turbulence due to buoyancy, streamline curvature or swirl can be accounted for in entirely empirical ways only. However, since the Monin-Oboukhov (Ref. 24) formula was introduced to account for the buoyancy effect, some improvements have been achieved for swirling

flows by correcting the length scale in an analogous fashion, as suggested by Bradshaw (Ref. 25) who first noticed the similarity of the governing equations for turbulent shear flow when either buoyancy or rotation and curvature effects are present. Bradshaw pointed out, however, that this correction should only be applicable when the effect of rotation is small. For the present problem, the non-equilibrium turbulence in the plateau region should be carefully dealt with to justify the parabolization (cf. section 3.1). However, the swirl effect is simply too strong to permit the use of a Monin-Oboukhov type correction, which is indispensable if the mixing length hypothesis is used to determine the eddy viscosity. Further, the eddy viscosity should not vanish at the center, and in fact it is expected to increase to assist the laminar viscosity to result in almost rigid body rotation near the axis. This can be accomplished by employing the Prandtl-Kolmogorov hypothesis (Ref. 26 and 27), which is another widely accepted idea for various turbulent problems. Since non-isotropy was assumed, we have

$$\varepsilon = C k^{1/2} l \quad (3.22)$$

$$\varepsilon_\theta = C_\theta k^{1/2} l \quad (3.23)$$

where l is a length scale proportional to that of the energy containing-motion, and C and C_θ are hopefully universal

constants which can be attuned to experimental data for one case and then used in general. It should be noted that two extra equations are required to compute the eddy viscosity, one for $k(x,r)$ itself and the other to determine the length scale $l(x)$. The use of an integrated TKE equation is common practice for wake problems. However for trailing vortices, a differentiated TKE equation is almost a necessity to properly account for the two physically different radial regions, inside and outside the core.

The length scale $l(x)$ has been typically chosen to be proportional to the wake width even for swirling wakes. For these flows the radial decay of flow quantities is usually monotonic and quite appreciable all the way to the freestream. The situation is quite different for vortices in that the $1/r$ decay of circumferential velocity is very slow near the end. Consequently, the computational domain will be extended unnecessarily if wake width is used to determine the length scale. The only other simple choice is the core radius. However, this choice is physically meaningful, because most of the changes in flow quantities take place inside the core. Further, this will eliminate the need of a differential equation for the length scale, since it can be determined once the circumferential velocity profile is known at each axial station.

The complete TKE equation in an axi-symmetric coordinate system is:

$$\begin{aligned} uk_x + vk_r &= v\nabla^2 - \overline{\{u'(k + p'/\rho)\}}_x - \overline{\{rv'(k + p'/\rho)\}}_r/r \\ &\quad - \overline{u'^2}u_x - \overline{v'^2}v_r - \overline{w'^2}v/r \\ &\quad - \overline{u'v'}(u_r + v_x) - \overline{v'w'}(w_r - w/r) - \overline{u'w'}w_x \\ &\quad - \Phi \end{aligned} \quad (3.24)$$

where Φ represents the dissipation function. For high Reynolds number flows it is usually approximated as

$$\Phi = C_D k^{3/2}/L \quad (3.25)$$

Here, L is the dissipation length scale and C_D is a constant. In most wake problems, L is taken to be same as l and C_D is adjusted accordingly. This will be discussed in more detail later in this section. The laminar diffusion is negligible in most turbulent cases. However, it should be included in present analysis following the same rationale used for laminar and turbulent stresses. With $\partial/\partial r \gg \partial/\partial x$, the diffusion can be approximated by

$$v\nabla^2 k - \overline{\{rv'(k + p'/\rho)\}}_r/r \quad (3.26)$$

and workers who adapted the Prandtl-Kolmogorov hypothesis usually approximate the term in the brace as,

$$\overline{v'(k + p'/\rho)} \approx \epsilon k_r / \sigma_k \quad (3.27)$$

where σ_k is called a Prandtl number for TKE, and its value is about 0.7 to 1.0. With this and noticing that $\varepsilon_r = \varepsilon k_r / 2k$, the diffusion now takes the form:

$$\begin{aligned} v\nabla^2 k - \{\overline{rv' (k + p'/\rho)}\}_r/r \\ = (v + \varepsilon/\sigma_k)(k_{rr} + k_r/r) + \varepsilon k_r^2/(2k\sigma_k) \end{aligned} \quad (3.28)$$

Now for axi-symmetric flow, $\overline{v'^2} \approx \overline{w'^2}$ and this relation is exact at the axis. Using this and continuity, production of TKE by normal stresses is,

$$-\overline{u'^2}u_x - \overline{v'^2}v_r - \overline{w'^2}v/r \approx -(\overline{u'^2} - \overline{v'^2})u_x \quad (3.29)$$

and this term is negligible since $\overline{u'^2} \approx \overline{v'^2}$ and u_x is small. Among the remaining production terms, $-\overline{u'w'w_x}$ can be neglected compared to the others. With $u_r \gg v_x$, the production can be approximated by,

$$-\overline{u'v'}u_r - \overline{v'w'}(w_r - w/r) \quad (3.30)$$

With these approximations and the shear stress model in eqns (3.7) and (3.8), the TKE equation reduces to,

$$\begin{aligned} uk_x + vk_r &= (v + \varepsilon/\sigma_k)(k_{rr} + k_r/r) + \varepsilon k_r^2/(2k\sigma_k) \\ &\quad + \varepsilon u_r^2 + \varepsilon \theta (w_r - w/r)^2 \\ &\quad - C_D k^{3/2}/l \end{aligned} \quad (3.31)$$

Here, it is noted that the whole turbulence model involves only three constants, that is, C and C_θ for non-

isotropic eddy viscosities and C_D in the dissipation model. Strictly speaking, one more constant is required to relate the core radius to the length scale, but this constant can be included in C.

Unfortunately, this type of computation had never been tried for trailing vortices before, so there was little guidance for the present study. There are no widely accepted values of the turbulence model constants even for ordinary swirling flows. In such a case, the only way to proceed is to attune them to experimental data. Here, that can be done only in the near-wake due to the lack of detailed measurements in the far-field, and it is not altogether clear whether the same values would represent the far-field as well.

For the present problem, the near-wake measurements at $x/c = 6$ and 9 were used to attune the eddy viscosity and the dissipation coefficients. The values $C \approx 0.002$ and $C_D \approx 0.5$ were found to yield adequate predictions in the near-wake for both the middle and the high test speeds (the low test speed case was not computed due to the larger experimental errors in the profiles mentioned earlier). But near the end of the decay, the situation is close to axi-symmetric non-swirling wakes, and for this Launder et al (Ref. 28) suggested that $C \approx 0.05$ and $C_D \approx 1.6$ using the wake width as the length scale. Even though the core radius was used as

the length scale for the present problem, these values can be used as a reference since core size approaches wake size near the end of decay.

The big discrepancy in eddy viscosity coefficient C strongly suggests that an axial variation be introduced for it, if not for the dissipation coefficient. Here, it should be noted that the TKE or the length scale l can not be used for this purpose due to the changes in their functional involvement, which would violate the intrinsic logic in the Prandtl-Kolmogorov hypothesis. Another possible parameter upon which to base C is the swirl number S_x , which is the ratio of angular momentum flux to axial momentum flux. However, this requires direct treatment of the pressure field and therefore is not suitable for the present problem.

It was decided to use the maximum tangential velocity w_{max} which is in fact the most important variable in trailing vortices. The suppression of turbulence was simply assumed to be proportional to the maximum tangential velocity. In other words,

$$C = C' V_\infty / w_{max} \quad (3.32)$$

where C' is a constant. Since $w_{max} \approx 1/\sqrt{x}$, $C \approx \sqrt{x}$, and the resulting slow variation in C in the far-field is consistent with the slowly changing flow characters in this region. The limiting case of zero w_{max} does not present any special

problem here, since a vortex breaks down well before w_{max} decays to zero. A constant value of C was used for comparison. C_D was assumed to be constant throughout.

For non-isotropy in the eddy viscosity, few elaborate models have been generated and the usual practice is to use a proportionality constant between eddy viscosities.

$$\sigma_\theta = \varepsilon/\varepsilon_\theta \quad (3.33)$$

Lilley (Ref. 29) reported values of slightly greater than 1.0 in a study of swirl flows and suggested that, although this number might be taken to be uniform radially, it should be a function of local swirl number S_x , and he deduced empirically,

$$\sigma_\theta = 1 + 2S_x^{1/3} \quad (3.34)$$

For the present problem, direct adaptation of this formula is not suitable since the expected value of σ_θ is much greater than unity (cf. section 3.1). Also, it is not possible to develop a formula in a similar way due to the lack of Reynolds stress data in the far-field. However, the far-field is expected to be nearly turbulence-free due to the rapid decay of turbulence, and the effect of non-isotropy would be very small, if it exists. For these reasons, a constant σ_θ which gives $-\overline{u'v'} \approx -\overline{v'w'}$ in the near-wake was used throughout.

3.3 NUMERICAL FORMULATION

Since the equations were parabolized, a simple marching scheme was written in an explicit finite difference formulation. Generally an implicit formulation is considered a better choice, because it allows bigger step sizes. For the present problem, the length scale for the eddy viscosity is determined from the circumferential velocity profile and the use of an unrevised length scale during the formulation will not permit a big step size. The limit in axial step size for the explicit scheme used, was found in a von Neumann type stability analysis considering only the major shear term ($\partial^2/\partial r^2$).

$$\Delta x < V \Delta r^2 / 2(v + \varepsilon) \quad (3.35)$$

Since the eddy viscosity is higher in the near-wake, an unnecessarily small step size would result in the far-field if a constant step size is used. To avoid this, a new step size was computed at each step using the maximum value of eddy viscosity.

Another problem is the choice of the radial boundary. High resolution is essential inside the core to adequately describe the rapidly changing flow. Consequently, a large number of points are required if the computational domain is extended to the edge of the wake, which is more than ten times the core size. However, the axial velocity reaches

the freestream value well before tangential velocity does, and this condition was used to define the radial boundary. The tangential velocity outside this boundary can be safely assumed to undergo the $1/r$ potential decay.

Initial conditions are supplied by the experimental data taken at $x/c = 6$, since they display very good axi-symmetry. This also indicates that the roll-up is completed at this station, and the flow is in the plateau region. Radial velocity was assumed to be zero at the initial station instead of using the erroneous measured profiles. The initial profile for TKE was provided by the axial turbulence intensity measurements through an isotropic assumption for normal stresses, that is, $\overline{u'^2} \approx \overline{v'^2} \approx \overline{w'^2}$. A previous measurement of propeller swirl by the author (Ref. 20) showed that this assumption is acceptable even for strong swirl. To obtain accurate initial profiles, values from the entire scan were used instead of just half of it. Measured profiles are folded in half and cubic splined with least square approximation. Subroutines VS RTP, VS RTU and ICSFKU from IMSL were employed for this purpose.

The equations were numerically formulated in such a way that any physical terms may be accessed directly, to help understand the flow characteristics more clearly. The program listing is given in Appendix D.

3.4 RESULTS AND DISCUSSION

As explained before, experimental data at $x/c = 6$ and 9 were used to provide the initial profiles for axial and radial velocity and turbulent kinetic energy, and to attune C (or C'), C_D and σ_θ in the near-wake. The same values were used for these constants for both $V_\infty = 95$ and 220 fps cases. The low test speed case ($V_\infty = 30$ fps) was not computed, since measurements were not taken at $x/c = 9$, and the axial turbulence intensity profile at $x/c = 6$ showed erratic behavior. Axial turbulence intensity was not measured at these stations for $\alpha = 5^\circ$, so only the $\alpha = -10^\circ$ case was computed.

The allowable axial step size for stability was around 20% of the maximum value (cf. eqn (3.35)) for constant C cases, but axial variation in C required smaller step size of about 5%. The radial boundary was chosen at $r = 2.4$ in. which was about 6 to 8 times the initial core radius. To provide high resolution inside the core, 48 radial steps were used.

About 10 sec. of CPU time was needed on the IBM 370/3081 computer to reach 2,000 ft downstream in a computation with constant C .

Even though the computational results in the far-field can not be verified directly due to lack of the experimental data, some previous studies provide valuable insight. One

is the effective (or apparent) viscosity concept in which the turbulent viscosity is simply assumed to be proportional to laminar viscosity (Ref. 8). The magnitude of the effective viscosity ε_e can be readily found through an appropriate laminar analysis. The most frequently used is the solution for the impulsively started vortex (Lamb Vortex),

$$w = \Gamma_o (1 - e^{-\zeta}) / 2\pi r \quad (3.36)$$

where $\zeta = V_\infty r^2 / 4\varepsilon_e x$ is a similarity variable for laminar motion and Γ_o is the circulation at large r . Therefore, if Γ_o and w_{max} are known, the effective viscosity is given as

$$\varepsilon_e \approx 0.0026 (V_\infty/x) (\Gamma_o/w_{max})^2 \quad (3.37)$$

In the near-wake, reported values of ε_e are from 10 to 80 v (Ref. 8), but values greater than 100 v were obtained in flight test (Ref. 30). For the present problem, the near-wake measurements of Γ_o and w_{max} yielded ε_e of about 20 to 30 v for $V_\infty = 95$ fps, and 50 to 70 v for $V_\infty = 220$ fps (cf. Fig. 41). As a reference, typical near-wake values of the eddy viscosity ε used in the computations are about 30 v at the center and about 5 v outside the core (at the initial station for $V_\infty = 95$ fps). Although these ε values can not be compared directly to ε_e values given above (ε_e does not vary radially), reasonable agreement between these values

shows that the turbulence model developed here produces eddy viscosity values of the correct order of magnitude.

Since the present measurements are only in the near-wake, the only way to achieve detailed verification of the present computations (hence the turbulence model), is to use the results of the correlation study by Iversen (Ref. 7). He solved a similarity equation for the circulation with a radially varying eddy viscosity, and plotted both scale model and flight data in terms of the resulting scaling parameters for maximum tangential velocity and axial distance:

$$w_{\max}^b / \Gamma_o^{AR} \quad (3.38)$$

$$(x/b) (\Gamma_o / V_\infty b) AR^2 f(\Gamma_o / v) \quad (3.39)$$

where b and AR are the span length and the aspect ratio of the wing, and $f(\Gamma_o / v)$ is a function of vortex Reynolds number. Fig. 28 shows the result along with the $f(\Gamma_o / v)$ profile. Maximum tangential velocity data from ground-based facilities and flight tests are nearly correlated into a single curve, and the existence of the plateau region is apparent. This curve will be used as the main basis in verifying the present computational results in the far-field.

As discussed before, C and C_D were attuned to the present near-wake measurements, which yielded $C \approx 0.002$ and $C_D \approx 0.5$. The axial variation in C was assumed to be inversely proportional to w_{\max} (cf. eqn (3.32)), and $C' \approx 0.001$ was chosen since $w_{\max} \approx 0.6 V_\infty$ at the initial station. σ_θ was determined to be about 3 on the prognosis that $-\overline{u'v'} = -\overline{v'w'}$. It was found that diffusion is small compared to production and dissipation, and $\sigma_k = 0.7$ was used throughout. Computed velocity profiles in the far-field showed little sensitivity to the changes in these coefficients, and this is the result of rapidly decaying turbulence which would render the rest of the flow field close to laminar. However, axial turbulence intensity (ATI) and shear stress profiles were very sensitive to C , C_D and σ_θ , and this is due to their direct dependence on these coefficients.

Although it is not a matter of direct comparison, the constants for axi-symmetric non-swirling wake (with wake radius to represent the length scale) suggested by Launder et al (Ref. 28) can be used to give a rough idea as to the magnitude of turbulence production and dissipation in the near-wake. The core radius is about 1/10 of the wake radius in the near-wake and therefore, the constants used in the present computation should be interpreted as $C \approx 0.0002$ and $C_D \approx 5.0$. With the usual values of $C \approx 0.05$ and $C_D \approx 1.6$

for a non-swirling wake, it can be seen that production of turbulence for the present vortex is about 1/250 of that for a non-swirling wake, although dissipation remains at roughly the same level. This is the physical anatomy of the turbulence in the near-wake, that is, the rapid decay is the result of very small production, not of high dissipation or diffusion.

Figures 29 to 31 show the decay in velocity profiles for $V_\infty = 95$ fps. Radial velocity is found to be three orders of magnitude smaller than u or w , which means that the balance between radial pressure gradient and centrifugal acceleration is almost perfect. In fact, this is the main reason behind the strong persistence of trailing vortices. A constant C was used and it can be seen that about 4,000 ft is required to complete the decay. However, axial and tangential velocity profiles obtained with axially varying C (Fig. 32 and 33) predict the required decay length to be only about 2,000 ft. This situation is summarized in Fig. 34 with Iversen's correlation. It is seen that the present measurements give about 2 times greater dimensionless w_{max} than correlated by Iversen. This is primarily due to the difference in wing planform and aspect ratio between those used for correlation and present model. As explained in Fig. 28, the wing models used for correlation in the plateau

region had rectangular planforms with high aspect ratios of 5.3 to 12, whereas a highly tapered (2:1) and small aspect ratio (2.7) wing was used for the present study, which resulted in a more elliptic circulation distribution along the wing span. Since Γ_0 is proportional to the average circulation on the wing (cf. Ref. 3), a smaller Γ_0 resulted. In spite of this discrepancy in magnitude, the decay trend predicted by the computation with an axially varying C agrees very well with the correlated data. However, a constant C predicts a slow decay especially near the end where the flow was predicted essentially laminar. This is the result of unnecessarily severe suppression of turbulence in the far-field imposed by the coefficient determined in the near-wake. The use of an axially varying C can be justified in this regard, although more detailed measurements are required for confirmation and further, to determine the exact functional relation.

Axial and tangential velocity decay for $V_\infty = 220$ fps are shown in Fig. 35 and 36, respectively. No changes were made to the coefficients used for $V_\infty = 95$ fps, and the changes in decay pattern are not appreciable. Maximum tangential velocity decay for both speeds is summarized in Fig. 37 which confirms that the Reynolds number effect is indeed small. One important finding is that the axial velocity defect around the center grows in the plateau region and the

recovery does not start until at the beginning of the decay region (cf. Fig. 32 and 35). This is an obvious result of the pressure adjustment in the core, but it has been assumed so far that the pressure is fully adjusted with the completion of the roll-up process. Fig. 38 depicts the growth of core size. Again Reynolds number effects on the growth pattern are small as was the case for the maximum tangential velocity decay. Here, it should be noted that the Reynolds number was found to have a major influence on vortex formation in the near-wake.

Figures 39 and 40 describe the decay of axial turbulence intensity for both speeds. As discussed before, they were very sensitive to changes in eddy viscosity and dissipation coefficients. The prediction at $x/c = 9$ is poor inside the core for both cases and this is mainly due to high dissipation caused by the $k^{3/2}$ term. Although better prediction is possible if a smaller dissipation coefficient is used inside the core, it was not implemented primarily due to lack of supporting reasoning, but also because of inaccuracies involved in the present measurements in this region.

Fig. 41 shows the decay of the effective viscosity for both speeds. Near-wake values of 20 to $70v$ agree very well with those reported in Ref. 8. The existence of non-equilibrium turbulence in the plateau region is clearly

evidenced by the very rapid decay, whereas the turbulence is apparently in equilibrium in the decay region, which is really the basis for similarity.

The axial and tangential shear stress profiles for $V_\infty = 95$ fps are given in Fig. 42 and 43. The radial shear stress ($-\overline{u'w'}$) was found to be about two order of magnitude smaller than the axial or tangential shear stress, and is not plotted. It should be noted that these are not the result of computation, but a part of the assumptions since the non-isotropy constant σ_θ was determined to give axial and tangential shear stresses the same order of magnitude.

Chapter IV

CONCLUSIONS

A coordinated computational and experimental study was undertaken to investigate the behavior of the vortices trailing from low aspect ratio lifting surfaces. Vortex formation in the near-wake was measured in a wind tunnel with yaw-head and hot-wire probes at three different Reynolds numbers. These near-wake measurements provided the initial conditions for the computational study of the far-field decay, with a numerical method comprehensive enough to describe the whole flow characters including axial flow and turbulence. The parabolized Navier-Stokes equations written in terms of vorticity and stream function were employed. Turbulent transport was modeled through the turbulent kinetic energy and the Prandtl-Kolmogorov hypothesis to give an eddy viscosity with the core radius chosen as the length scale. Results of the correlation study by Iversen were used to verify the computation results. A summary of the detailed findings follows:

1. The vortex location is determined essentially by model geometry and downstream distance with little influence from Reynolds number. However, the Reynolds number is found to play a major role in vortex formation in the near-wake. It has a

decreasing effect on both axial velocity defect and axial turbulence intensity, and an increasing effect on maximum tangential velocity. The computation adequately predicted these effects.

2. The decay in the far-field is determined mainly by downstream distance and the Reynolds number has little influence on the decay trend. The predicted decay for maximum tangential velocity agrees very well with Iversen's correlation.
3. The rapid decay of turbulence is due to small production, not to high dissipation or diffusion.
4. The axial velocity defect around the center grows in the plateau region, and the recovery does not start until at the beginning of the decay region. This disputes the usual assumption that the pressure is fully adjusted with the completion of the roll-up process.
5. The effect of small aspect ratio on the vortex formation is not direct, but through corresponding wing characteristics.
6. The asymmetry during the roll-up is mainly in the vertical direction.
7. The role of vortex age as a self-sufficient parameter in vortex study is not confirmed.

8. A simplified calibration procedure which may reduce considerably the amount of work needed in calibration of 5-port, yaw-head probes is suggested.

REFERENCES

1. Ciffone, D. L. and Orloff, K. L., "Far-Field Wake-Vortex Characteristics of Wings," AIAA J. Aircraft, vol. 12, no. 5, 1975.
2. Crow, S. C., "Stability Theory for a Pair of Trailing Vortices," AIAA J., vol. 8, no. 12, 1970.
3. Betz, A., "Behavior of Vortex Systems," NACA TM 713, 1933.
4. Rossow, V. J., "Prediction of Span Loading from Measured Wake-Vortex Structure - An Inverse Betz Method," AIAA J. Aircraft, vol. 12, no. 7, 1975.
5. Donaldson, C., duP., "A Brief Review of the Aircraft Trailing Vortex Problem," A.R.A.P. Report, no. 155, 1971.
6. Bilanin, A. J., and Donaldson, C., duP., "Estimation of Velocities and Roll-Up in Aircraft Vortex Wakes," AIAA J. Aircraft, vol. 12, no. 7, 1975.
7. Iversen, J. D., "Correlation of Turbulent Trailing Vortex Decay Data," AIAA J. Aircraft, vol. 13, no. 5, 1976.
8. Hall, M. G., "The Structure of Concentrated Vortex Cores," Progress in Aeronautical Science, vol. 7, Pergamon Press, New York, 1966.

9. Batchelor, G. K., "Axial Flow in Trailing Line Vortices," J. Fluid Mech., vol. 20, 1964.
10. Moore, D. W. and Saffman, P. G., "Axial Flow in Laminar Trailing Vortices," Proc. of the Royal Society, Ser. A, Mathematical and Physical Sciences, vol. 333, 1973.
11. Fernandez, F. L. and Lubard, S. C., "Turbulent Vortex Wakes and Jets," AIAA Paper, no. 71-615, 1971.
12. Iversen, J. D., "Inviscid to Turbulent Transition of Trailing Vortices," AIAA paper, no. 75-883, 1975.
13. Donaldson, C. duP., "Calculation of Turbulent Shear Flow for Atmospheric and Vortex Motions," AIAA J., vol. 10, no. 1, 1972.
14. Brunn, H. H., "Linearization and Hot-Wire Anemometry," J. of Physics, E: Scientific Instruments, vol. 4, 1971.
15. Mason, W. H. and Marchman, J. F., "Farfield Structure of an Aircraft Trailing Vortex, Including Effects of Mass Injection," NASA CR-62078, 1972.
16. Treaster, A. and Yocum, A., "The Calibration and Application of Five-Hole Probes," ISBN 87664-403-5, 1978.
17. Winternitz, F. A. L., "Probe Measurements in Three-Dimensional Flow," Aircraft Engineering, 1956.

18. Stottmeister, H. P. and Schetz, J. A., "Experimental Measurements in the Near Wake Region of a Self-Propelled Slender Body with Attached Appendages," VPI-Aero-077, 1978.
19. Chue, S. H., "Pressure Probes for Fluid Measurements," Progress Aerospace Science, vol. 16, no. 2, 1975.
20. Schetz, J. A., Lee, H. and Kong, F., "Measurements in the Near-Wake Region of a Slender, Self-Propelled Model at Pitch or Yaw," (to be published in J. of Ship Research)
21. Marshall, J. R., and Marchman, J. F., "Vortex Age as a Wake Turbulence Scaling Parameter," VPI-Aero-006, 1973.
22. Rorke, J. B. and Moffitt, R. C., "Wind Tunnel Simulation of Full Scale Vortices," NASA CR-2180, 1973.
23. Ribeiro, M. M. and Whitelaw, J. H., "Co-Axial Jets With and Without Swirl," J. Fluid Mech., vol. 96, part 4, 1980.
24. Monin, A. S., "On Symmetry Properties of Turbulence in the Surface Layer of Air," Izv. Akad. Nauk. SSSR, Fiz. Atmos. Okeana, vol. 11, 1965.
25. Bradshaw, P., "The Analogy Between Streamline Curvature and Buoyancy in Turbulent Shear Flow," J. Fluid Mech., vol. 36, part 1, 1969.

26. Prandtl, L., "Uber ein neues Formelsystem fur die ausgebildete Turbulenz," Nachr. Akad. Wiss., Gottingen, Math.-Phys. Klasse, 1945.
27. Kolmogorov, A. N., "Equations of Turbulent Motion of an Incompressible Fluid," Izv. Akad. Nauk. SSSR, Seria Fiz. Vi., no. 1-2, 1942.
28. Launder, B. E., Morse, A., Rodi, W. and Spalding, D. B., "The Prediction of Free Shear Flows - A Comparision of the Performance of Six Turbulence Models," NASA SP-321, 1973.
29. Lilley, D. G., "Prediction of Inert Turbulent Swirl Flows," AIAA J., vol. 11, no. 7, 1973.
30. McCormick, B. W., Tangler, J. L. and Sherrieb, H., "Structure of Trailing Vortices," AIAA J. Aircraft, vol. 5, 1968.
31. "Aircraft Wake Turbulence and Its Detection," edited by Olsen, Goldburg and Rogers, Plenum Press, New York, 1971.
32. "Wake Vortex Minimization," NASA SP-409, 1976.

	<u>$\alpha = 5^\circ$</u>		<u>$\alpha = -10^\circ$</u>	
	horizontal distance from $\frac{c}{2}$	vertical distance from floor	horizontal distance from $\frac{c}{2}$	vertical distance from floor
<u>$x/c = 3$</u>				
$V_\infty = 30$ fps	15.17	15.00	14.47	16.39
95	15.06	15.06	14.68	16.25
220	15.06	15.19	14.61	16.04
<u>$x/c = 6$</u>				
$V_\infty = 30$ fps	14.92	14.85	13.13	16.87
95	14.65	14.89	13.41	16.75
220	14.75	14.73	13.28	16.69
<u>$x/c = 9$</u>				
$V_\infty = 30$ fps	14.81	14.44	12.75	17.44
220	14.84	14.50	12.69	17.37
(inch)				

Table 1 Location of Vortex Centers

	<u>$\alpha = 5^\circ$</u>		<u>$\alpha = -10^\circ$</u>	
	horizontal scan	vertical scan	horizontal scan	vertical scan
<u>$x/c = 3$</u>				
$V_\infty = 30$ fps	0.47	0.39	0.50	0.35
95	0.31	0.31	0.35	0.35
220	0.30	0.31	0.27	0.29
<u>$x/c = 6$</u>				
$V_\infty = 30$ fps	0.45	0.45	0.60	0.47
95	0.32	0.31	0.40	0.35
220	0.32	0.29	0.28	0.31
<u>$x/c = 9$</u>				
$V_\infty = 30$ fps	0.30	0.43	0.40	0.37
220	0.27	0.35	0.35	0.31
(inch)				

Table 2 Vortex Core Radius

	<u>$\alpha = 5^\circ$</u>		<u>$\alpha = -10^\circ$</u>	
	horizontal scan	vertical scan	horizontal scan	vertical scan
<u>$x/c = 3$</u>				
$V_\infty = 30$ fps	0.44	0.44	0.47	0.49
95	0.58	0.57	0.63	0.61
220	0.56	0.60	0.62	0.66
<u>$x/c = 6$</u>				
$V_\infty = 30$ fps	0.39	0.38	0.35	0.36
95	0.52	0.53	0.59	0.59
220	0.63	0.61	0.66	0.66
<u>$x/c = 9$</u>				
$V_\infty = 30$ fps	0.53	0.51	0.55	0.56
220	0.61	0.59	0.64	0.63
			(V_∞)	

Table 3 Maximum Tangential Velocity

	<u>$\alpha = 5^\circ$</u>		<u>$\alpha = -10^\circ$</u>	
	horizontal scan	vertical scan	horizontal scan	vertical scan
<u>$x/c = 3$</u>				
$V_\infty = 30$ fps	0.75	0.78	0.64	0.66
95	0.97	0.94	0.84	0.81
220	0.97	0.94	0.95	0.95
<u>$x/c = 6$</u>				
$V_\infty = 30$ fps	0.77	0.78	0.92	0.90
95	0.95	0.95	0.85	0.86
220	1.05	1.06	1.00	1.00
<u>$x/c = 9$</u>				
$V_\infty = 30$ fps	0.90	0.91	0.83	0.81
220	1.00	1.01	0.95	0.95
				(V_∞)

Table 4 Axial Velocity at Vortex Center

$\alpha = 5^\circ$ $\alpha = -10^\circ$

	horizontal	vertical	horizontal	vertical
	scan	scan	scan	scan

 $x/c = 3$

$V_\infty = 30$ fps	8.1	8.5	8.6	9.2
95	6.4	6.7	6.1	5.2
220	5.8	4.9	3.0	3.8

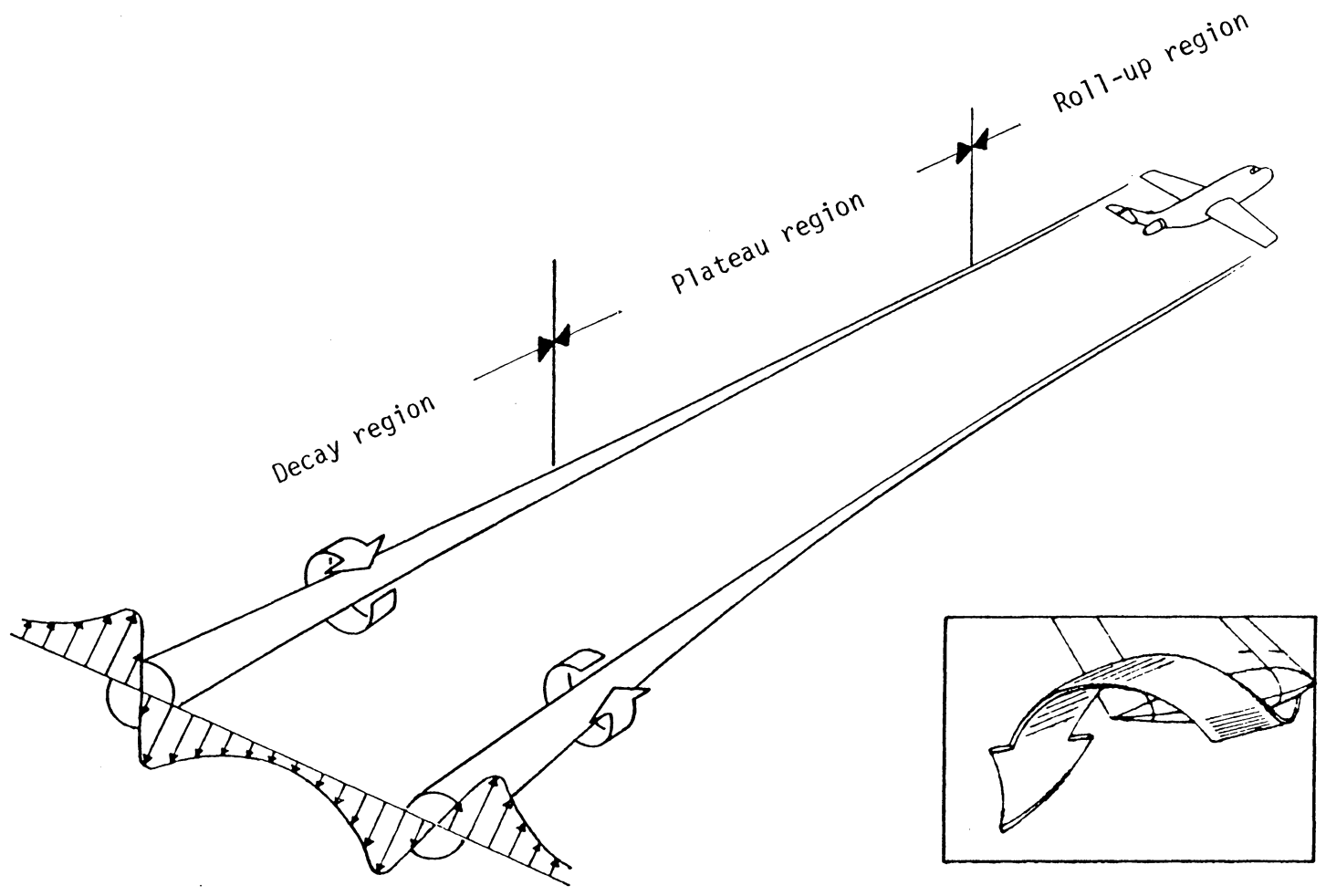
 $x/c = 6$

$V_\infty = 30$ fps		6.6	9.8
95		6.0	5.7
220		4.0	3.9

 $x/c = 9$

$V_\infty = 30$ fps		3.1	4.5
220		4.3	4.9
		(%)	

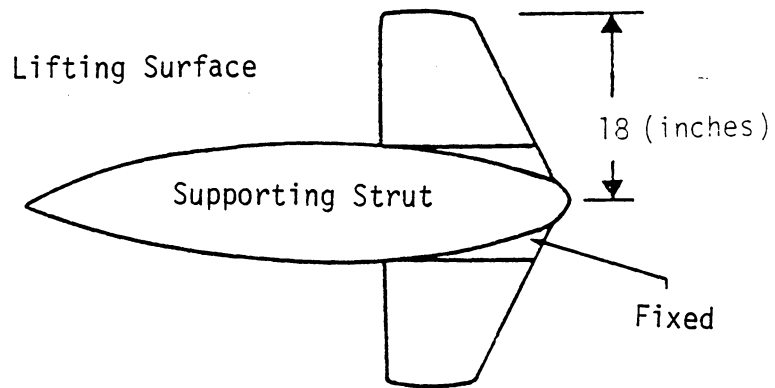
Table 5 Axial Turbulence Intensity at Vortex Center



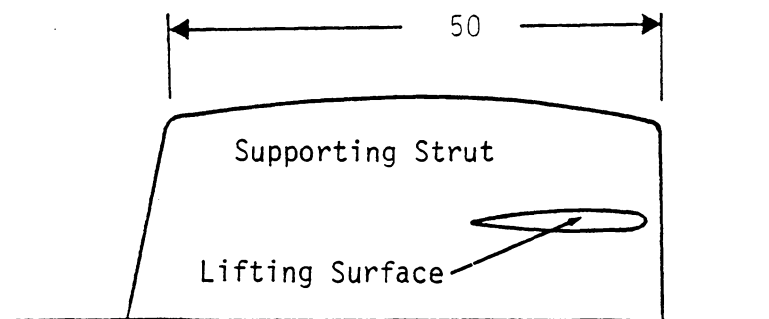
Typical Tangential Velocity Profile
(Core size is exaggerated)

Formation of the Tip Vortices

Fig. 1 Structure of Trailing Vortices



(a) Top View



(b) Side View

Fig. 2 Model Description

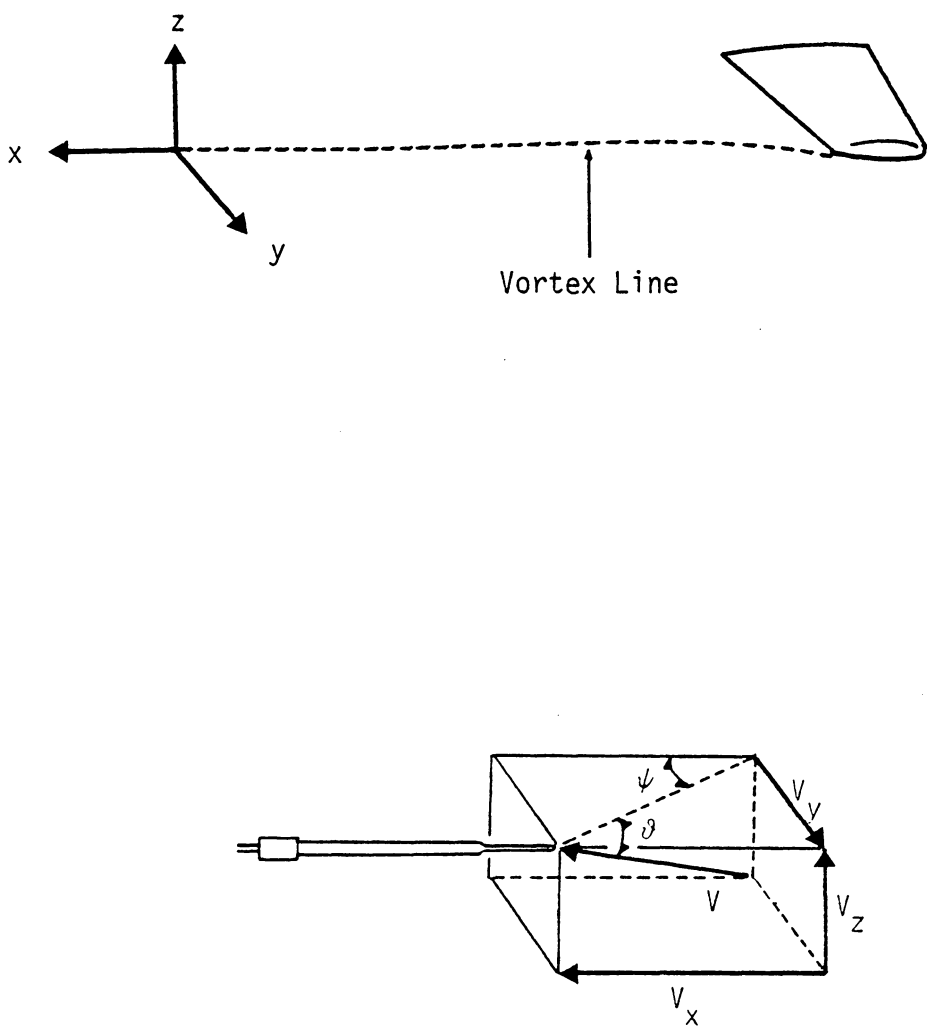


Fig. 3 Coordinate System for Experimental Study

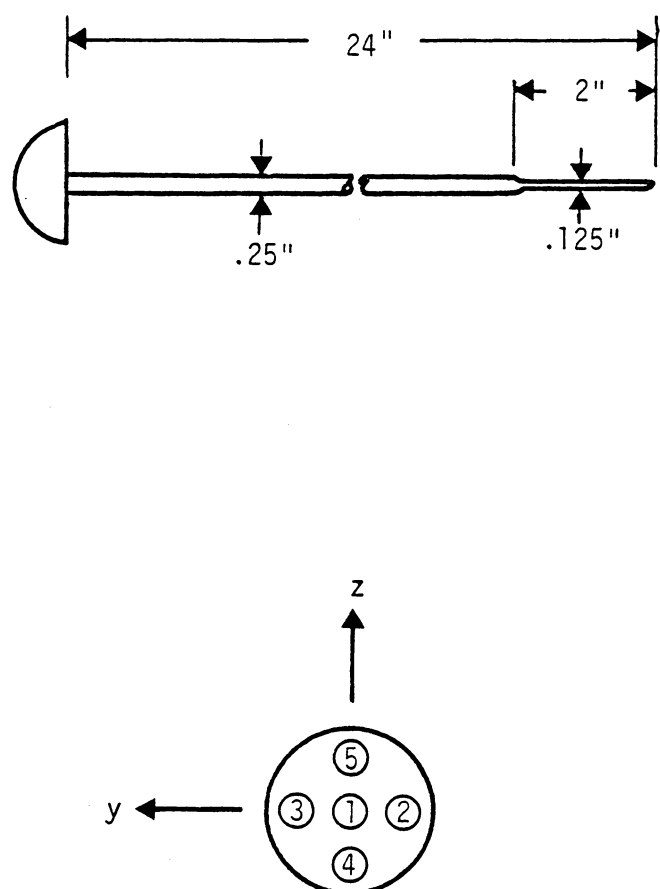
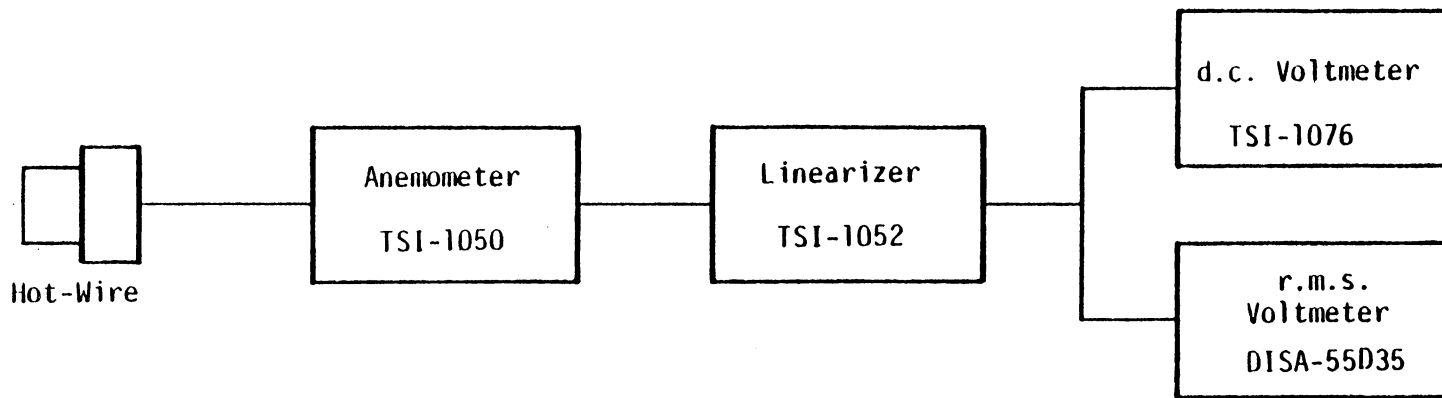


Fig. 4 Description of Yaw-Head Probe



T₁

Fig. 5 Arrangement of Hot-Wire Anemometer System

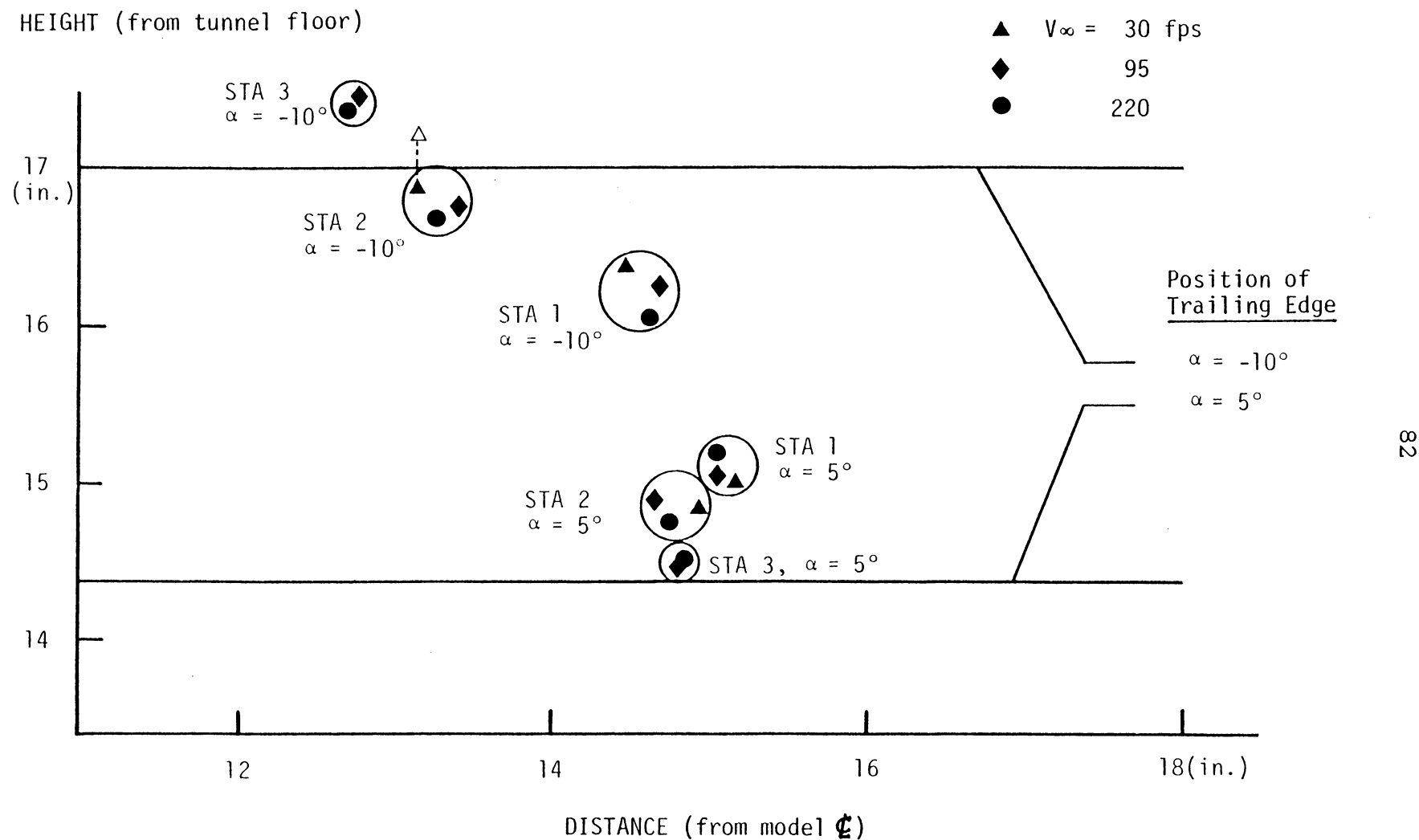


Fig. 6 Location of Vortex Centers

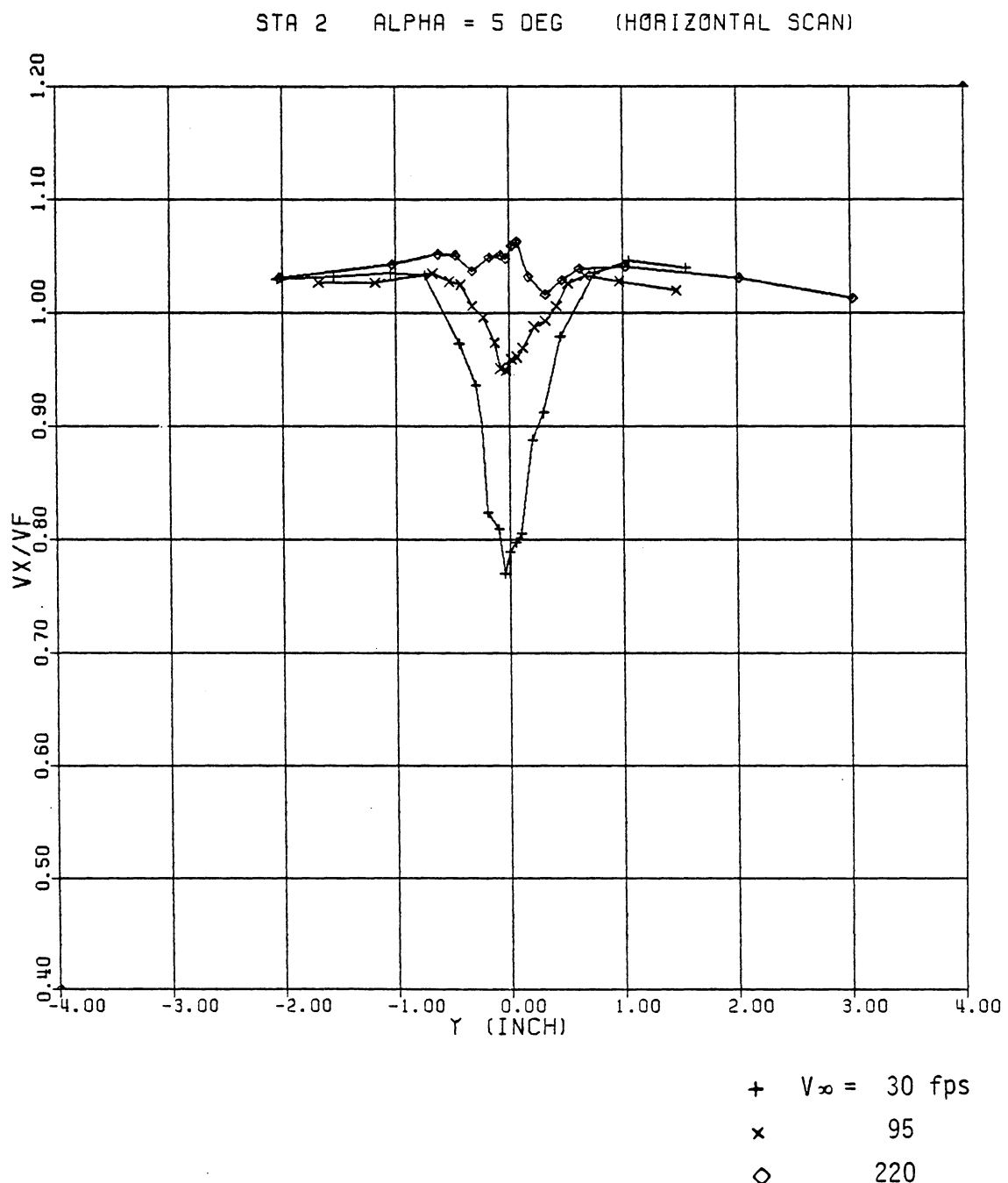


Fig. 7 Typical Axial Velocity Profiles

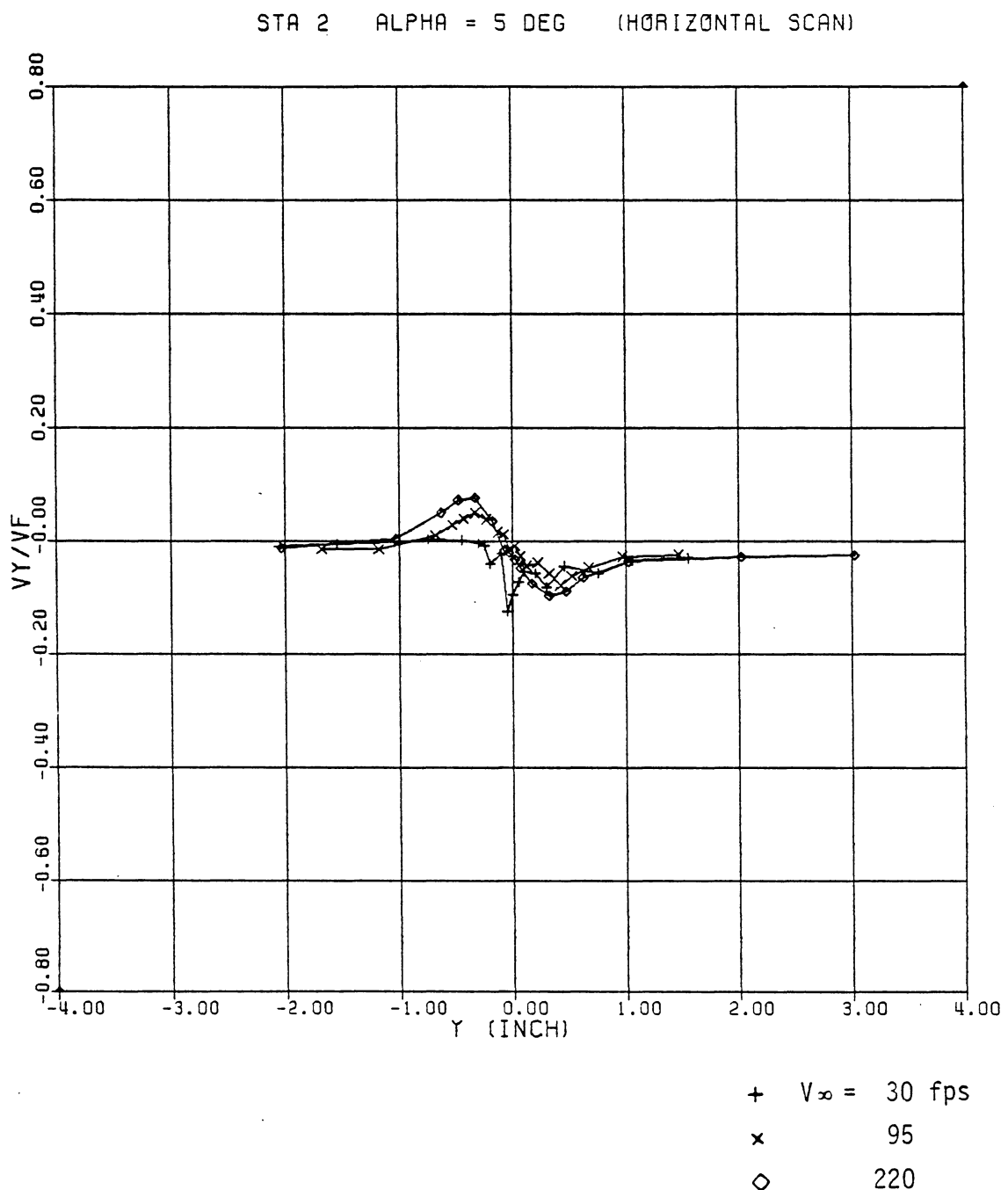


Fig. 8 Typical Radial Velocity Profiles

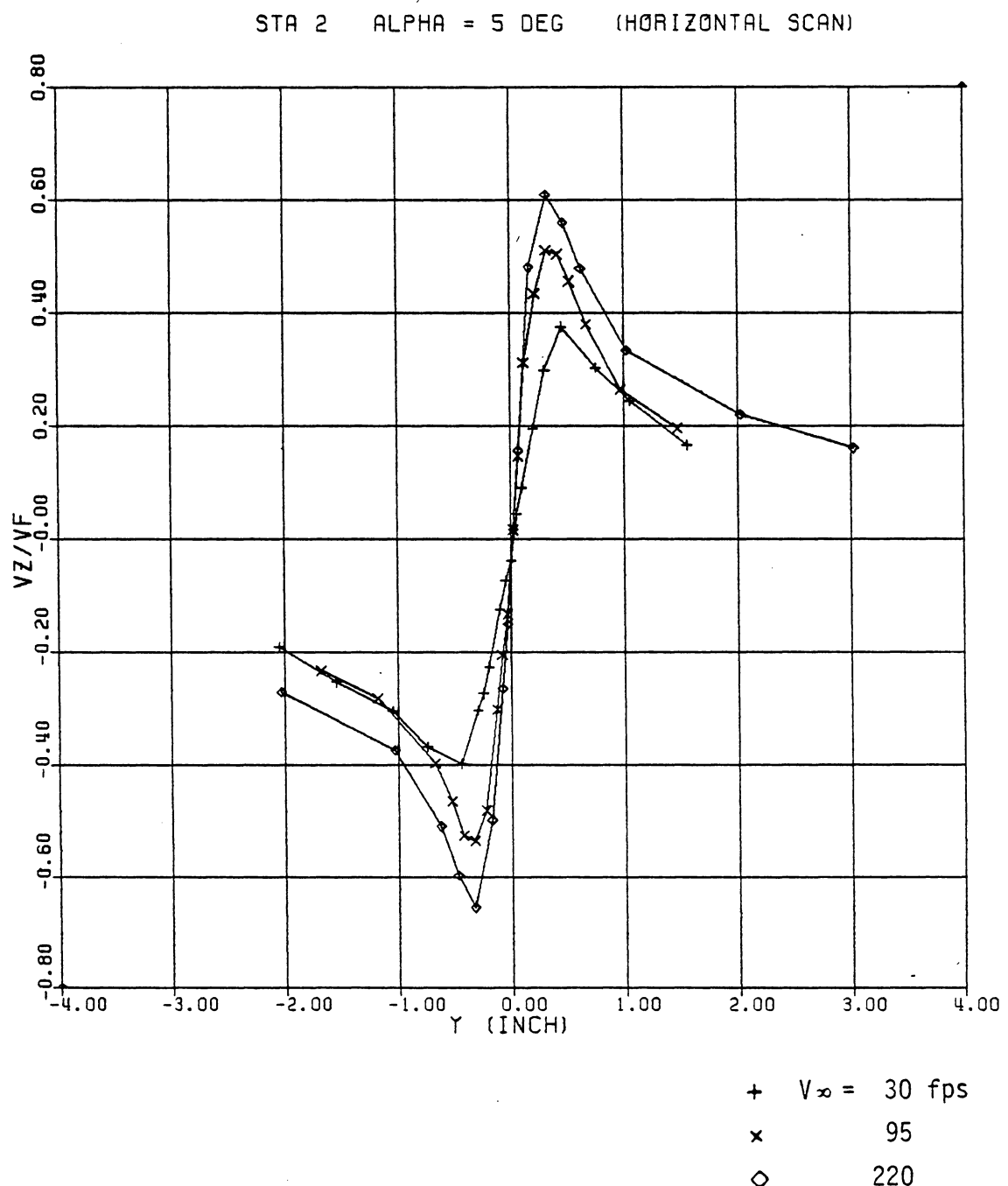


Fig. 9 Typical Tangential Velocity Profiles

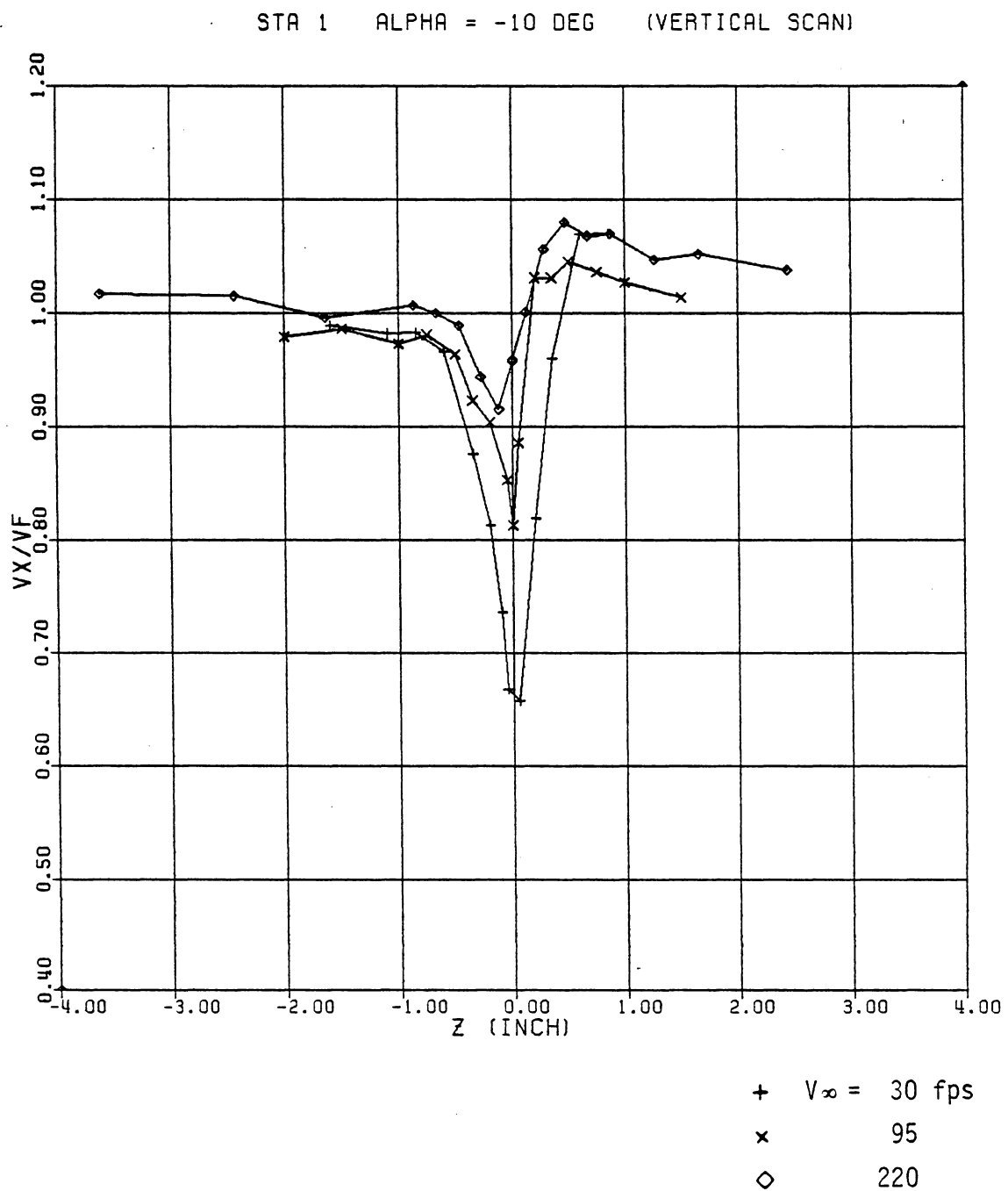


Fig. 10 Asymmetry in Axial Velocity Profiles at $x/c = 3$

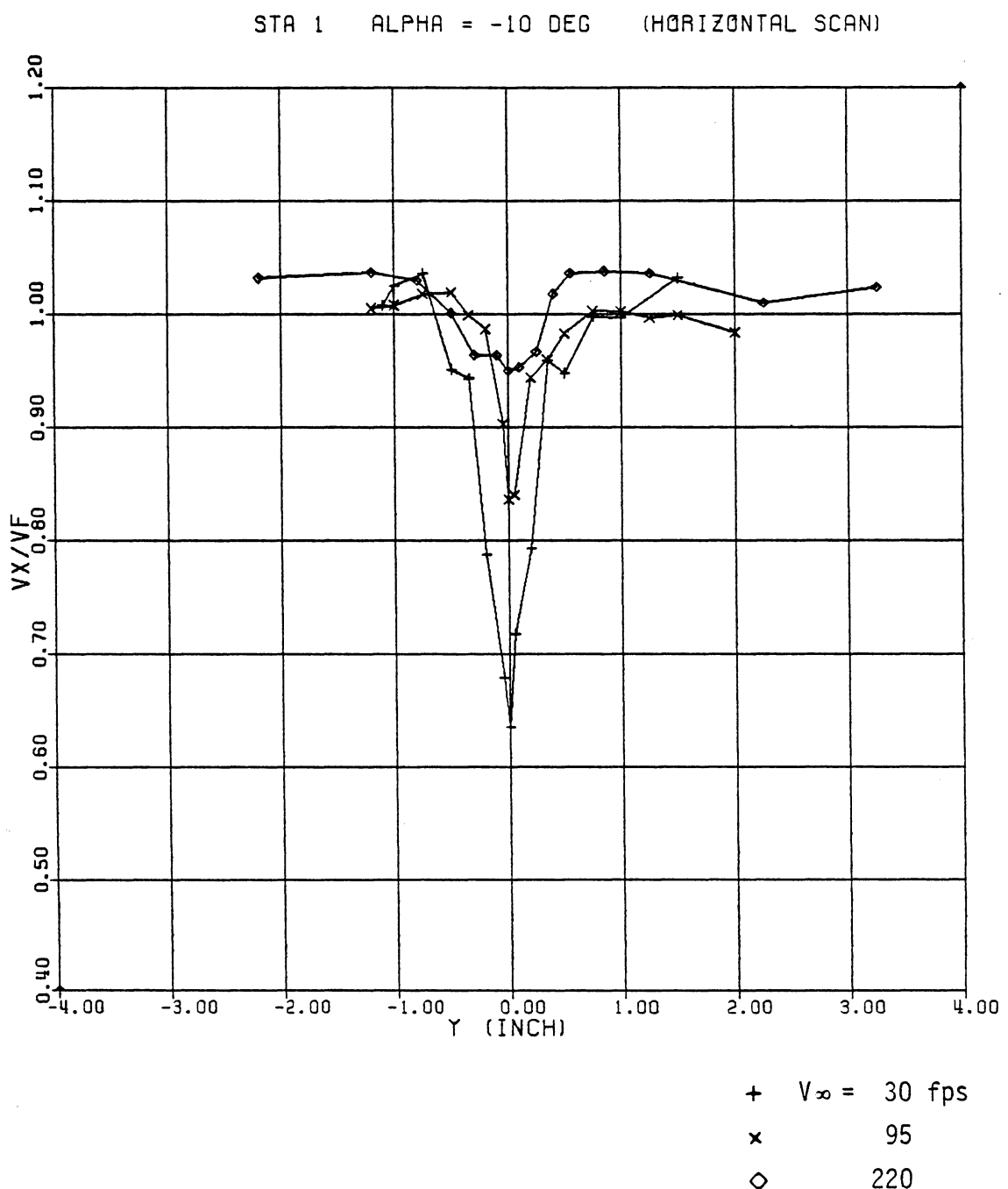


Fig. 11 Symmetry in Axial Velocity Profiles at $x/c = 3$

ALPHA = 5 DEG Q = 0.2 IN. OF WATER (HORIZONTAL SCAN)

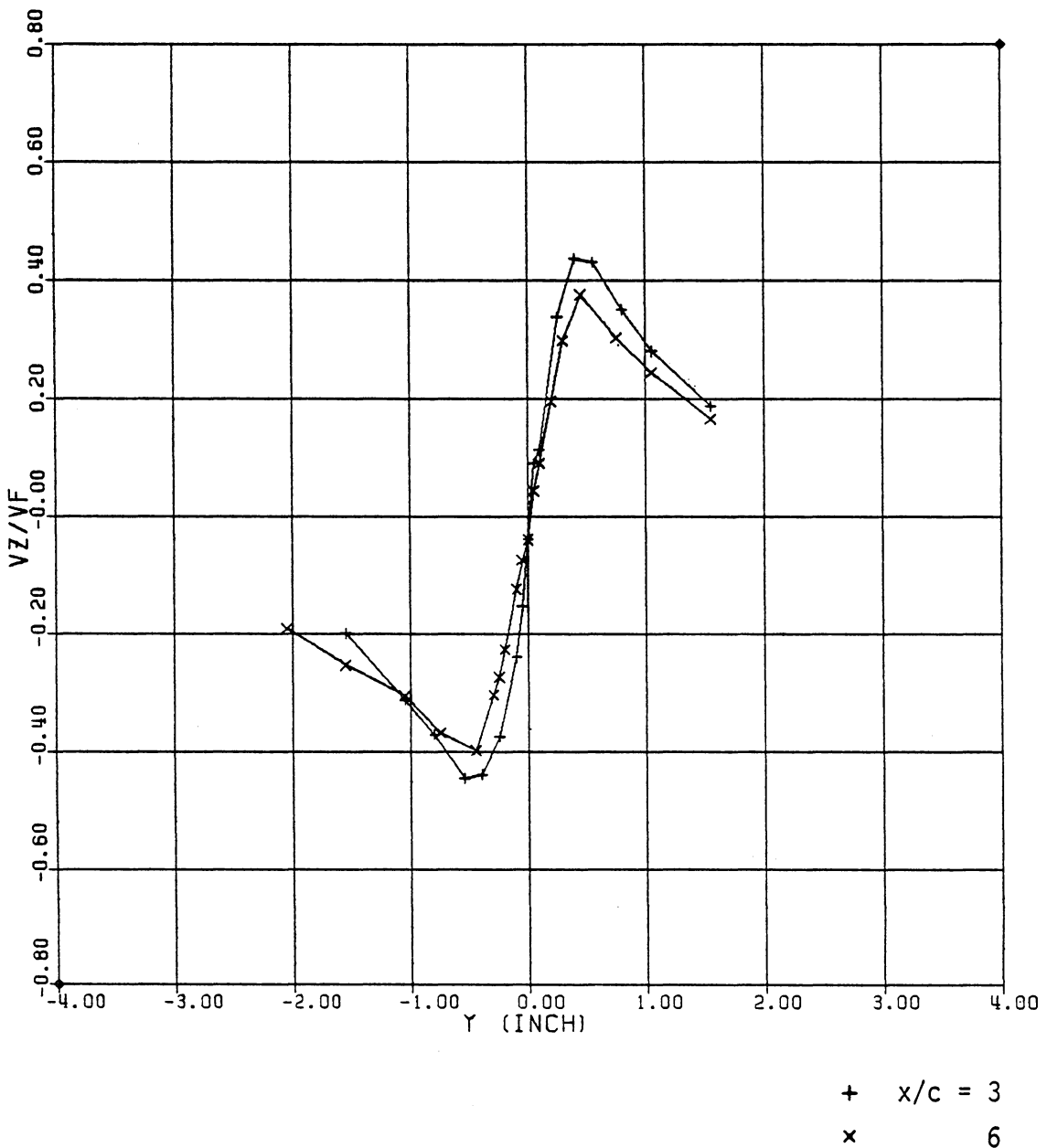


Fig. 12 Effect of Downstream Distance on Tangential Velocity
for $V_\infty = 30$ fps

ALPHA = 5 DEG Q = 2.0 IN. OF WATER (HORIZONTAL SCAN)

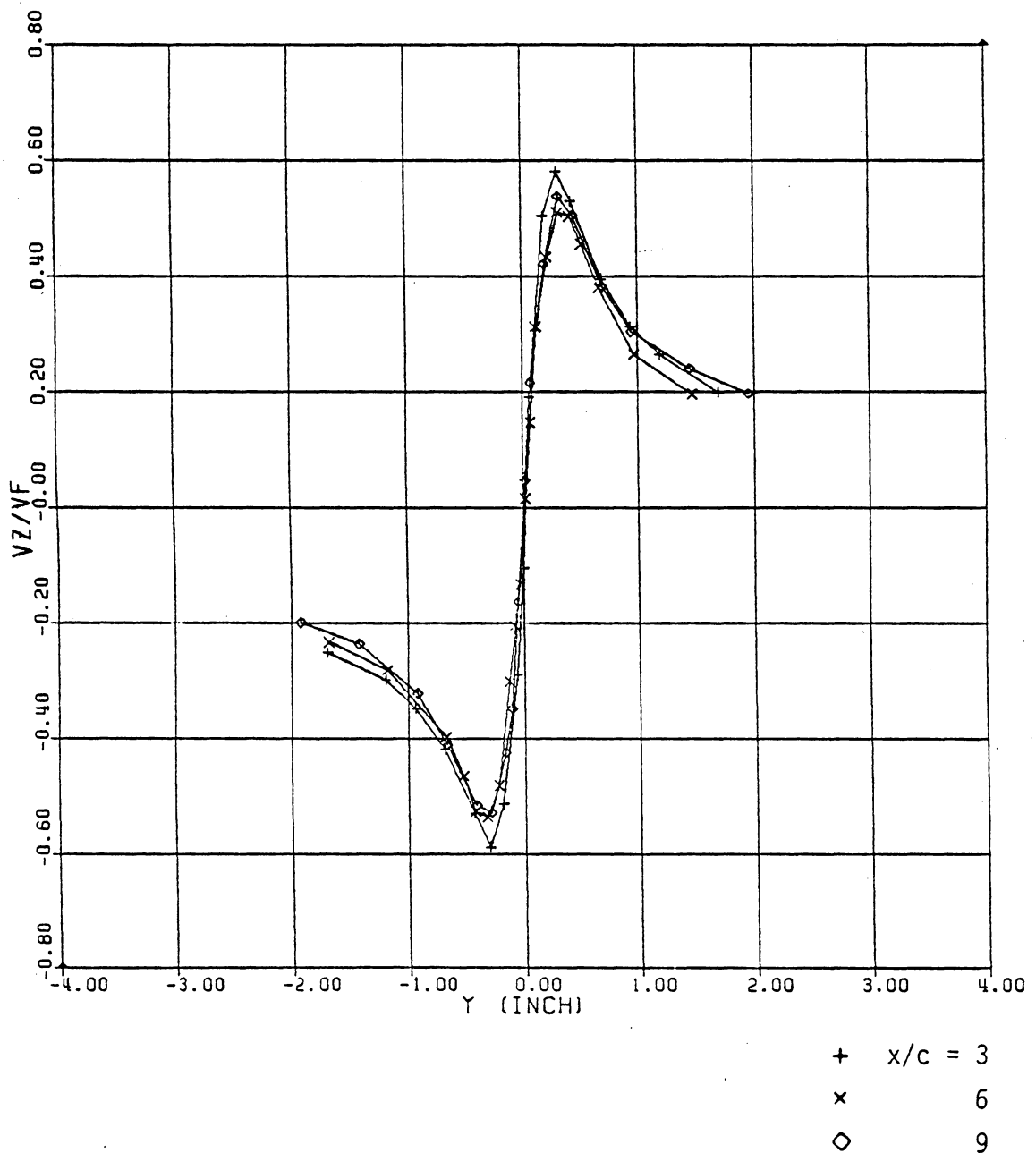


Fig. 13 Effect of Downstream Distance on Tangential Velocity
for $V_\infty = 95$ fps

ALPHA = 5 DEG Q = 9.5 IN. OF WATER (HORIZONTAL SCAN)

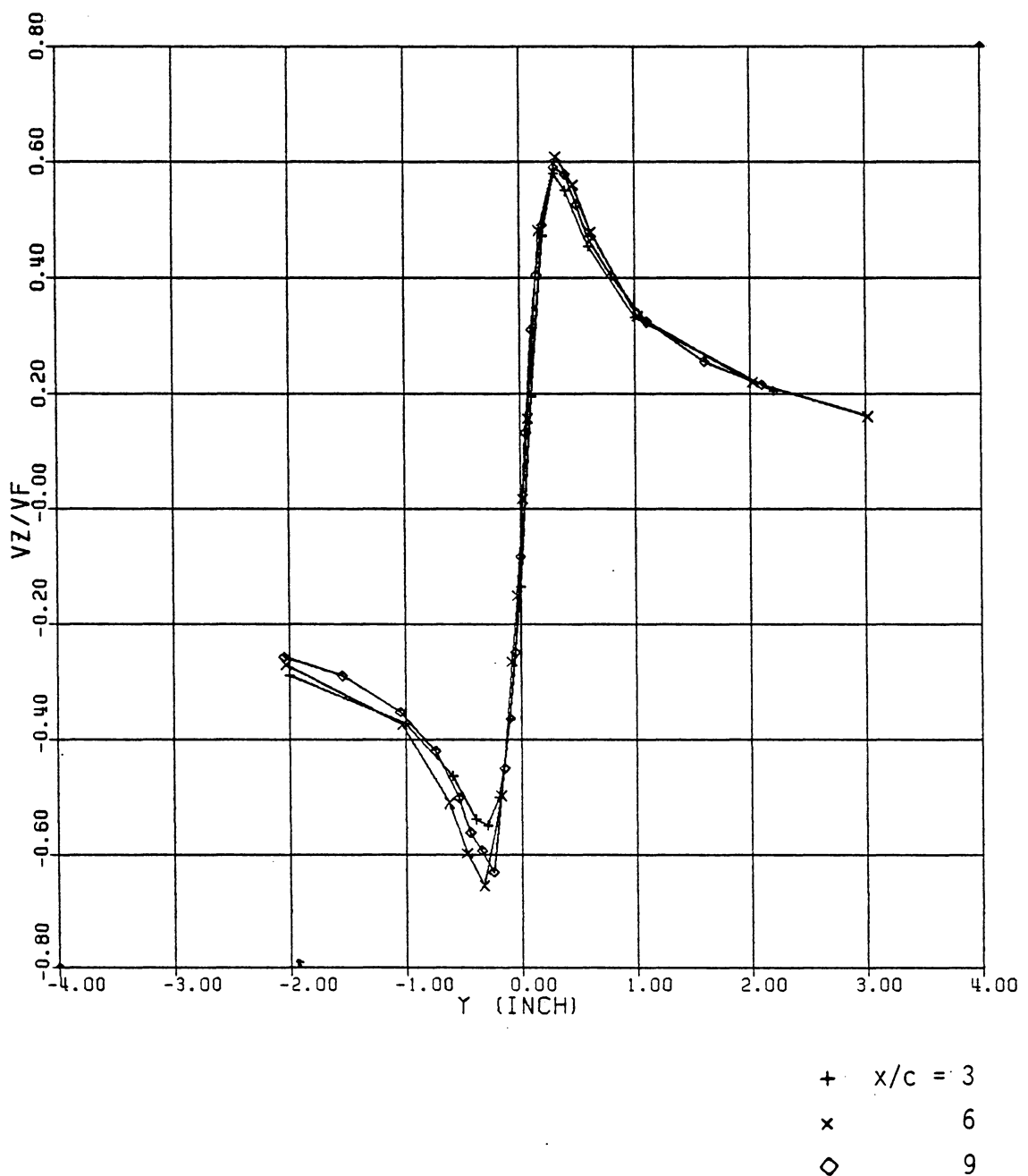


Fig. 14 Effect of Downstream Distance on Tangential Velocity
for $V_\infty = 220$ fps

STA 1 ALPHA = 5 DEG (HORIZONTAL SCAN)

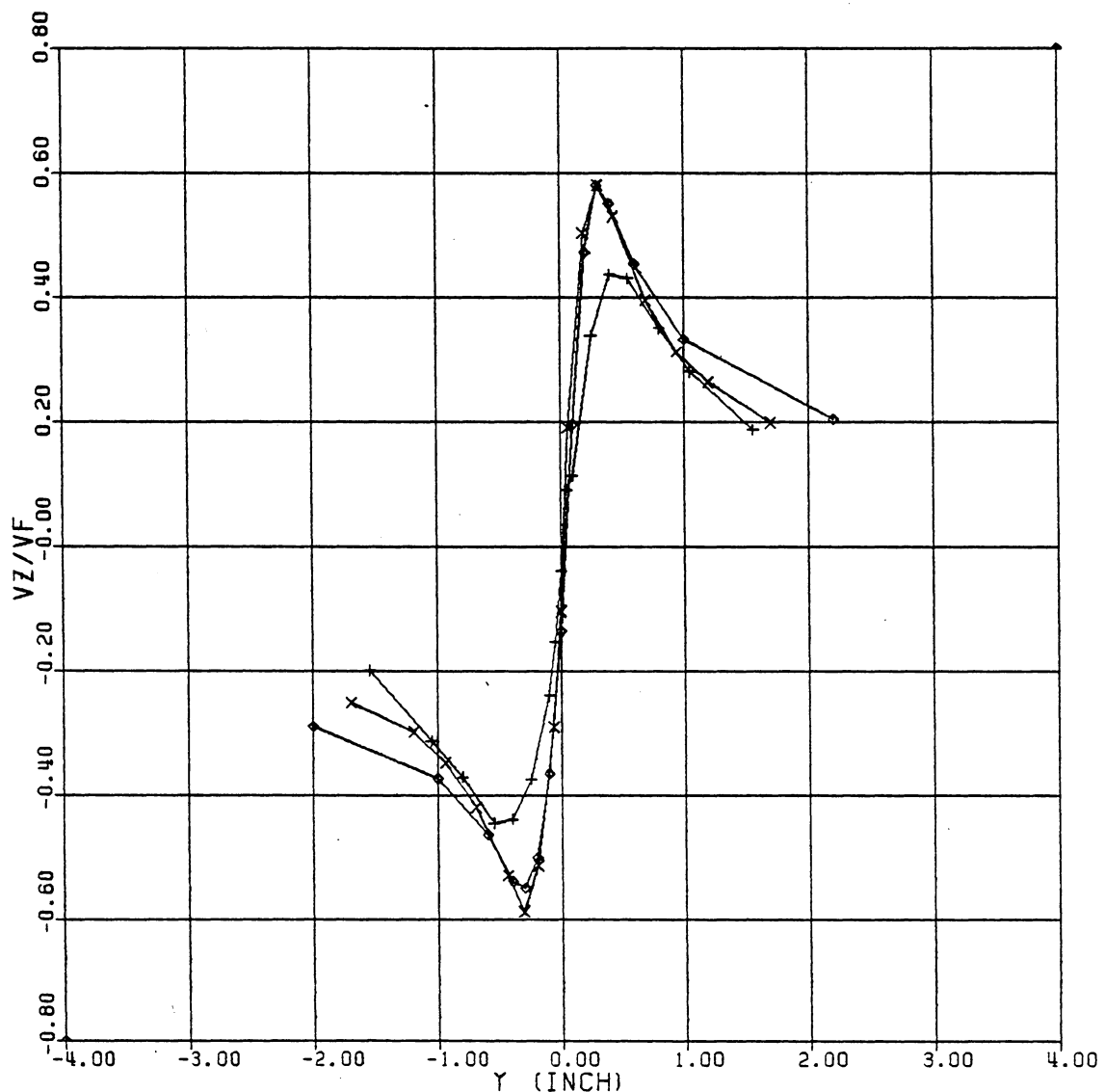


Fig. 15 Effect of Angle of Attack on Tangential Velocity
for $\alpha = 5^\circ$

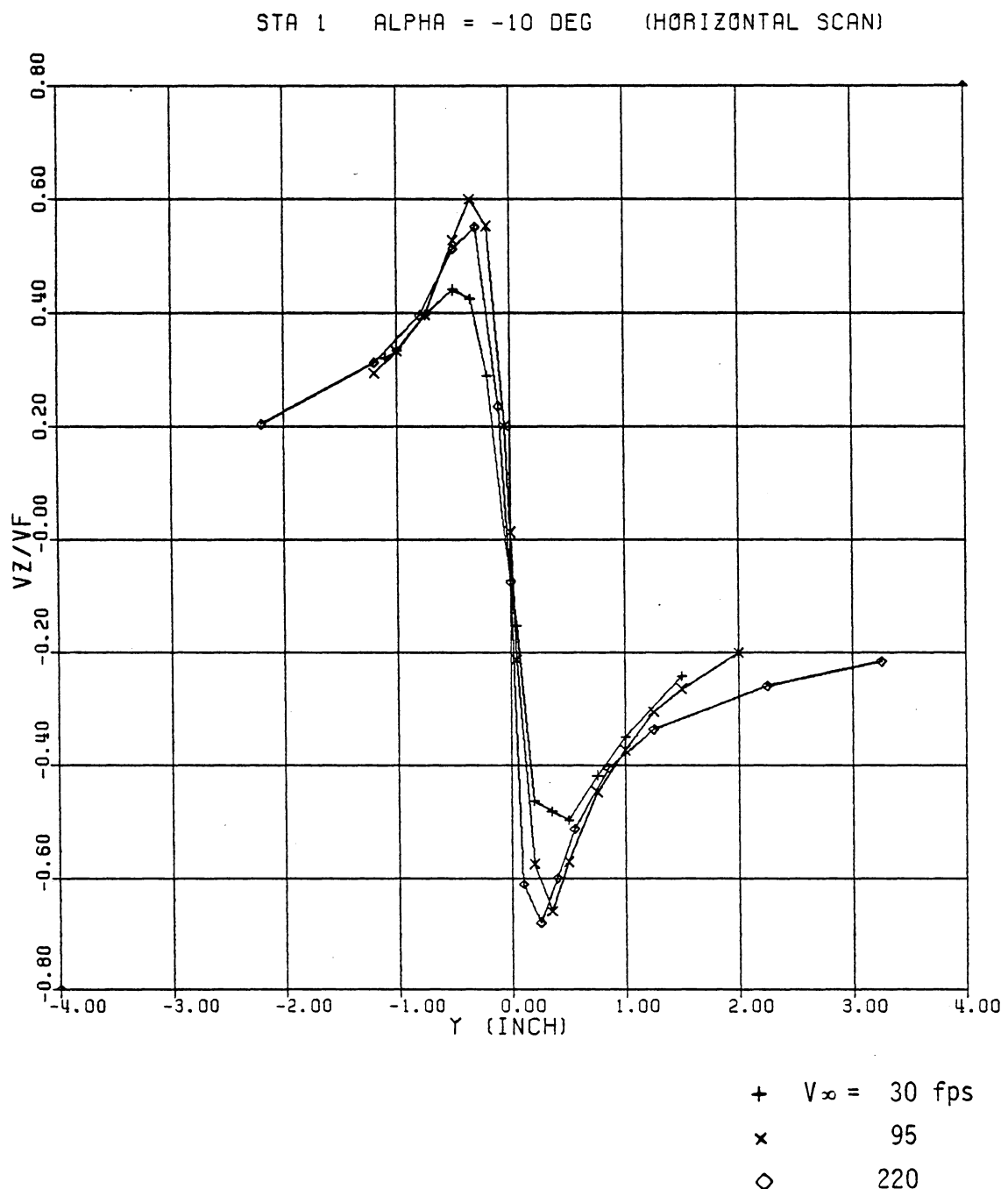


Fig. 16 Effect of Angle of Attack on Tangential Velocity
for $\alpha = -10^\circ$

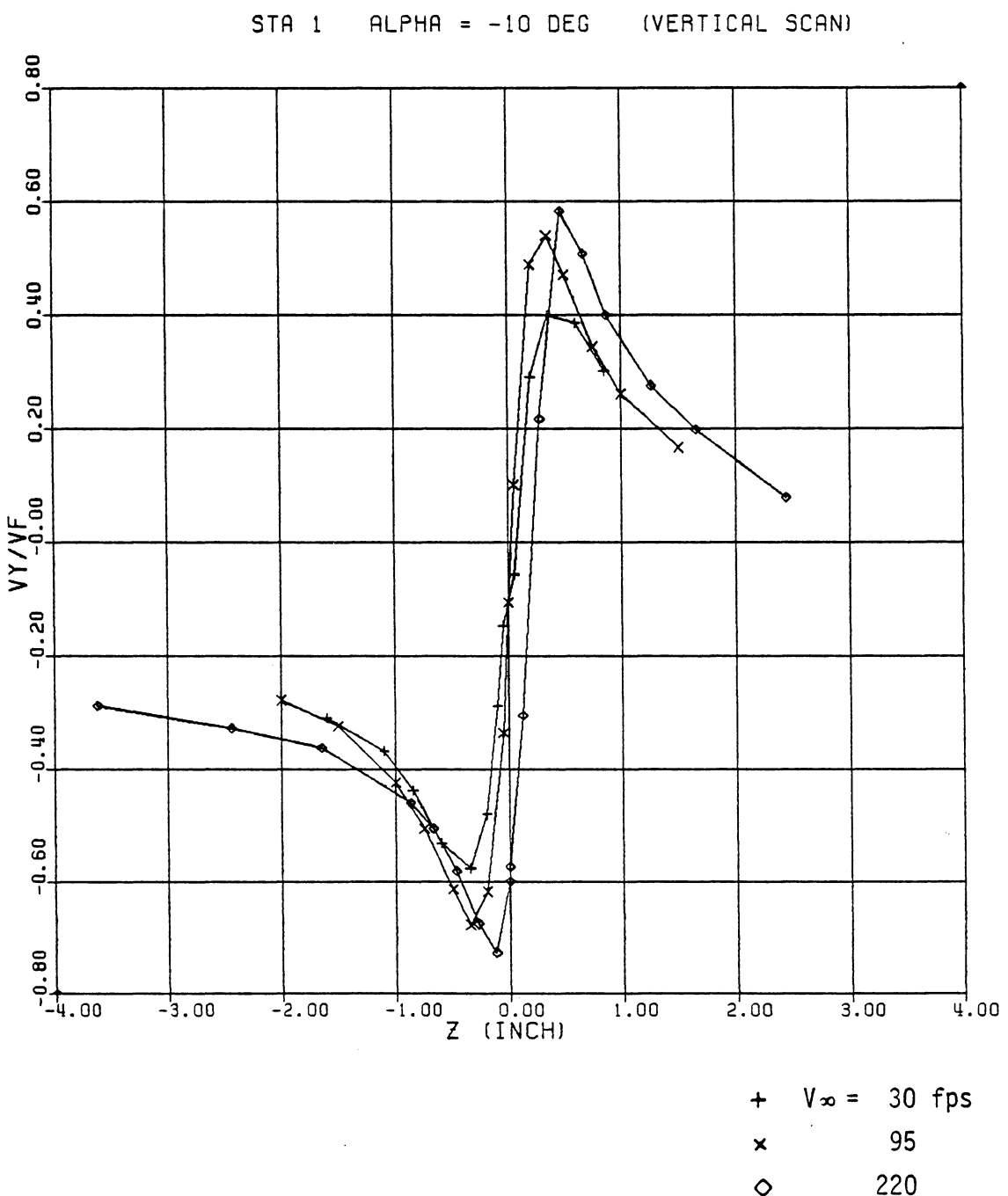


Fig. 17 Effect of Imprecise Center Measurement

CORE RADIUS

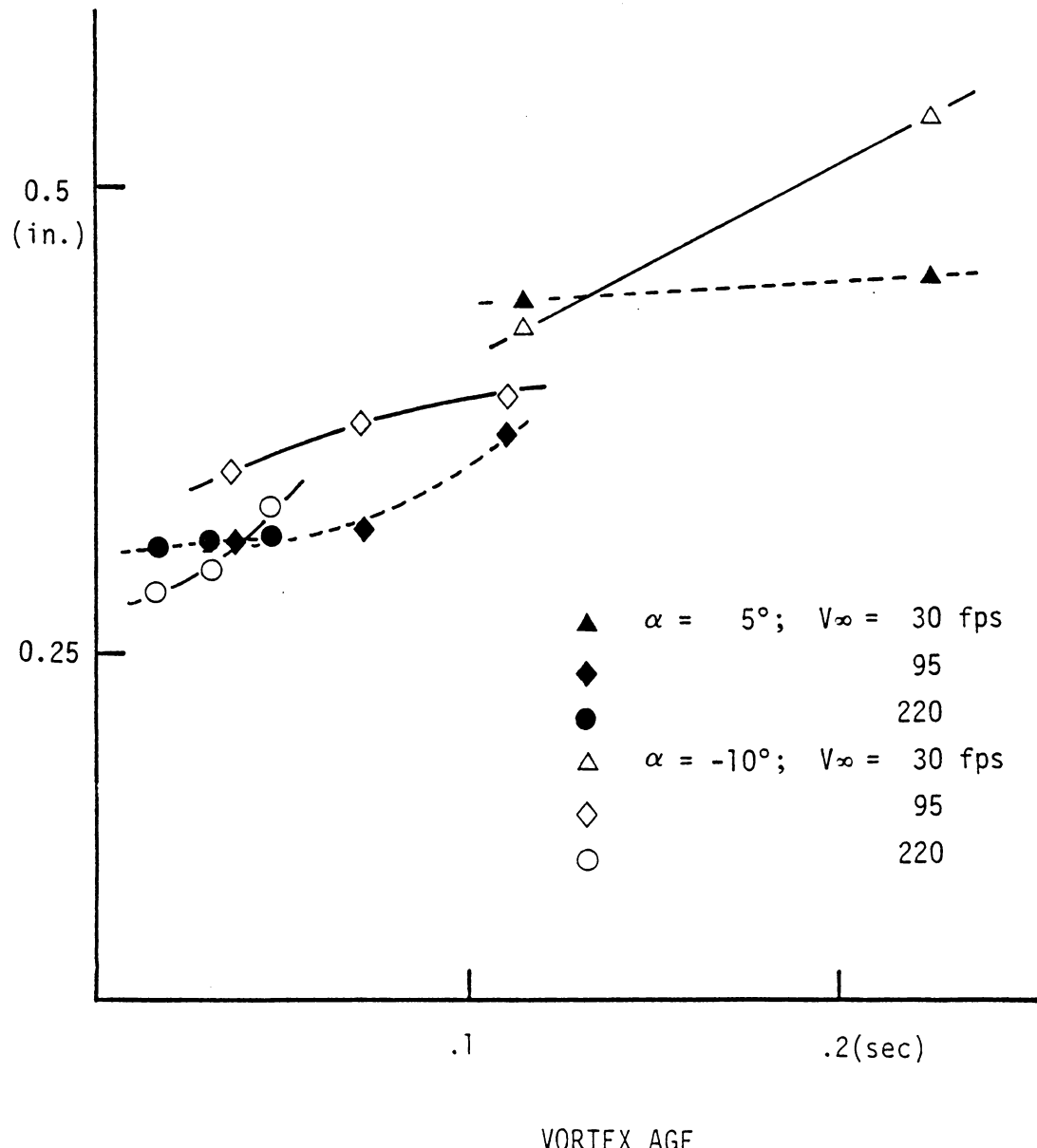


Fig. 18 Core Radius vs. Vortex Age

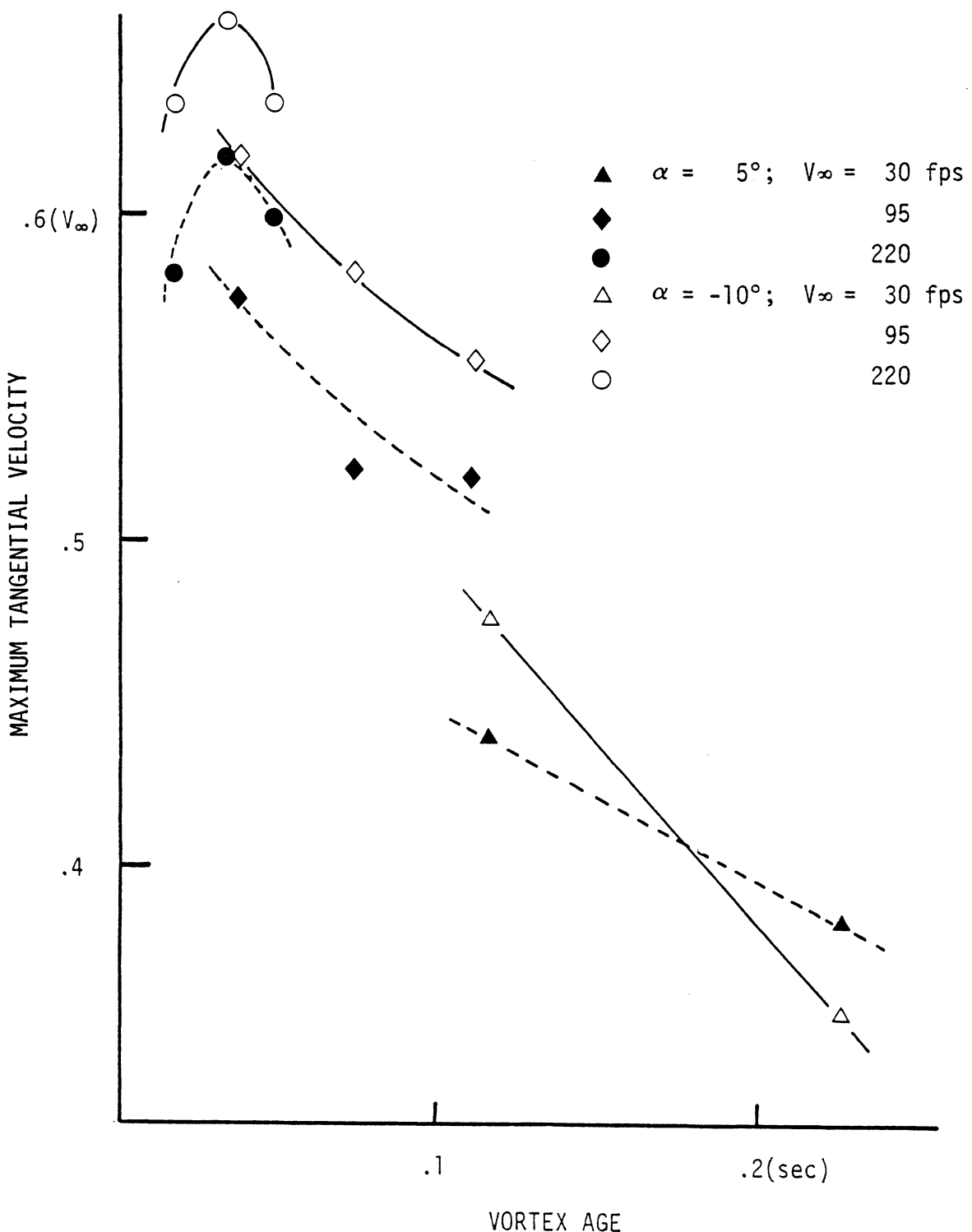


Fig. 19 Maximum Tangential Velocity vs. Vortex Age

AXIAL VELOCITY at CENTER

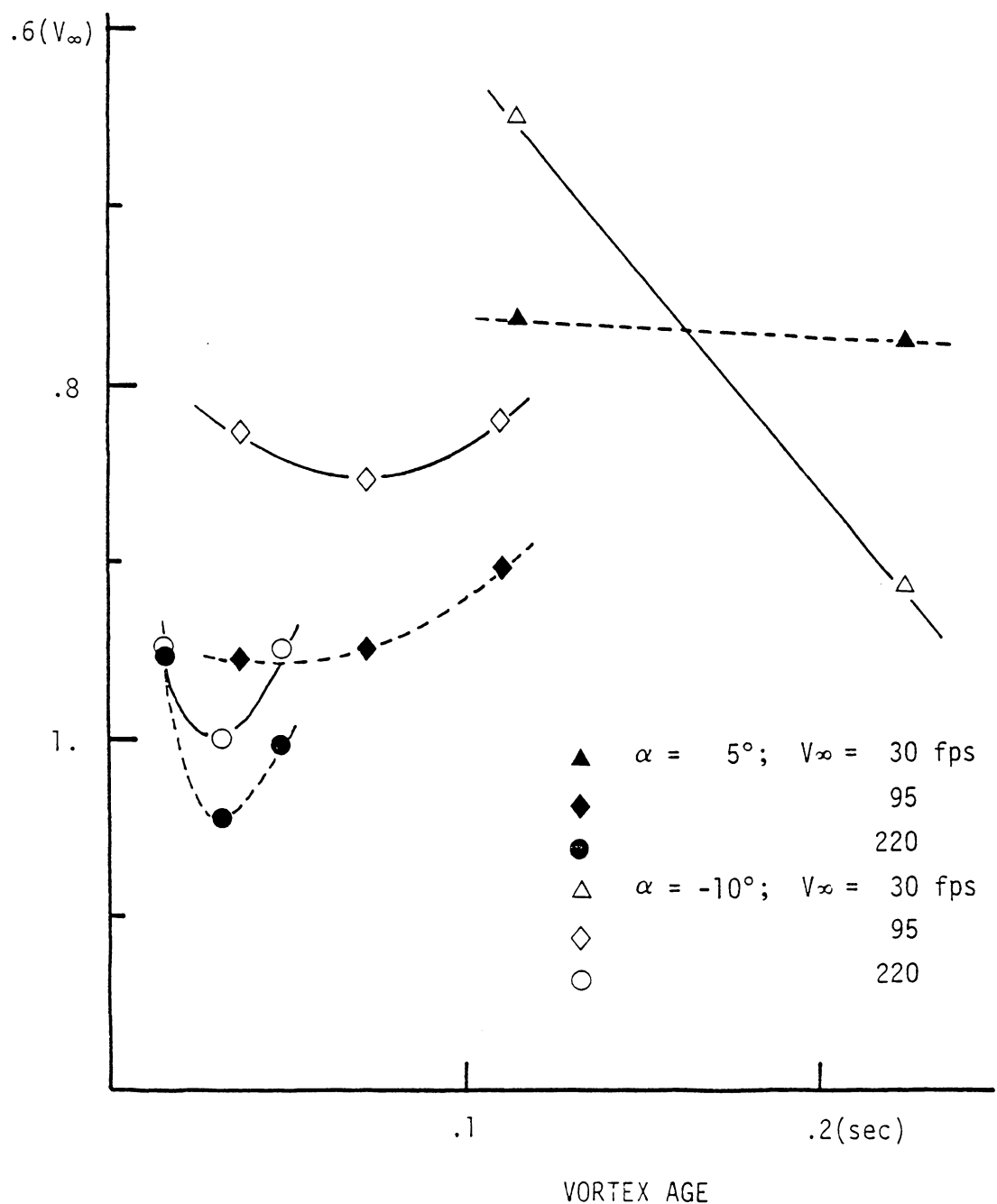


Fig. 20 Axial Velocity at Center vs. Vortex Age

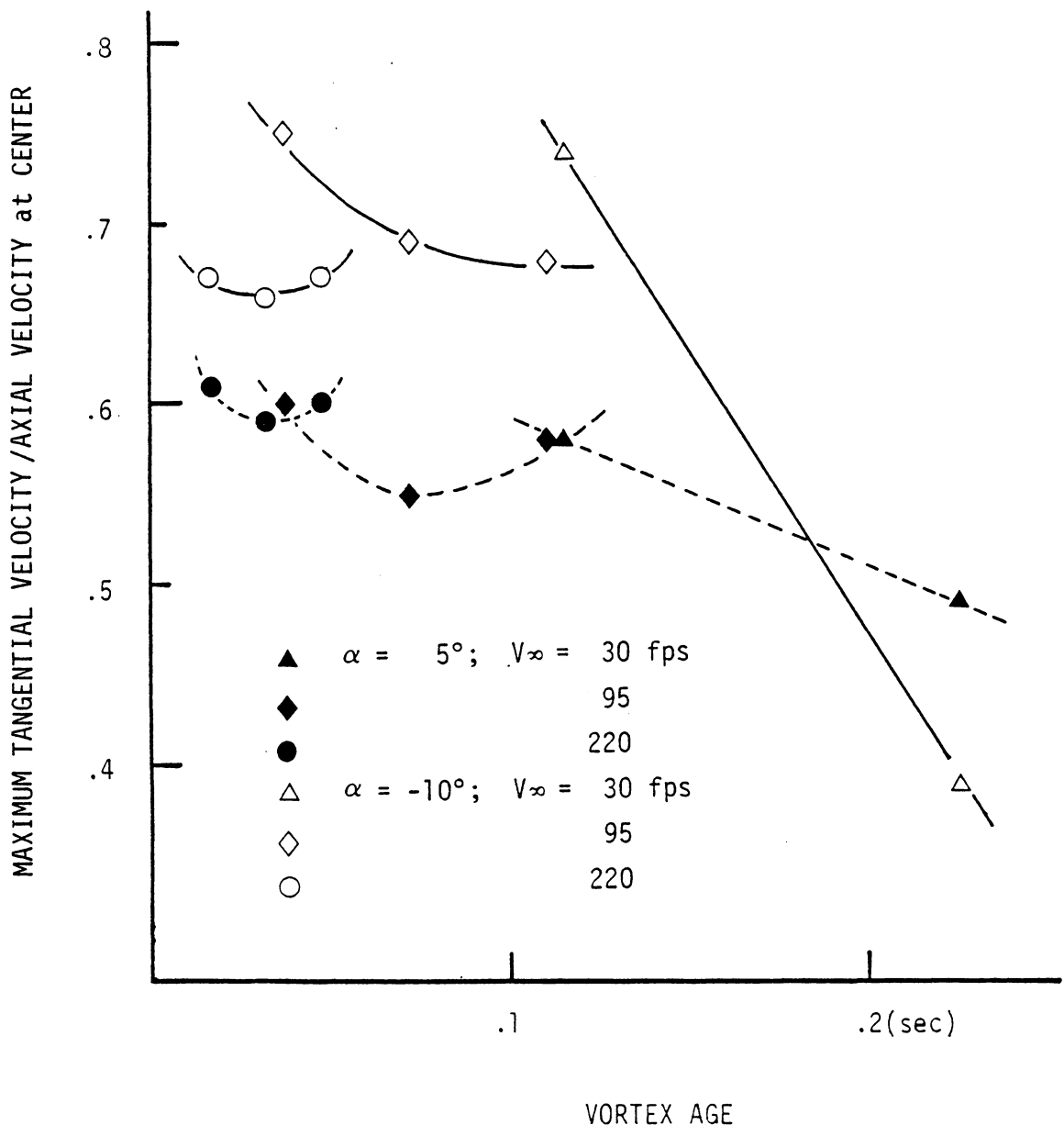


Fig. 21 Maximum Tangential Velocity/Axial Velocity at Center
vs. Vortex age

STA 2 ALPHA = -10 DEG (VERT. SCAN : HORIZ. WIRE)

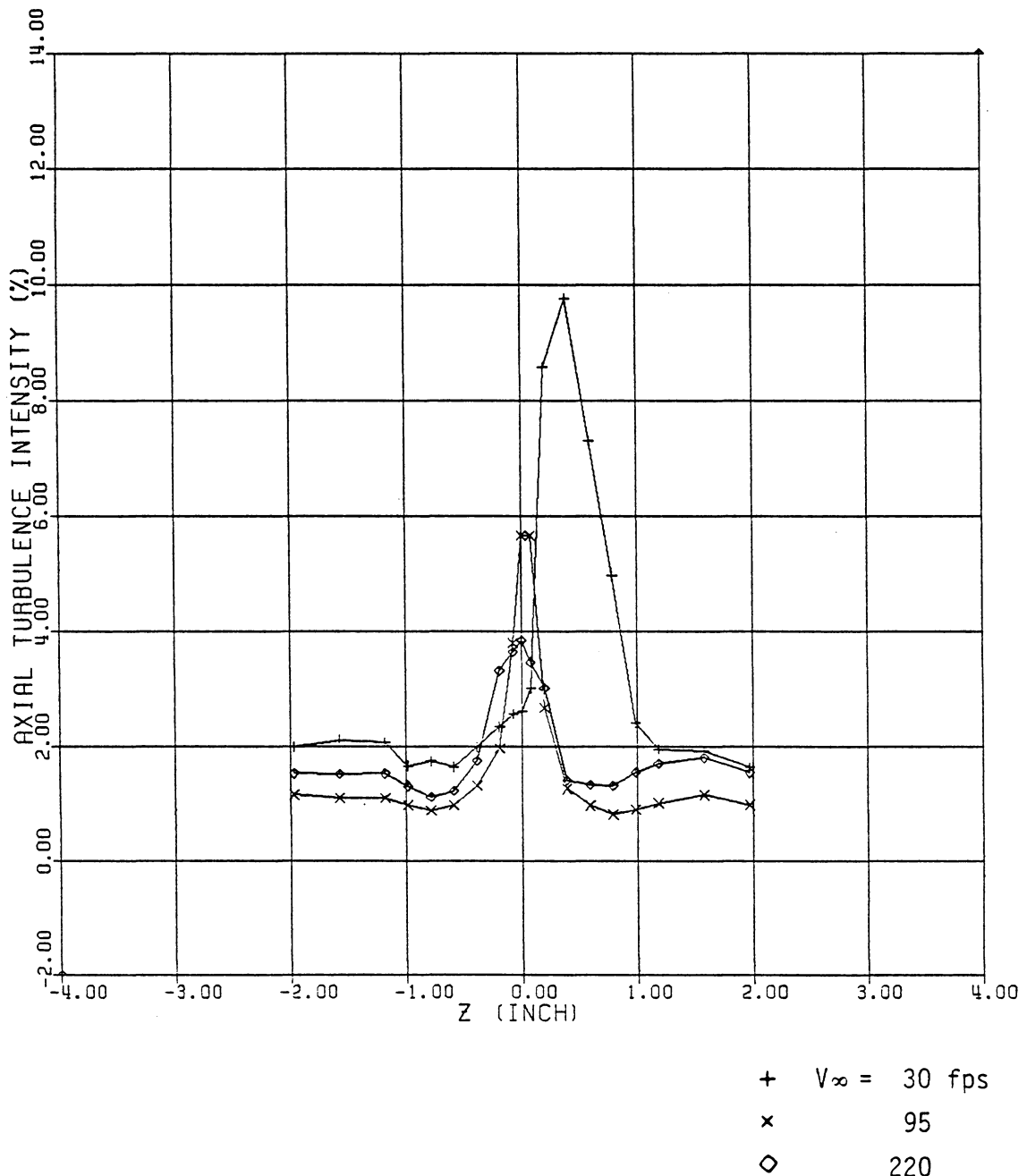


Fig. 22 Axial Turbulence Intensity Profiles at $x/c = 6$

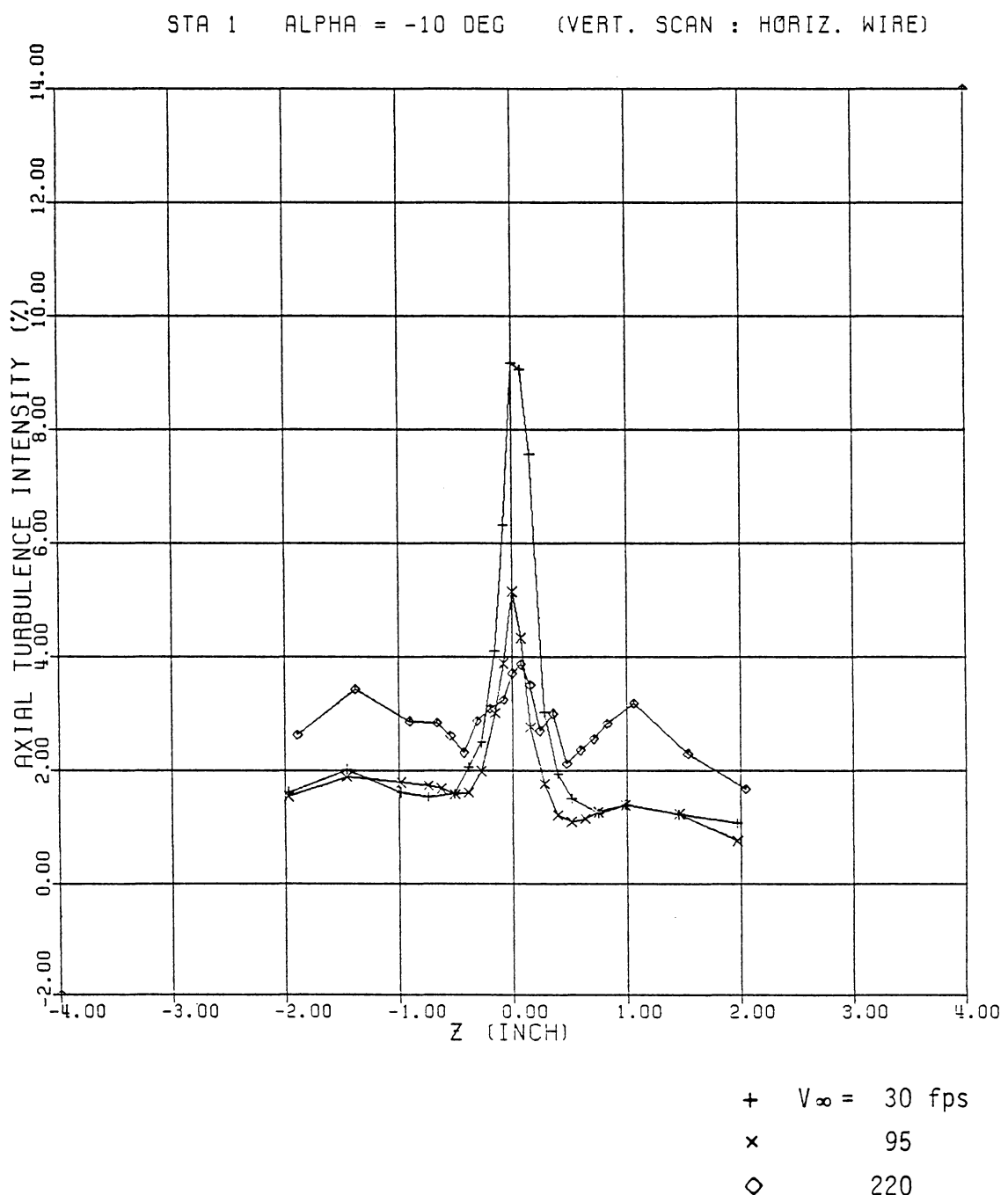
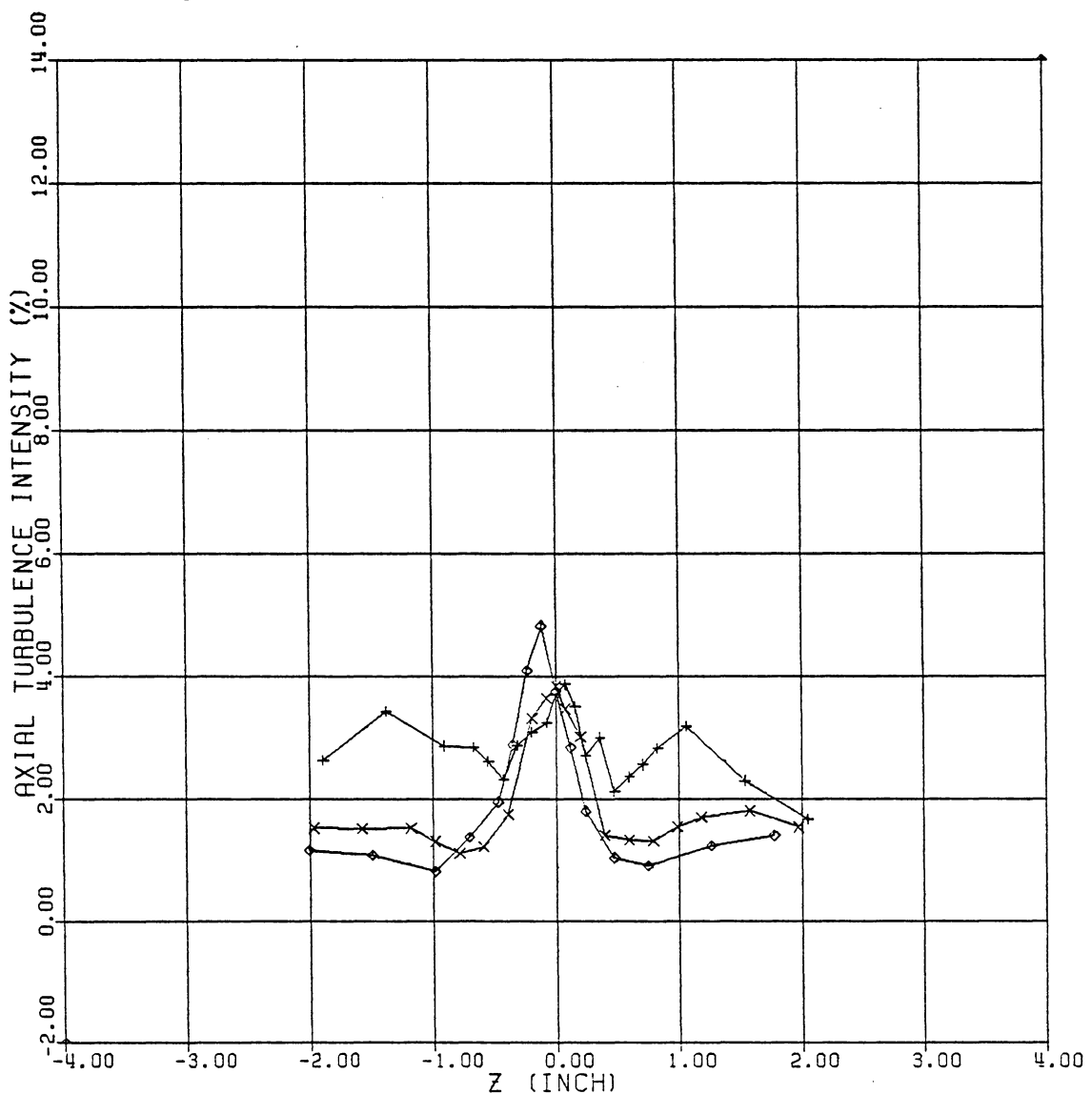


Fig. 23 Axial Turbulence Intensity Profiles at $x/c = 3$

$Q = 9.5$ $\text{ALPHA} = -10 \text{ DEG}$ (VERT. SCAN : HORIZ. WIRE)



+ $x/c = 3$
x 6
◊ 9

Fig. 24 Axial Turbulence Intensity Profiles for $V_\infty = 220$ fps

$Q = 2.0$ $\text{ALPHA} = -10 \text{ DEG}$ (HORIZ. SCAN : VERT. WIRE)

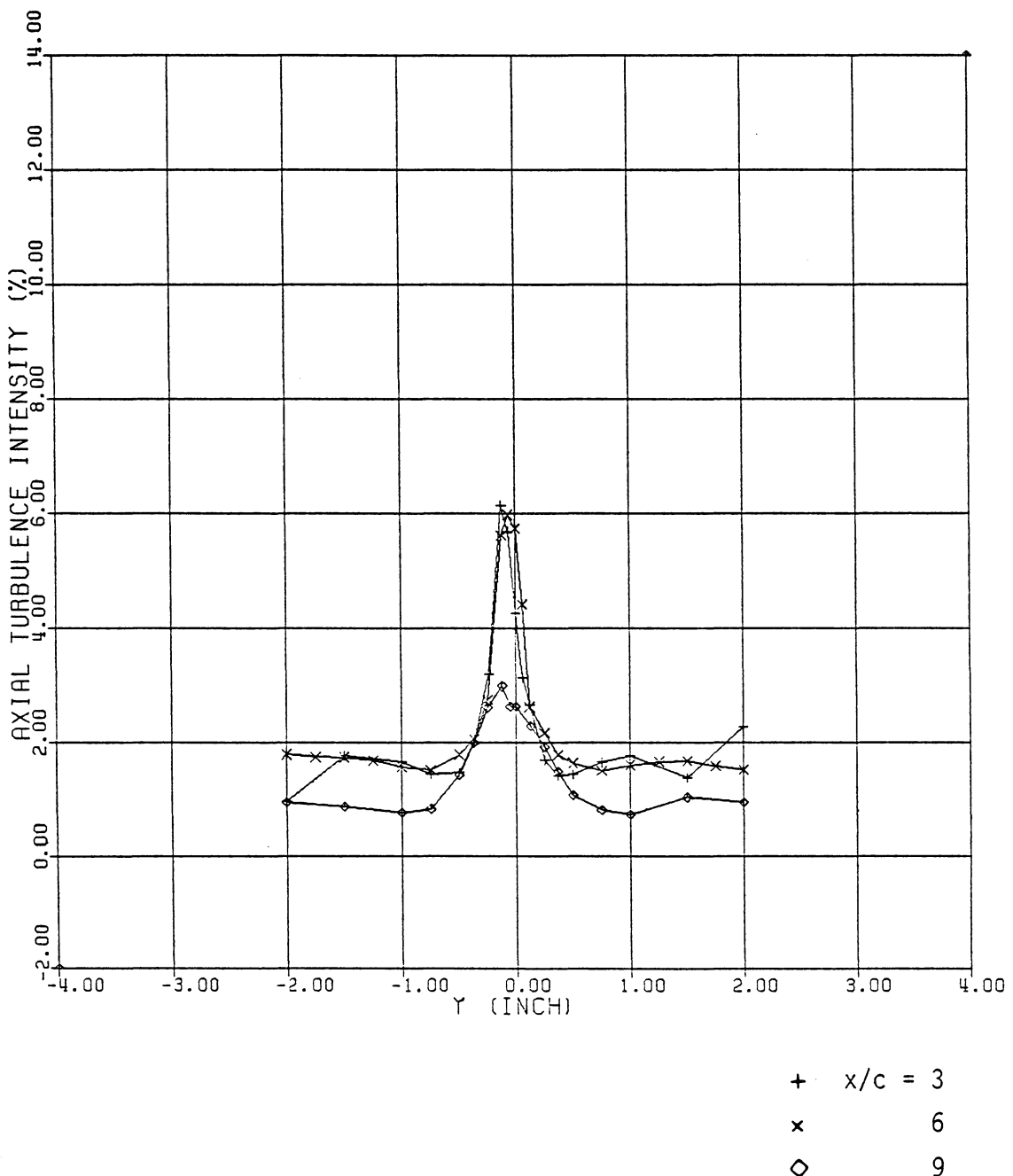


Fig. 25 Axial Turbulence Intensity Profiles for $V_\infty = 95$ fps

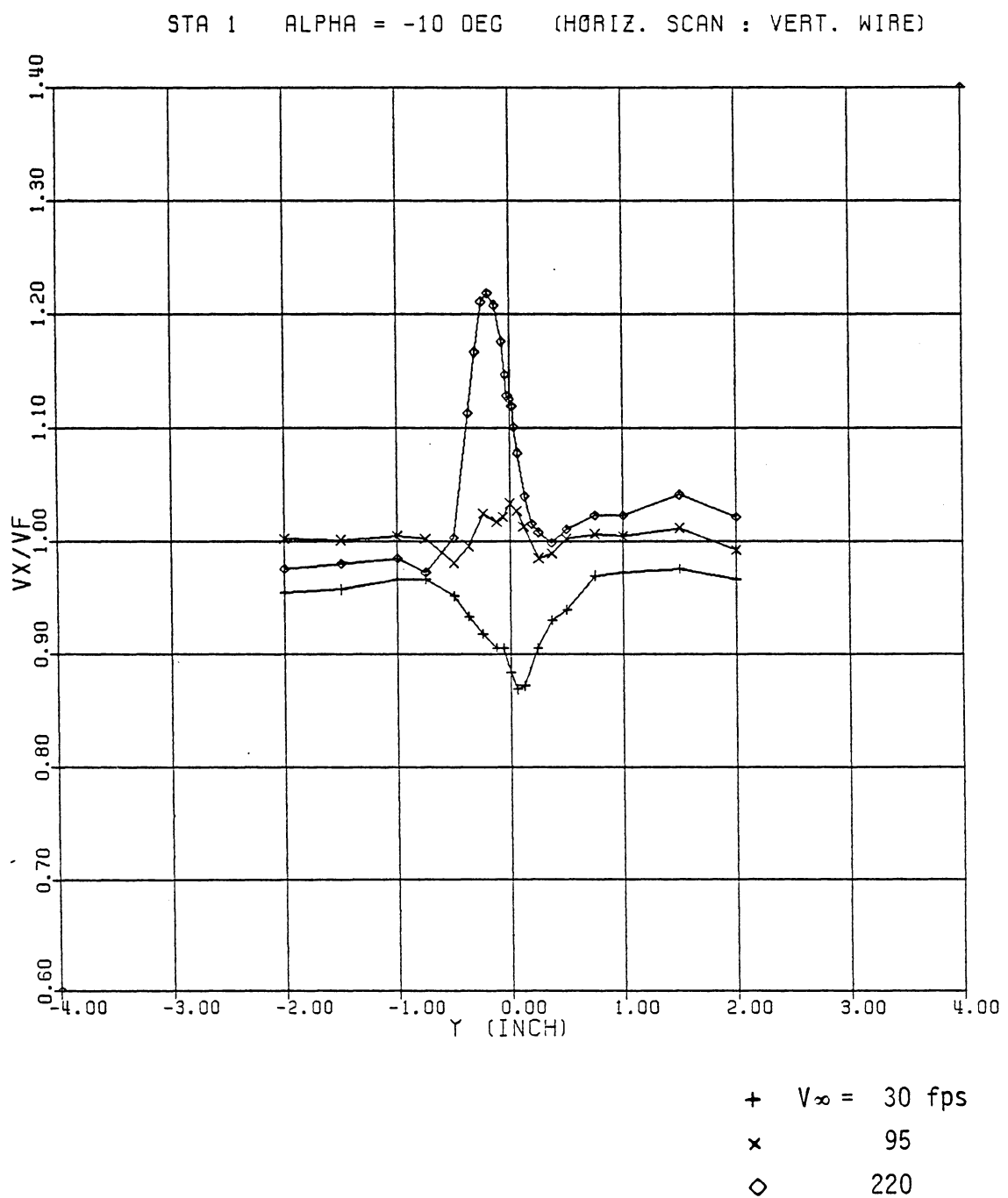


Fig. 26 Typical Mean Axial Velocity Profiles by Hot-Wire

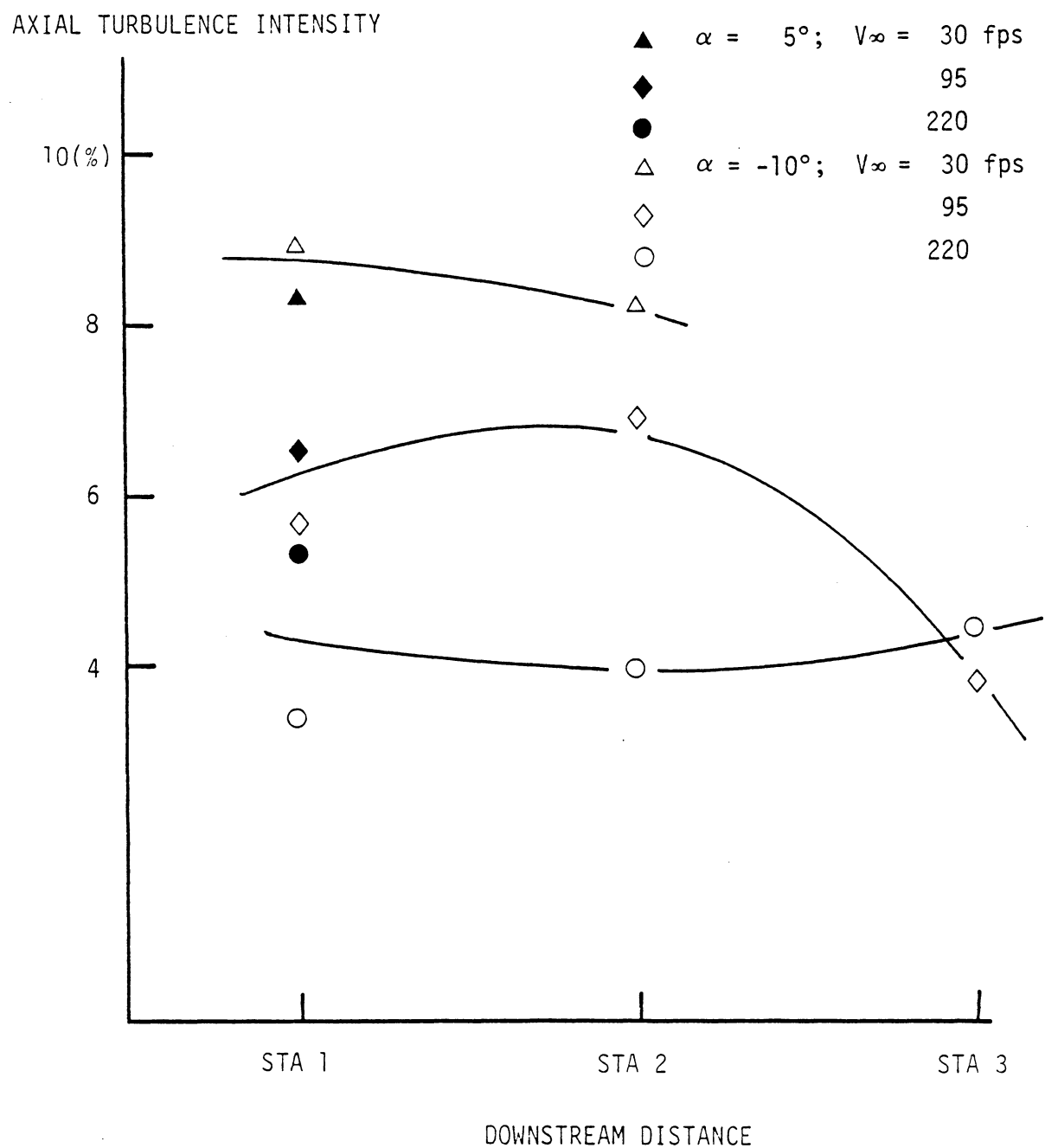
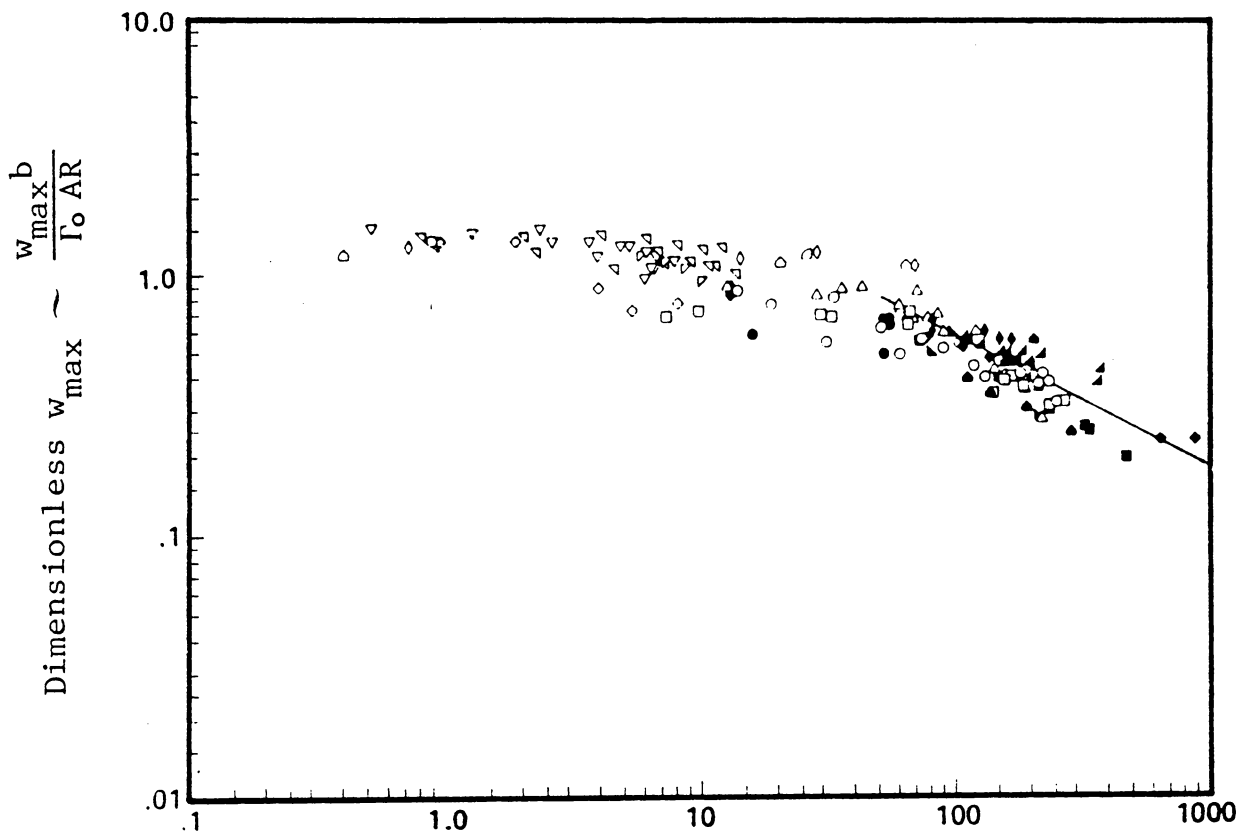


Fig. 27 Axial Turbulence Intensity at Center
vs Downstream Distance



$$\text{Dimensionless Downstream Distance} \sim \frac{x}{b} \frac{\Gamma_0}{V_\infty b} AR^2 f\left(\frac{\Gamma_0}{\nu}\right)$$

SYM	FACILITY	$\frac{\Gamma_0}{\nu}$ REYNOLDS NO.	AR ASPECT RATIO	MODEL
○	WIND TUNNEL	$3.1(10)^3$?	RECTANGULAR
○	TOW TANK	$3.9(10)^4$	5.33	RECTANGULAR
○	TOW TANK	$4.8(10)^4$	5.33	RECTANGULAR
△	TOW TANK	$7.7(10)^4$	5.33	RECTANGULAR
▽	WIND TUNNEL	$3.4(10)^4 - 7.2(10)^4$	12	RECTANGULAR
▽	WIND TUNNEL	$5.0(10)^4 - 10.6(10)^4$	12	RECTANGULAR
▽	WIND TUNNEL	$8.7(10)^4 - 14.4(10)^4$	17	RECTANGULAR
▽	WIND TUNNEL	$1.4(10)^5$	5.33	RECTANGULAR
□	WIND TUNNEL	$4.3(10)^5$	5.33	RECTANGULAR
□	WIND TUNNEL	$9.5(10)^5$	5.33	RECTANGULAR
▼	FLIGHT	$1.3(10)^6$	5.82	CHEROKEE
▲	FLIGHT	$1.4(10)^6$	7.45	O-1
◆	FLIGHT	$1.5(10)^6$	5.82	CHEROKEE
◆	FLIGHT	$1.9(10)^6$	5.82	CHEROKEE
◆	FLIGHT	$3.5(10)^6$	6.12	P-51
■	FLIGHT	$9.4(10)^6 - 1.3(10)^7$	6.22	COMET HI
●	FLIGHT	$1.1(10)^7$	7.33	DC-8
●	FLIGHT	$1.9(10)^7$	7.94	CS-A

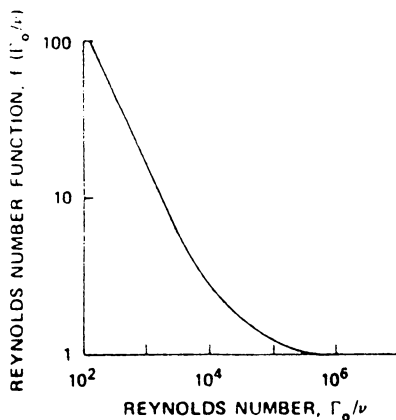
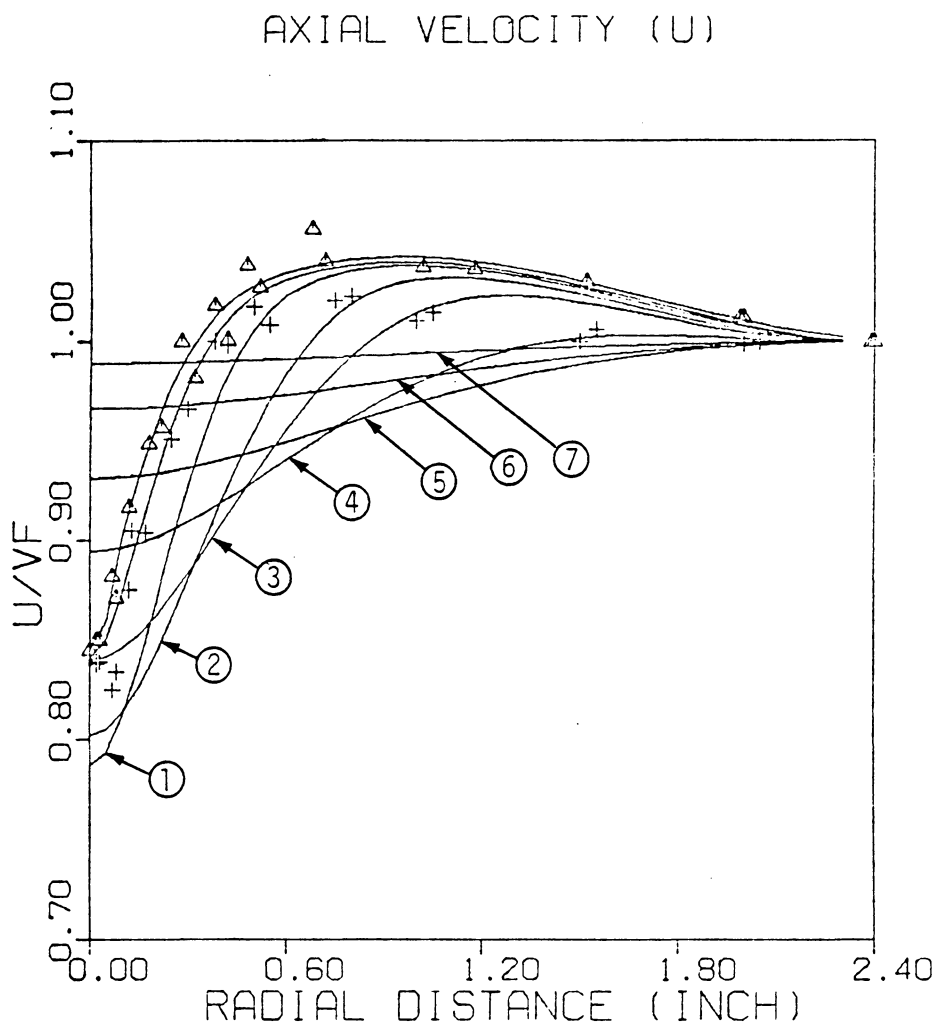


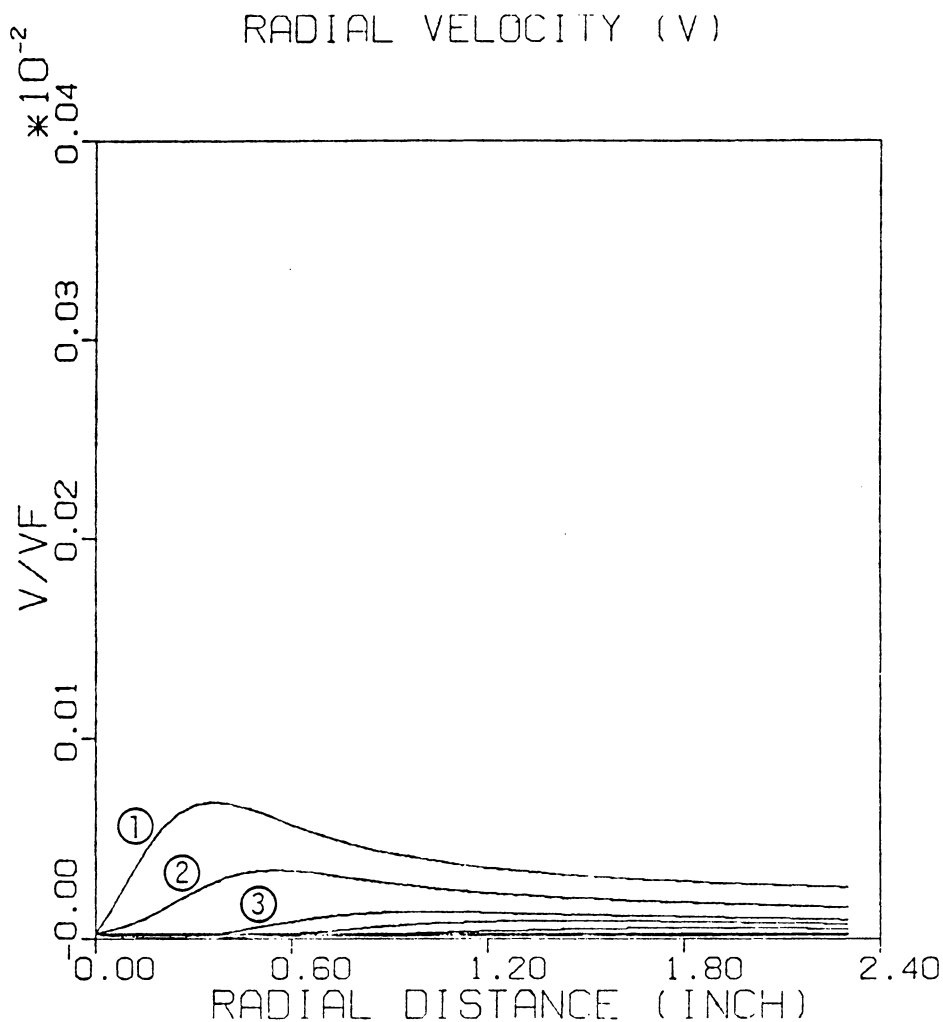
Fig. 28 Maximum Tangential Velocity Correlation

by Iversen (Ref. 7)



<u>Measurement</u>	<u>Prediction</u>
$\Delta \quad x = 7.0 \text{ ft}$	① $x = 30 \text{ ft}$
$+\quad 10.5$	② 100
	③ 200
	④ 500
	⑤ 1000
	⑥ 2000
	⑦ 4000

Fig. 29 Axial Velocity Decay for $V_\infty = 95 \text{ fps}$ with
Constant Eddy Viscosity Coefficient

Prediction

- (1) $x = 30$ ft
- (2) 100
- (3) 200

Fig. 30 Radial Velocity Decay for $V_\infty = 95$ fps with
Constant Eddy Viscosity Coefficient

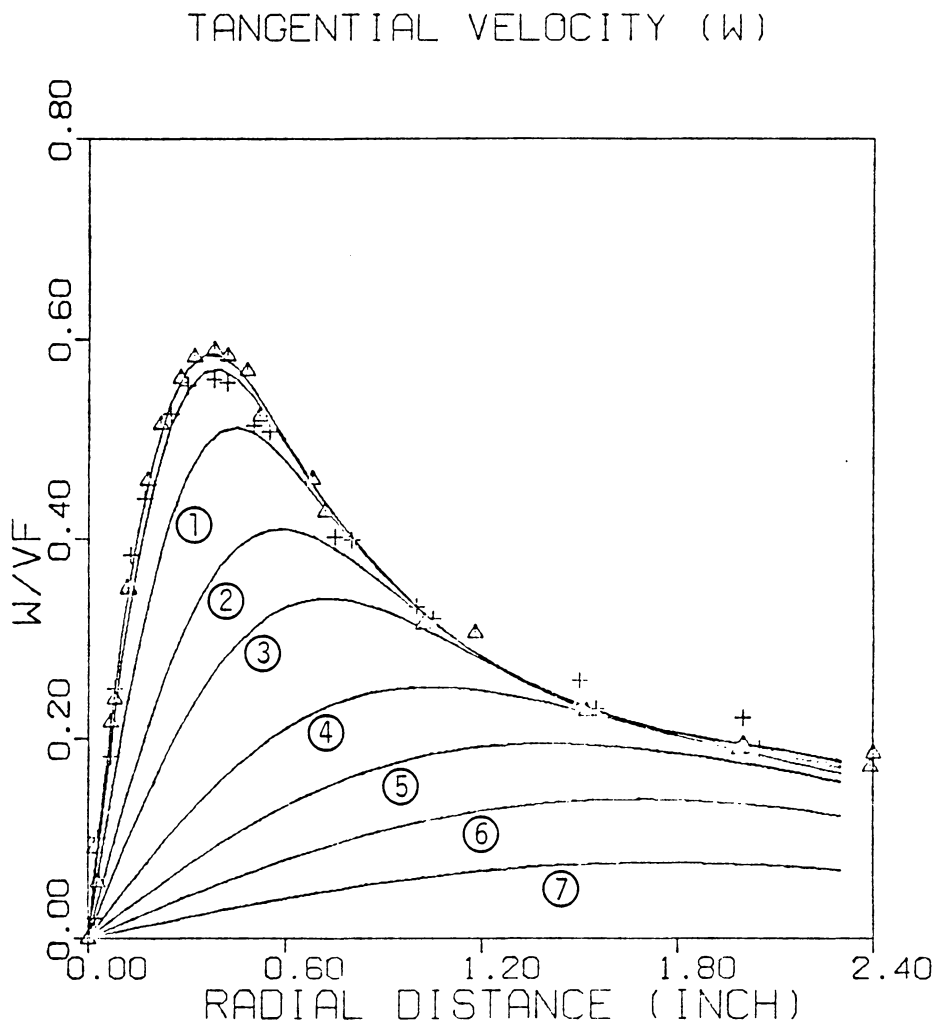
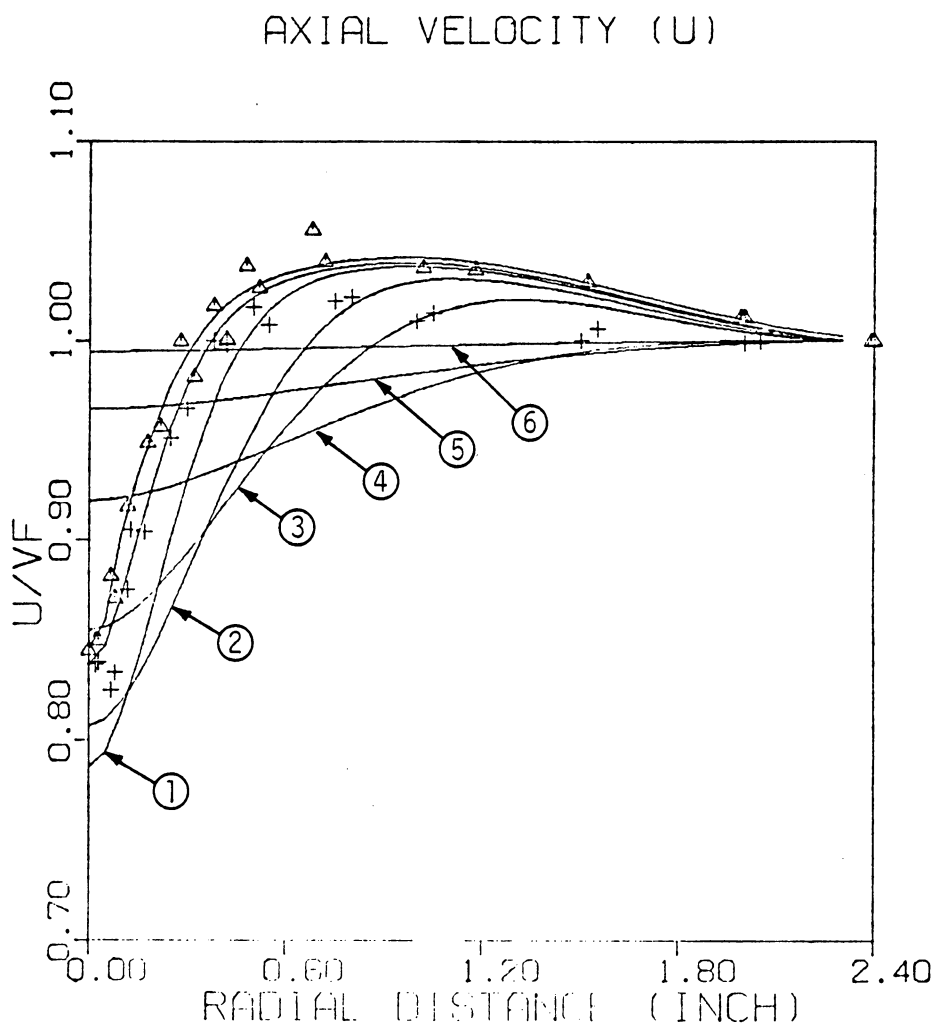
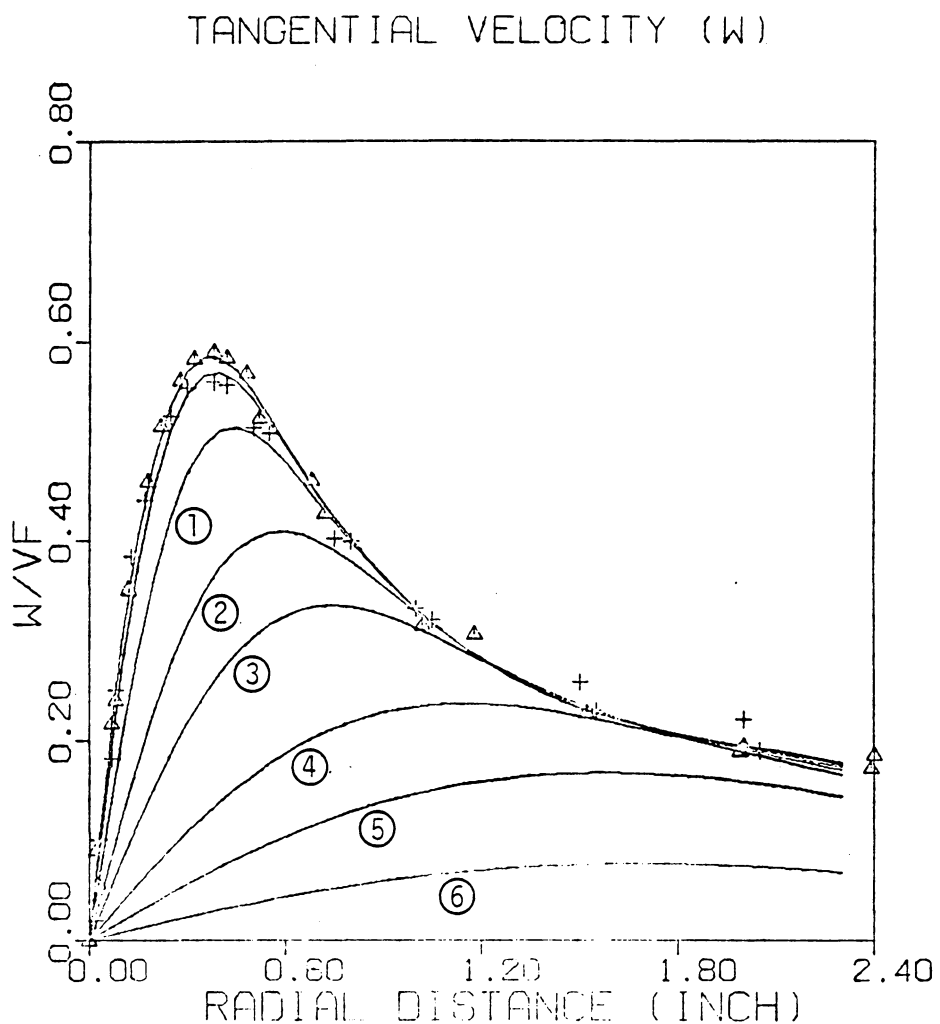


Fig. 31 Tangential Velocity Decay for $V_{\infty} = 95$ fps with
Constant Eddy Viscosity Coefficient



<u>Measurement</u>	<u>Prediction</u>
$\Delta \quad x = 7.0 \text{ ft}$	① $x = 30 \text{ ft}$
$+\quad 10.5$	② 100
	③ 200
	④ 500
	⑤ 1000
	⑥ 2000

Fig. 32 Axial Velocity Decay for $V_\infty = 95 \text{ fps}$ with Axially Varying Eddy Viscosity Coefficient



<u>Measurement</u>	<u>Prediction</u>
$\Delta \quad x = 7.0 \text{ ft}$	(1) $x = 30 \text{ ft}$
$+ \quad 10.5$	(2) 100
	(3) 200
	(4) 500
	(5) 1000
	(6) 2000

Fig. 33 Tangential Velocity Decay for $V_\infty = 95 \text{ fps}$ with Axially Varying Eddy Viscosity Coefficient

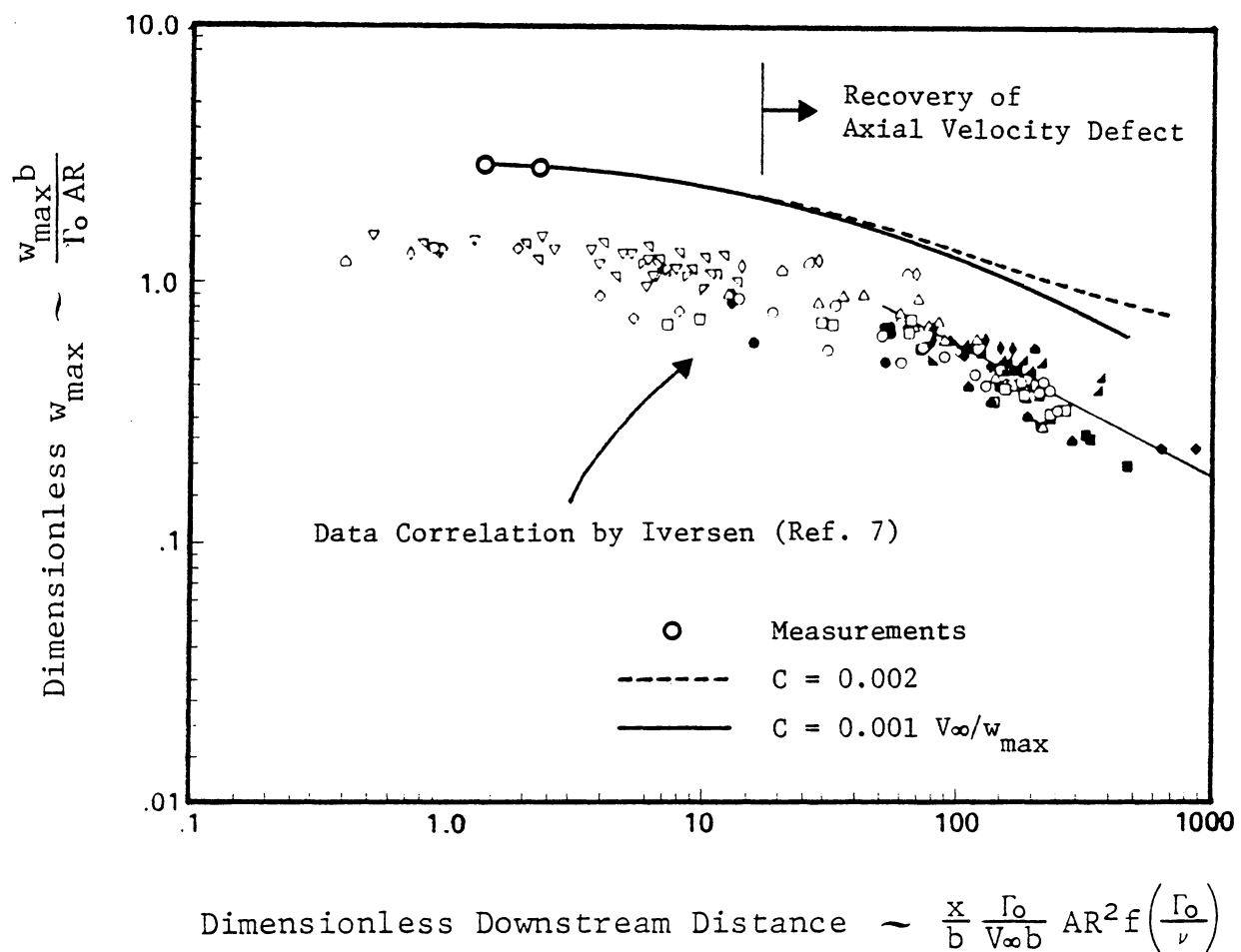
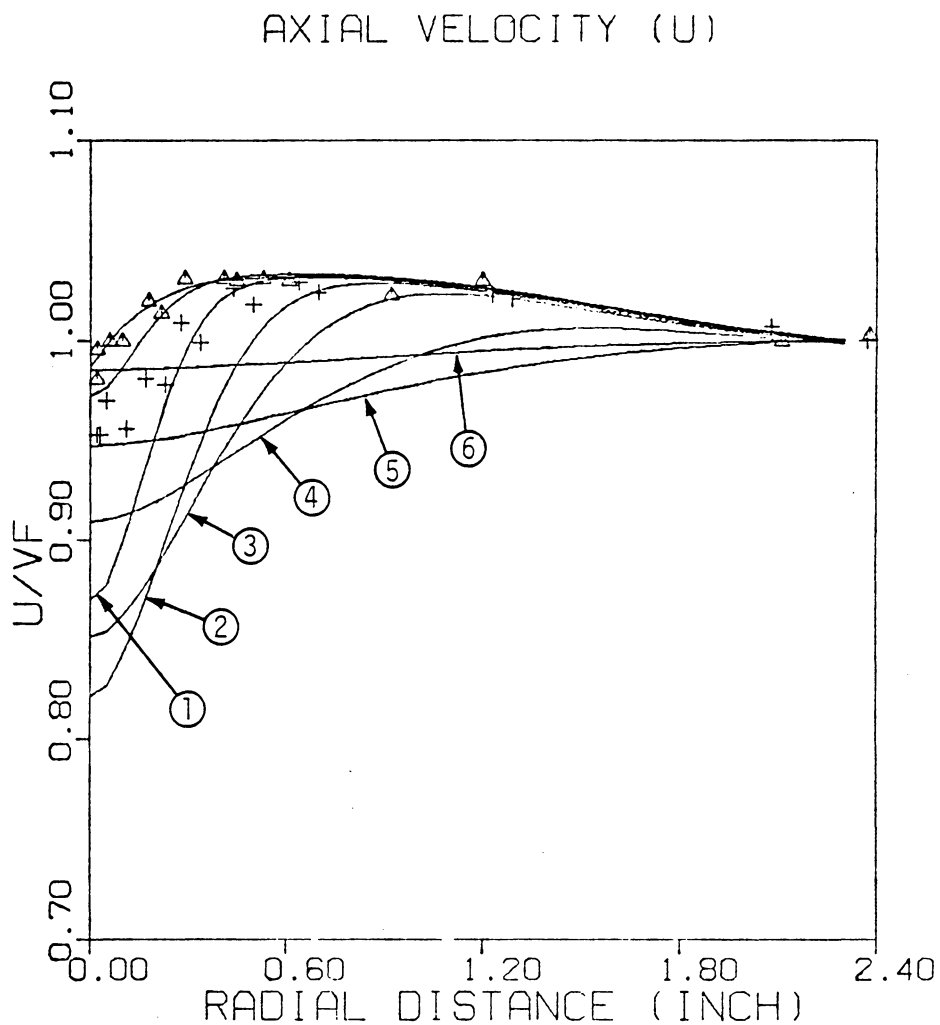


Fig. 34 Effect of Eddy Viscosity Coefficient on w_{\max} Decay
for $V_\infty = 95$ fps

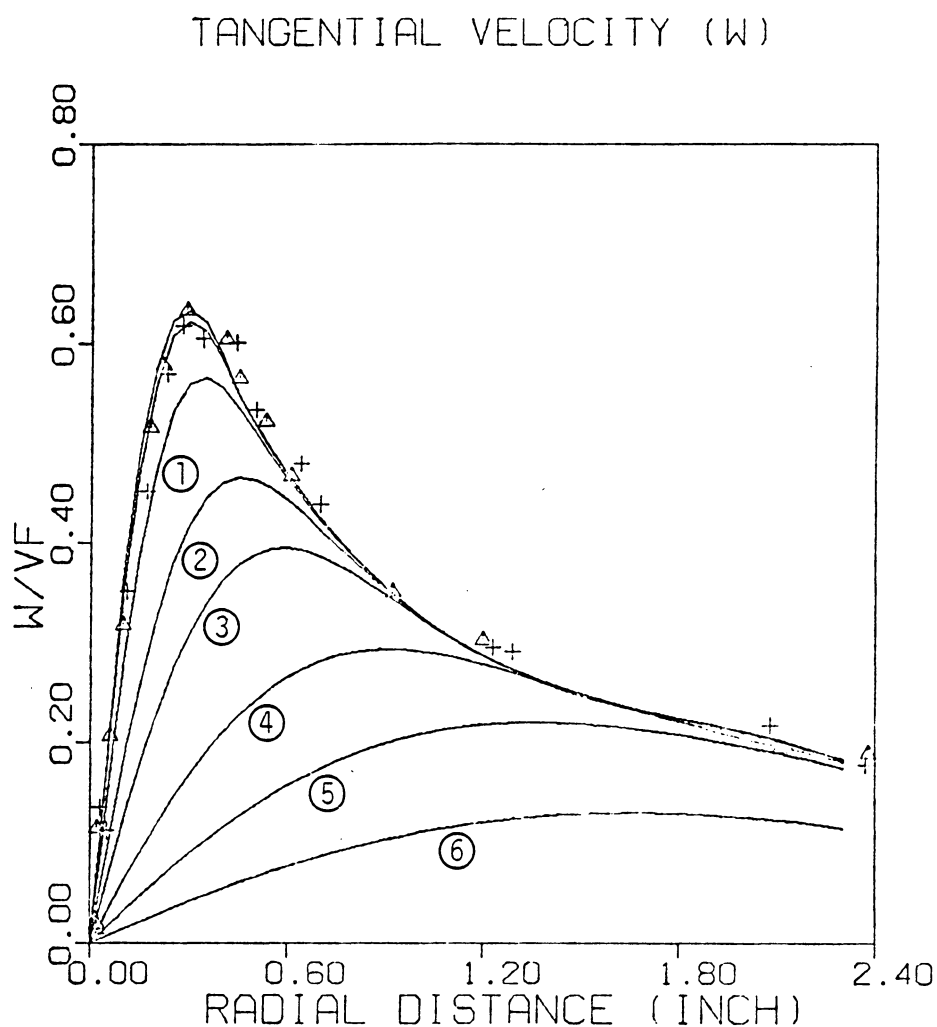
Measurement

\triangle $x = 7.0 \text{ ft}$
 $+$ 10.5

Prediction

(1)	$x = 30 \text{ ft}$
(2)	100
(3)	200
(4)	500
(5)	1000
(6)	2000

Fig. 35 Axial Velocity Decay for $V_\infty = 220 \text{ fps}$



<u>Measurement</u>	<u>Prediction</u>
$\Delta \quad x = 7.0 \text{ ft}$	① $x = 30 \text{ ft}$
$+ \quad 10.5$	② 100
	③ 200
	④ 500
	⑤ 1000
	⑥ 2000

Fig. 36 Tangential Velocity Decay for $V_\infty = 220 \text{ fps}$

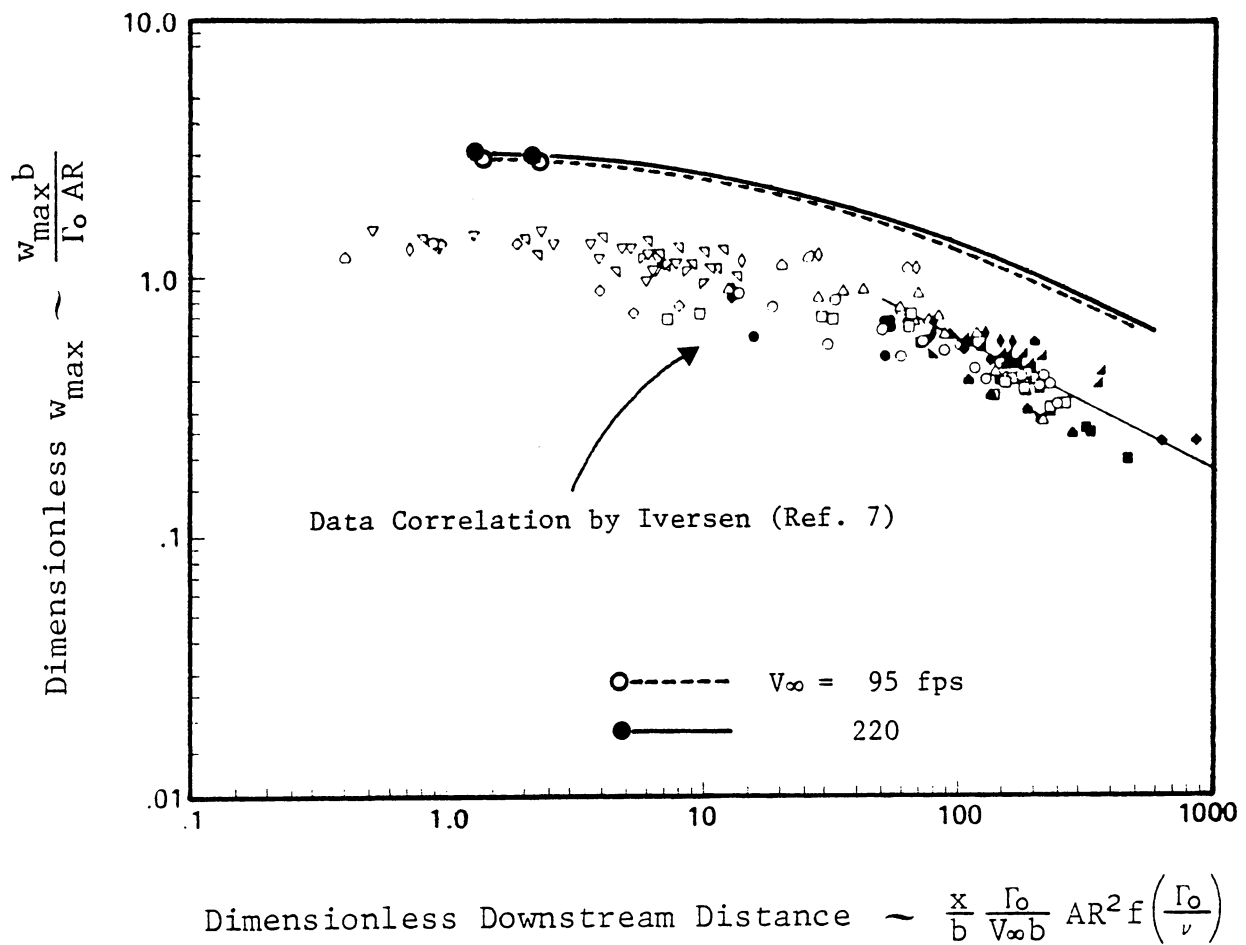


Fig. 37 Effect of Reynolds Number on w_{\max} Decay with Axially Varying Eddy Viscosity Coefficient

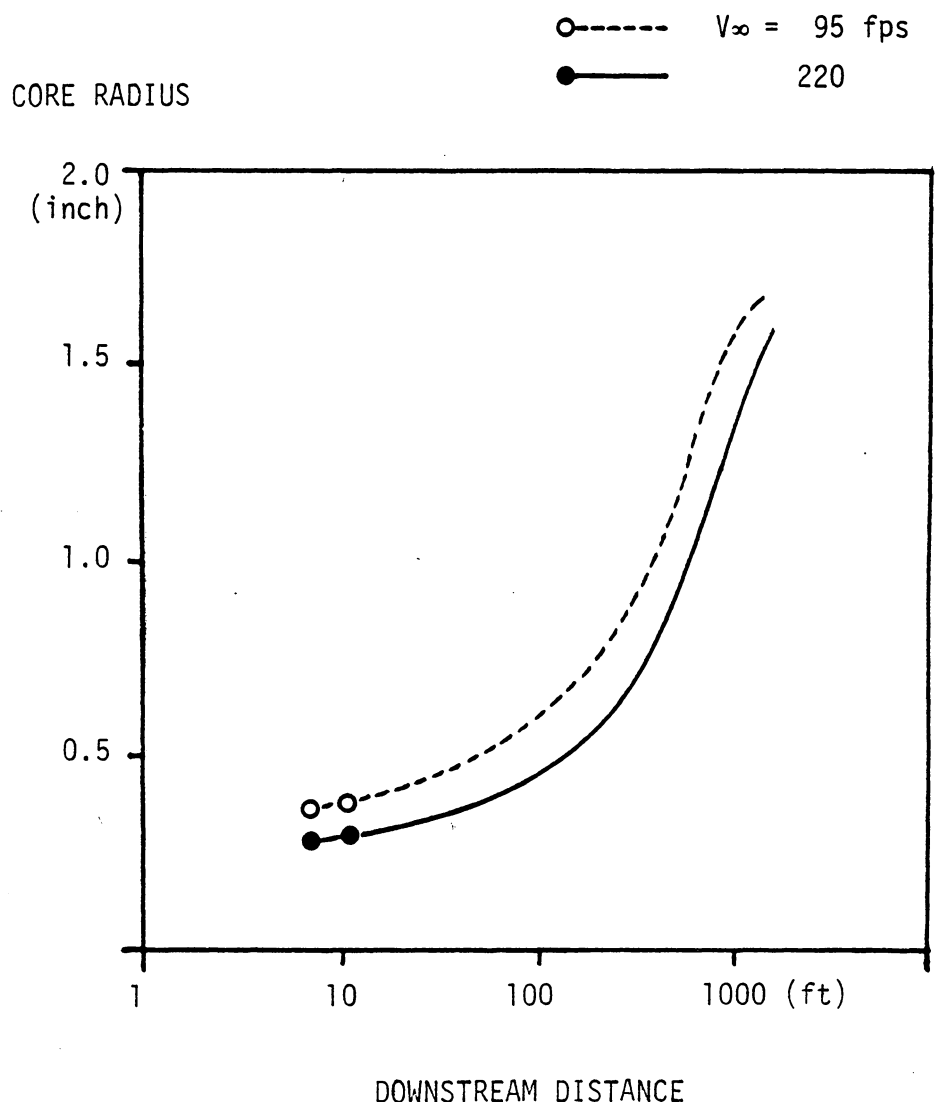
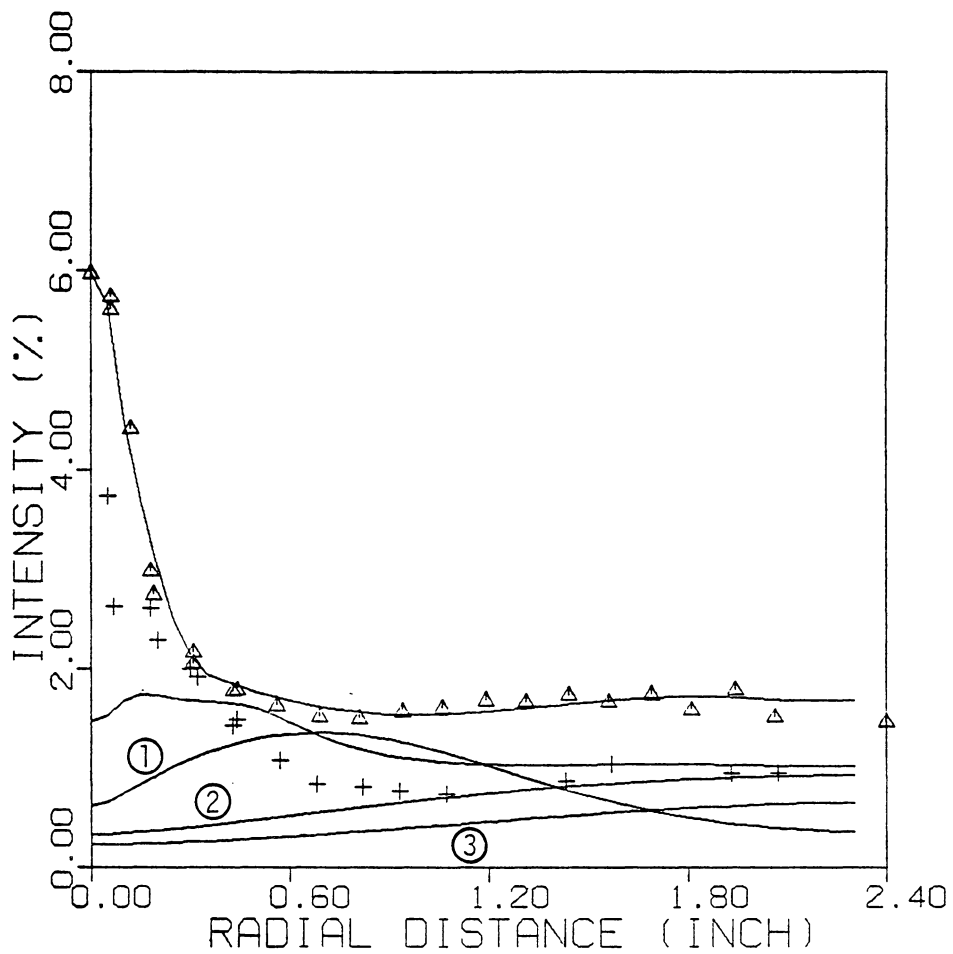


Fig. 38 Growth of Core Radius

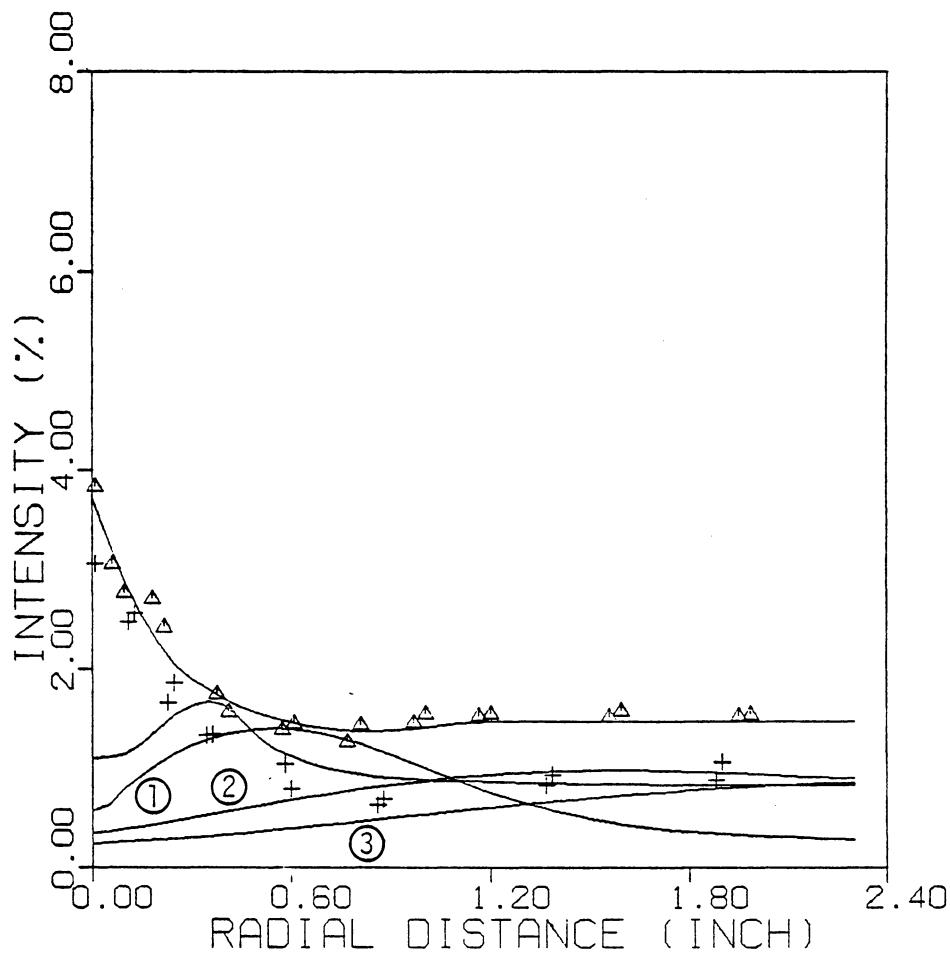
TURBULENT INTENSITY (ATI)



<u>Measurement</u>	<u>Prediction</u>
$\Delta \quad x = 7.0 \text{ ft}$	(1) $x = 200 \text{ ft}$
$+$ 10.5	(2) 1000
	(3) 2000

Fig. 39 Axial Turbulence Intensity Decay for $V_\infty = 95$ fps

TURBULENT INTENSITY (ATI)

Measurement

Δ $x = 7.0$ ft
+ 10.5

Prediction

① $x = 200$ ft
② 1000
③ 2000

Fig. 40 Axial Turbulence Intensity Decay for $V_\infty = 220$ fps

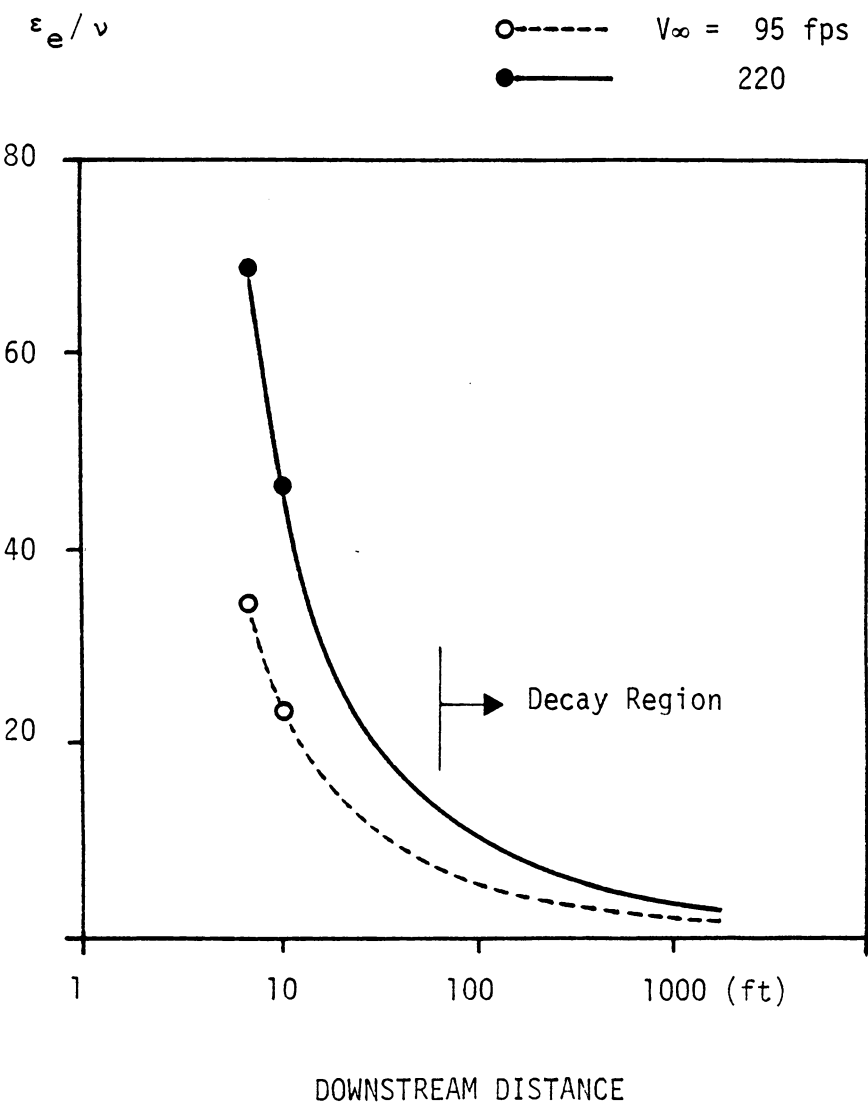
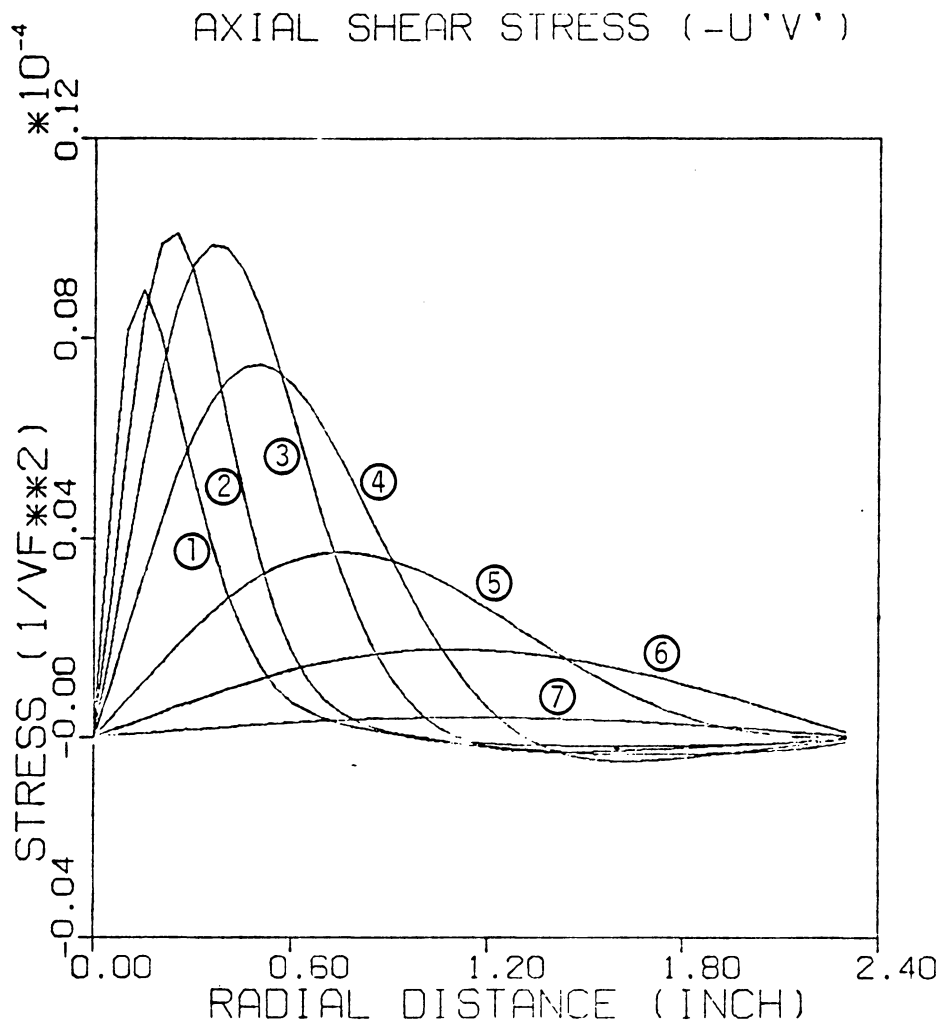


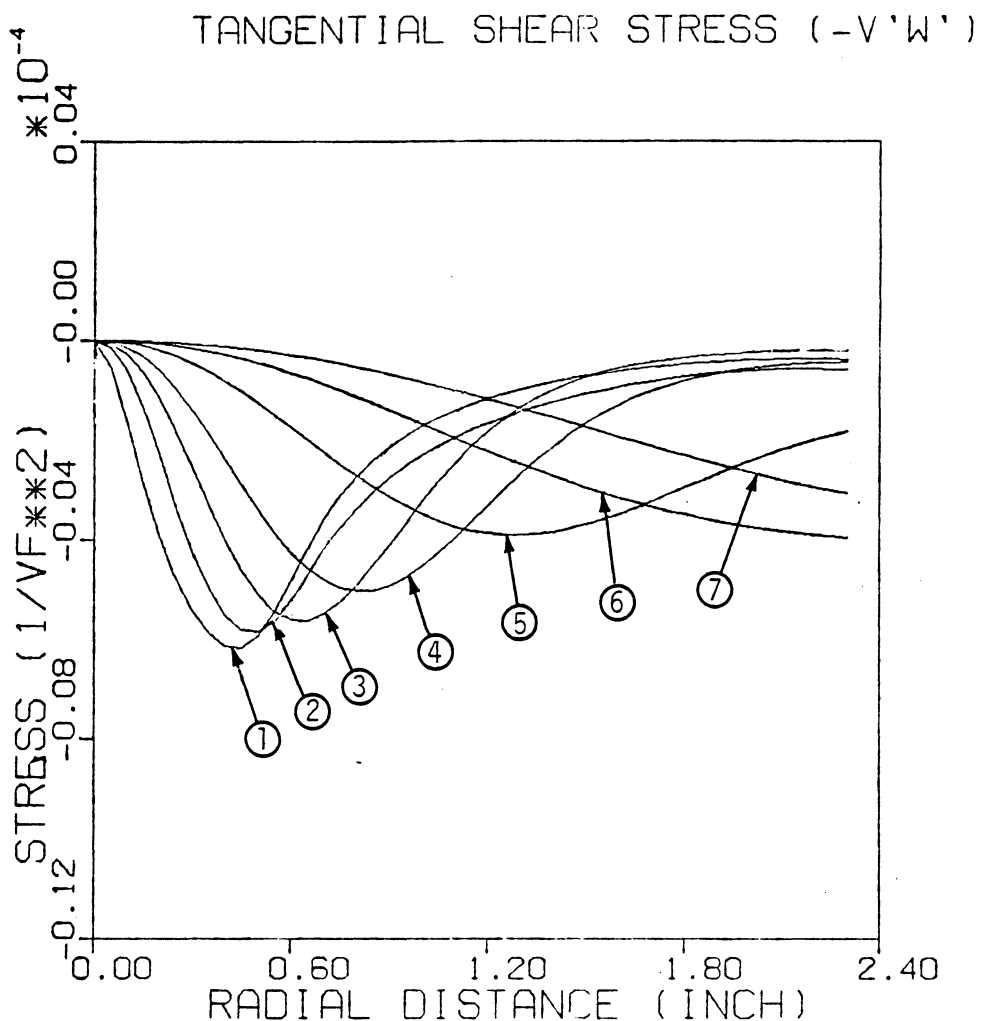
Fig. 41 Decay of Effective Eddy Viscosity



Prediction

- | | |
|-----|-----------|
| (1) | x = 10 ft |
| (2) | 30 |
| (3) | 100 |
| (4) | 200 |
| (5) | 500 |
| (6) | 1000 |
| (7) | 2000 |

Fig. 42 Axial Shear Stress Decay for $V_\infty = 220$ fps



Prediction

- | | |
|-----|---------------------|
| (1) | $x = 10 \text{ ft}$ |
| (2) | 30 |
| (3) | 100 |
| (4) | 200 |
| (5) | 500 |
| (6) | 1000 |
| (7) | 2000 |

Fig. 43 Tangential Shear Stress Decay for $V_\infty = 220 \text{ fps}$

Appendix A

CALIBRATION OF THE YAW-HEAD PROBE

The calibration of the five-port, yaw-head probe was conducted in the Virginia Tech small, 3ft. diameter, open-throat wind tunnel at the tunnel speed of 95 fps. The previous calibration of the same probe (Ref. 18) adapted a procedure suggested by Treaster and Yocum (Ref. 16), which requires a different probe setting for each desired pair of flow pitch (ϑ) and yaw (ψ) angles. This is a time consuming process due to the resulting oddities in probe setting angles. To avoid this, probe angle of attack (δ) and bank angle (ϕ) were used directly regardless of the flow angles, and this proved to be considerably time saving not only for the calibration itself but also for the data reduction which will be discussed later.

The probe was set on a sextant and was banked first on its longitudinal axis and then pitched, to simulate flow pitch and yaw angles. Bank angle ϕ was varied from -90° to 90° at 15° interval and at a fixed ϕ , angle of attack δ was changed by 7° from -42° to 42° . The transformation between flow and probe angles is described by

$$\cos\delta = \cos\vartheta \cos\psi$$

$$\tan\phi = \tan\psi / \sin\vartheta$$

or inversely,

$$\sin\psi = \sin\delta \sin\phi$$

$$\tan\delta = \tan\phi \cos\phi$$

The dimensionless pressure coefficients for data reduction are:

$$C_p \text{ pitch} = (p_4 - p_5)/A$$

$$C_p \text{ yaw} = (p_2 - p_3)/A$$

$$C_p \text{ total} = (p_1 - p_t)/A$$

$$C_p \text{ static} = (p_1 - p_s)/A - 1$$

where $A = p_1 - (p_2 + p_3 + p_4 + p_5)/4$. The total and static pressure, p_t and p_s , are reference values which must be determined from an independent probe. The result for the pitch and yaw coefficients is given in Fig. A-1. It exhibits a remarkably simple pattern which can not be found in the old calibration result based on flow pitch and yaw angles (Fig. A-2). The magnitudes of $(C_p \text{ pitch}^2 + C_p \text{ yaw}^2)^{1/2}$ are slightly larger for negative value of δ , and this was found to come from the misalignment of about 1° between the freestream in the tunnel and the horizontal line used as reference for probe setting. This effect was accounted for in the actual data reduction. Another aspect

of the figure which might break its otherwise complete simplicity is the difference between $\phi = \pm 90^\circ$ lines and C_p pitch = 0 line. This is the result of misalignment between the line connecting No. 2 and 3 holes and the hemisphere on the other end of the probe (cf. Fig. 3), which was placed in horizontal plane to serve as a reference. However, the yaw-head can be set at a roll angle of about 5° to nullify the above mentioned difference. If this adjustment is used as a reference when placing the probe, and if the lines in Fig. A-1 are assumed straight, a surprisingly accurate calibration would be possible with only measurements of a set of ϕ at a given δ and a set of δ for a given ϕ . The corresponding error in angularity is estimated to be less than 1° , except for δ larger than 35° , where the error can be up to 2° . Another advantage comes from simplification of the interpolation procedure in data reduction. Only the value of $(C_p \text{ pitch}^2 + C_p \text{ yaw}^2)^{1/2}$ is needed to determine δ through a one-dimensional interpolation. By the same token, ϕ is interpolated with $C_p \text{ pitch}/C_p \text{ yaw}$ only. Consequently, the need of complex 2-dimensional interpolation is eliminated.

For the present study, the straight line assumption was not used, and a 2-dimensional interpolation scheme was developed utilizing subroutine IBCIEU in International Mathematical and Statistical Libraries (IMSL). Therefore,

the greater part of any errors should be blamed on the experimental procedure itself. The angularity in the flow measurement is expected to be accurate within 1° . Also, the reduced data showed little difference from those reduced with the old calibration result.

Fig. A-3 to A-6 show the results of the calibration check conducted in the Virginia Tech stability tunnel, together with the corresponding calibration result in the small tunnel. The angularity coefficients (Fig. A-3 and A-4) and the total pressure coefficient (Fig. A-5) exhibit an almost perfect match, regardless of test speed and type of tunnel. Also, test speed has little effect on the static pressure coefficient. However, the result from the small tunnel differs appreciably from those of in the stability tunnel (Fig. A-6), and this is believed to be the effect of the open test section in the small tunnel. This discrepancy was accounted for in the data reduction procedure, and the corresponding errors for mean velocities were estimated to be less than 3%.

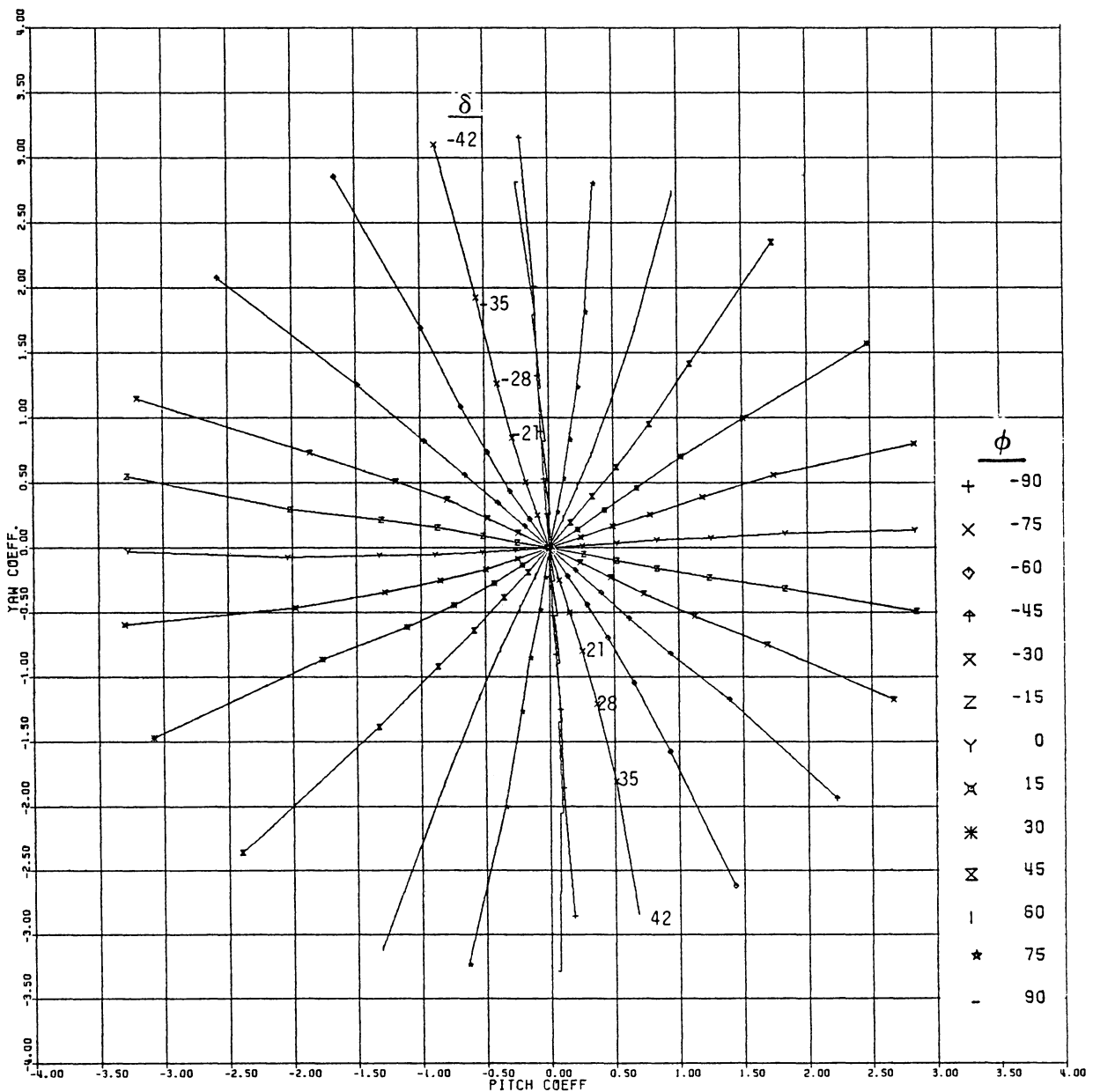


Fig. A-1 Yaw Coefficient vs Pitch Coefficient:
New Calibration Result

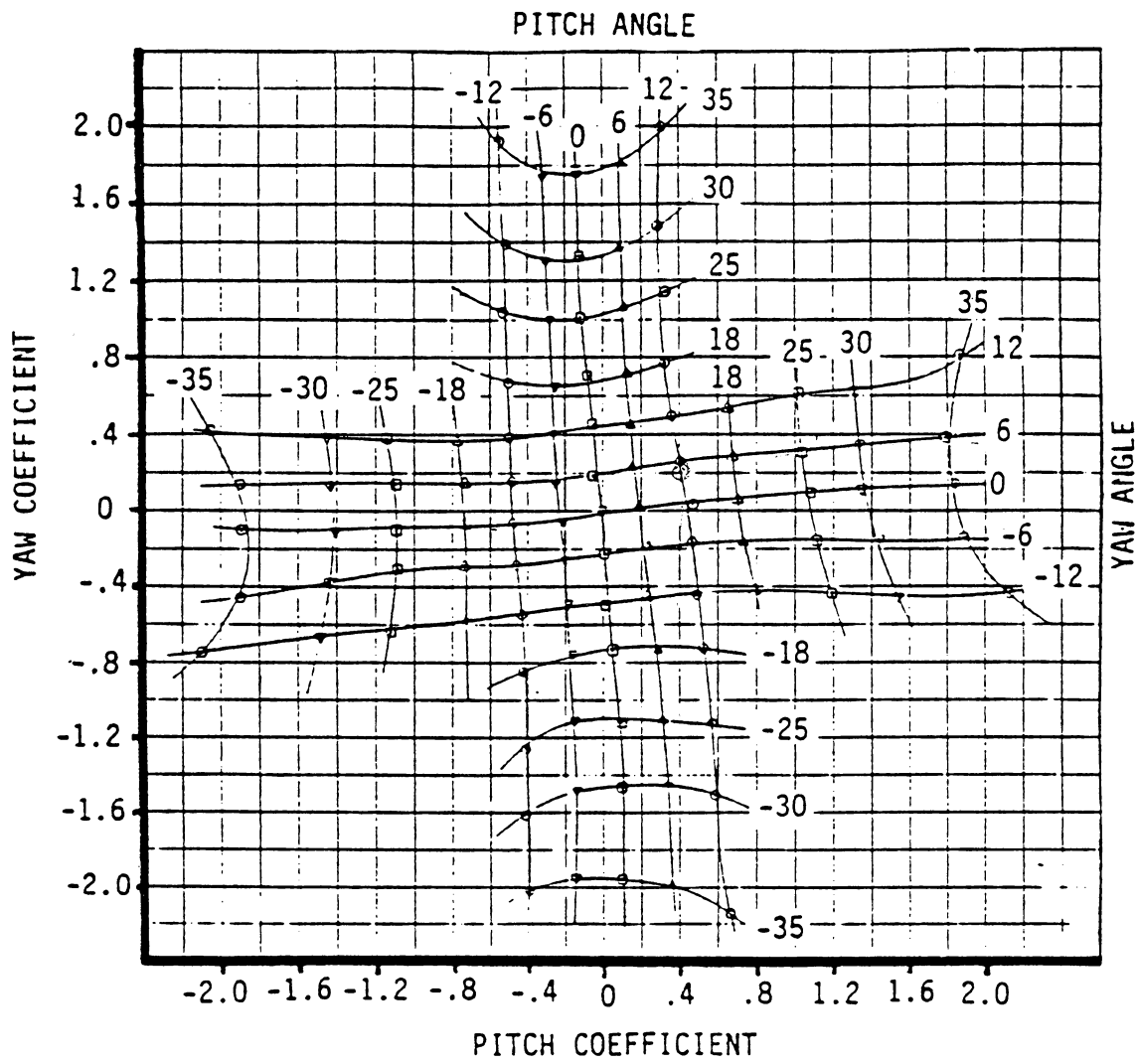


Fig. A-2 Yaw Coefficient vs Pitch Coefficient:
Old Calibration Result (from Ref. 18)

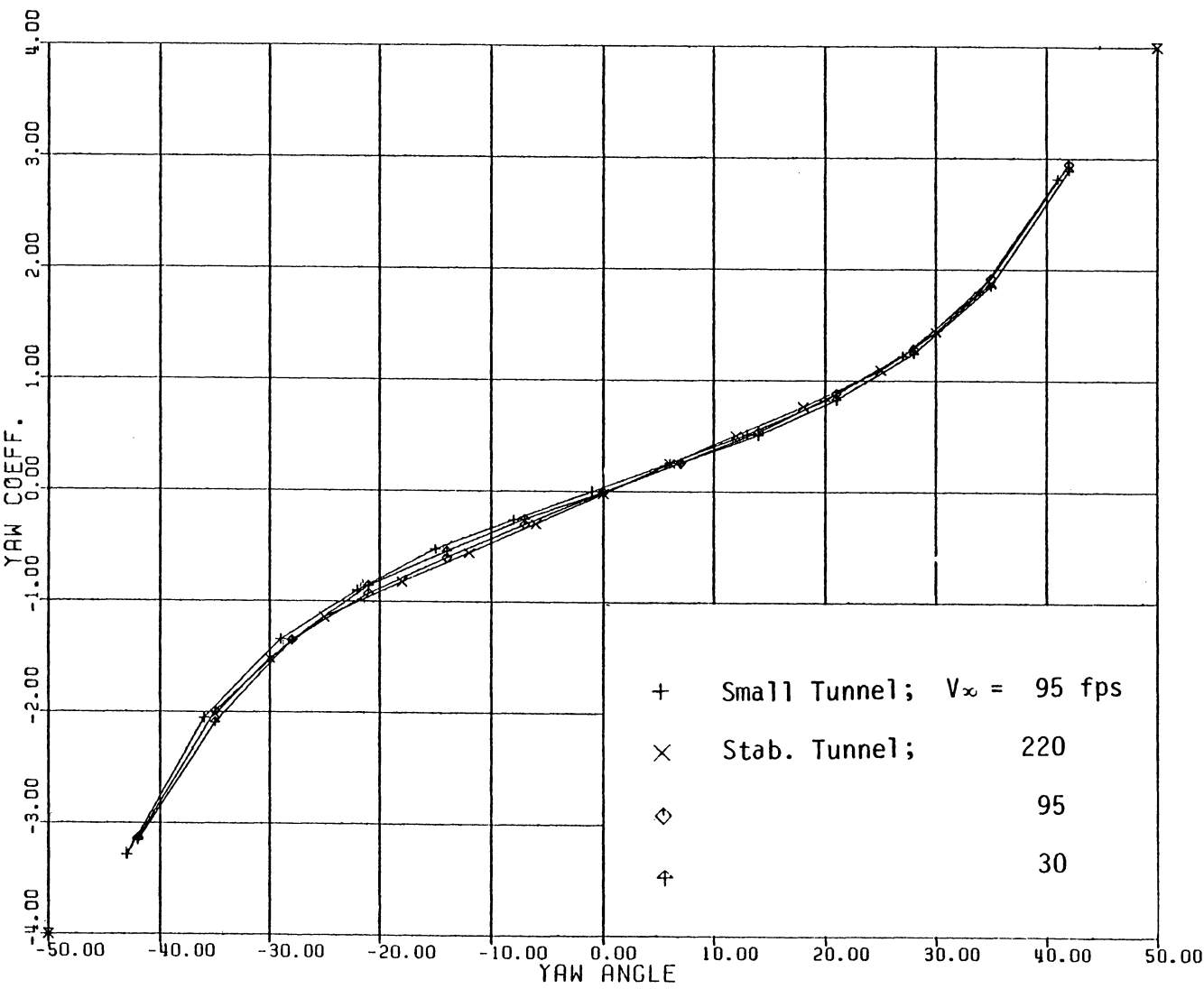


Fig. A-3 Yaw Coefficient vs Yaw Angle for Zero Pitch

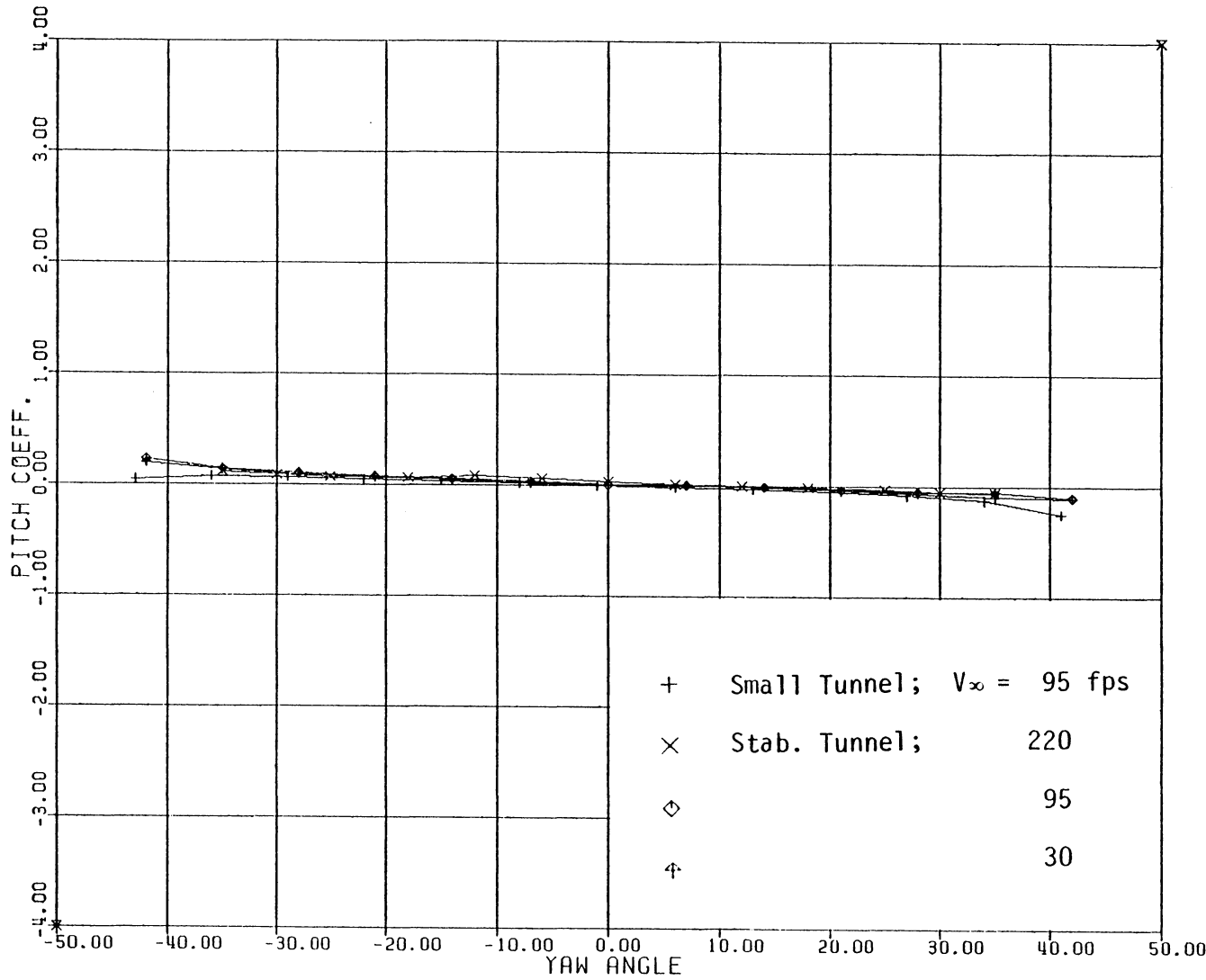


Fig. A-4 Pitch Coefficient vs Yaw Angle for Zero Pitch

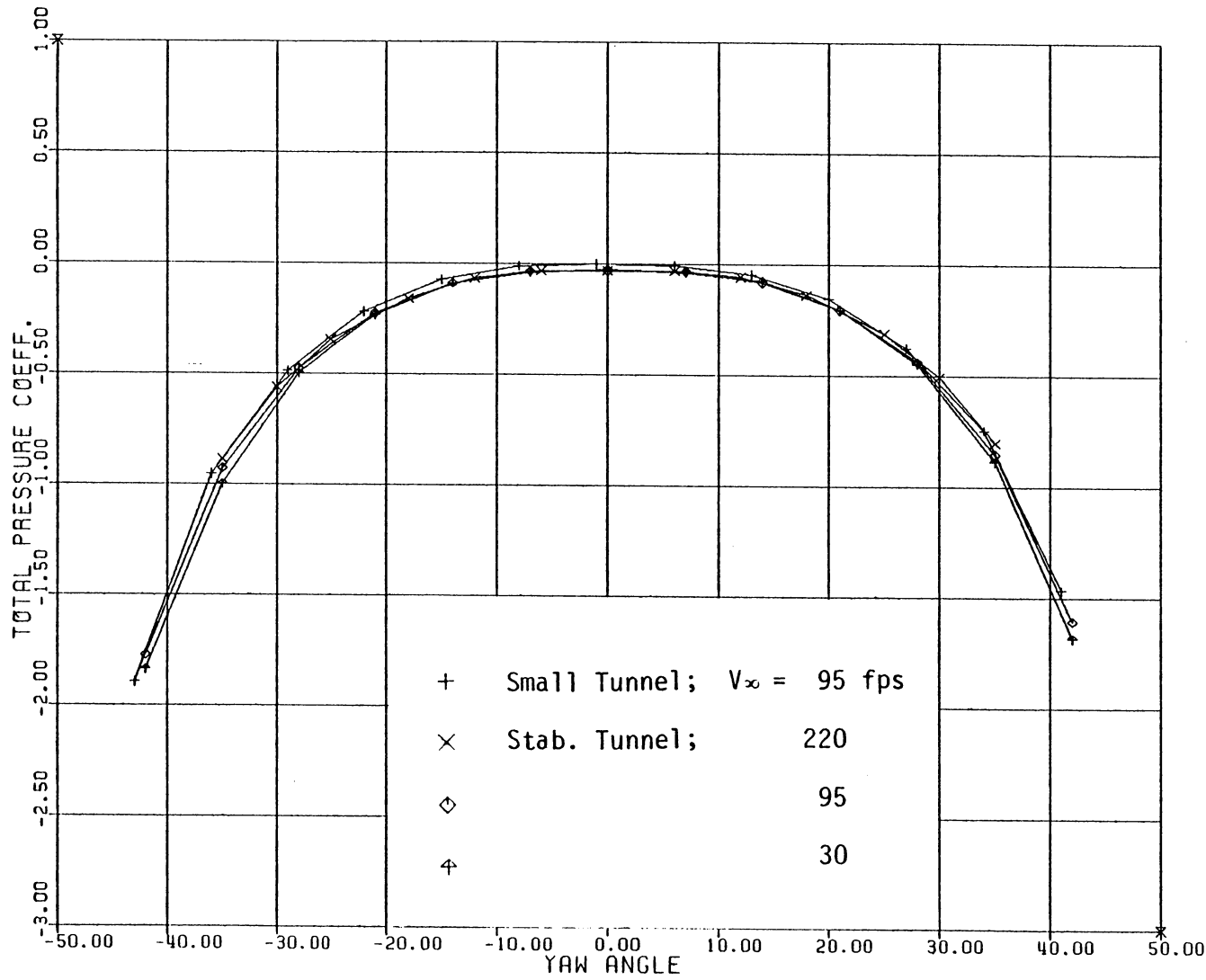


Fig. A-5 Total Pressure Coefficient vs Yaw Angle for Zero Pitch

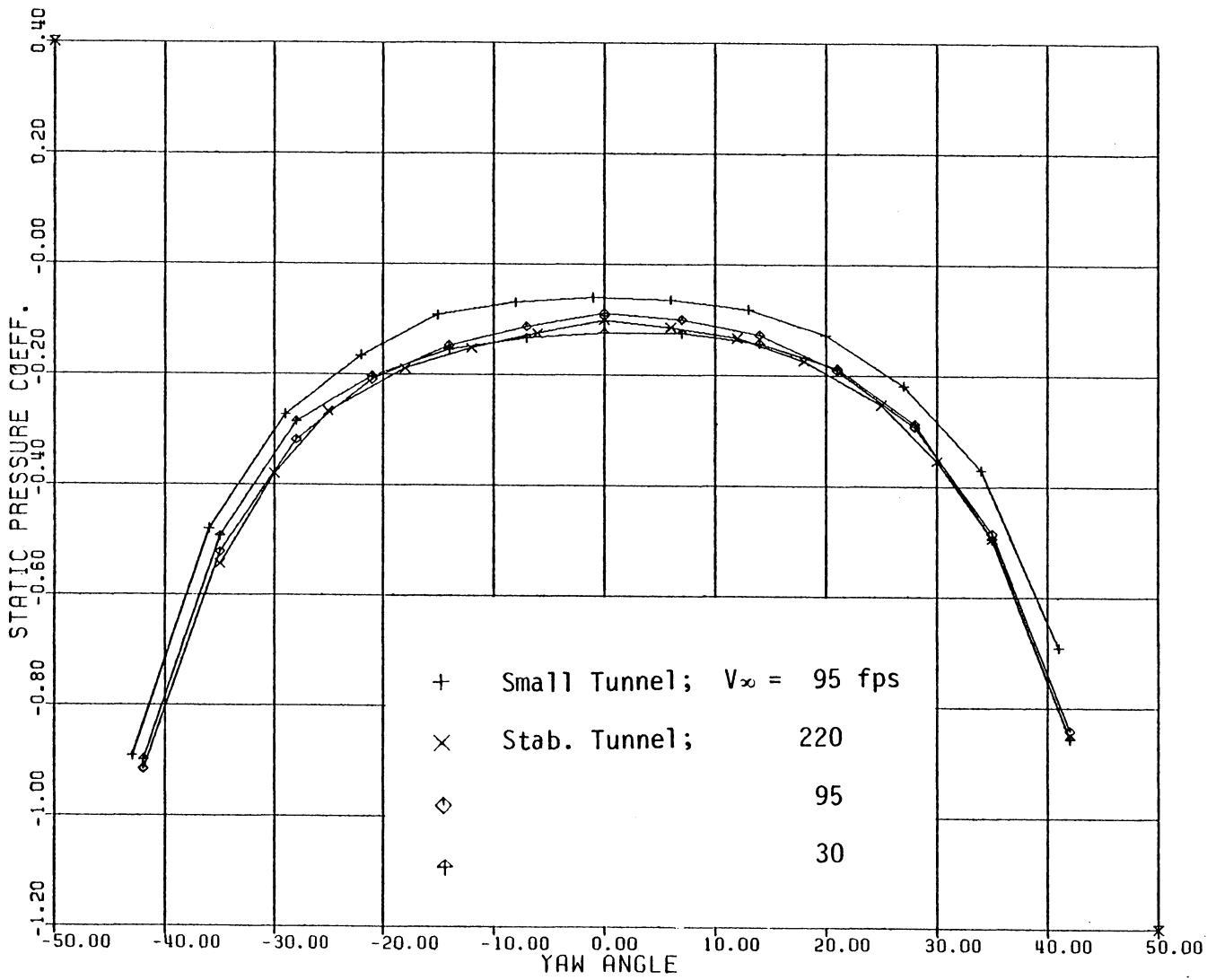


Fig. A-6 Static Pressure Coefficient vs Yaw Angle for Zero Pitch

Appendix B

PROGRAM LISTING FOR YAW-HEAD DATA REDUCTION

```
C  
C  
C          PROGRAM YAW-HEAD  
C          -----  
C  
C          THIS PROGRAM REDUCES YAW-HEAD PROBE DATA  
C  
C          BOTH OLD AND NEW CALIBRATION RESULTS ARE USED  
C          CONFER CHAPTER II AND APPENDIX A FOR DETAIL  
C  
C          INPUT   : POSITION OF YAW-HEAD (IN ANY UNITS)  
C                      FREESTREAM STATIC & DYNAMIC PRESSURE (PSF)  
C                      FREESTREAM TEMPERATURE (FAHRENHEIT)  
C                      5 PRESSURE READINGS FROM YAW-HEAD (PSI)  
C  
C          OUTPUT   : FLOW ANGULARITY (DEGREE)  
C                      VELOCITY COMPONENT (FT/SEC)  
C  
C          SUBROUTINE : IBCIEU IN IMSL  
C  
C  
C          DIMENSION CPSYP1(6,3),CPSYP2(6,7),CPSYP3(6,3)  
C          DIMENSION CPSYN1(6,3),CPSYN2(6,7),CPSYN3(6,3)  
C          DIMENSION CPTYP1(6,3),CPTYP2(6,7),CPTYP3(6,3)  
C          DIMENSION CPTYN1(6,3),CPTYN2(6,7),CPTYN3(6,3)  
C          DIMENSION PA(9,11),PB(11,9),YA(9,11),YB(11,9)  
C          DIMENSION PC(11),PC1(9),PA1(6),PA2(6),PA3(6)  
C          DIMENSION YA1(3),YA2(7),YAN1(3),YAN2(7)  
C          DIMENSION TCPS(1,7),TCPT(1,7),PAFL(1,11),YAFL(1,9)  
C          DIMENSION CPWK1(15),CPWK2(25),PAWK1(41),PAWK2(33)  
C          DIMENSION XCPP(14,13),XCPY(14,13),XCPT(13,13),XCPS(13,13)  
C          DIMENSION DELTA(13),PHI(14),XPHI(13),XFL(1,13),XWK(49)  
C          DIMENSION FP1(2,7),FP2(2,7),FP4(13,7),FP5(13,7),XH1(2),XH2(13)  
C          DIMENSION FY1(2,7),FY2(2,7),FY4(13,7),FY5(13,7),YHN(7),YHP(7)  
C          DIMENSION FL(1,7),WK1(25),WK2(36)  
C  
C          READ IN OLD CALIBRATION DATA  
C  
C          READ (4,10) ((CPSYP1(I,J),J=1,3),I=1,6)  
C          READ (4,11) ((CPSYP2(I,J),J=1,7),I=1,6)  
C          READ (4,10) ((CPSYP3(I,J),J=1,3),I=1,6)  
C          READ (4,10) ((CPSYN1(I,J),J=1,3),I=1,6)  
C          READ (4,11) ((CPSYN2(I,J),J=1,7),I=1,6)  
C          READ (4,10) ((CPSYN3(I,J),J=1,3),I=1,6)  
C          READ (4,10) ((CPTYP1(I,J),J=1,3),I=1,6)  
C          READ (4,11) ((CPTYP2(I,J),J=1,7),I=1,6)  
C          READ (4,10) ((CPTYP3(I,J),J=1,3),I=1,6)  
C          READ (4,10) ((CPTYN1(I,J),J=1,3),I=1,6)  
C          READ (4,11) ((CPTYN2(I,J),J=1,7),I=1,6)  
C          READ (4,10) ((CPTYN3(I,J),J=1,3),I=1,6)  
C          READ (4,12) ((PA(I,J),J=1,11),I=1,9)  
C          READ (4,12) ((YA(I,J),J=1,11),I=1,9)  
C          READ (4,13) ((PB(I,J),J=1,9),I=1,11)  
C          READ (4,13) ((YB(I,J),J=1,9),I=1,11)  
C          READ (4,12) (PC(I),I=1,11)  
C          READ (4,13) (PC1(I),I=1,9)  
C          READ (4,14) (PA1(I),I=1,6)
```

```

READ (4,14) ( PA2(I), I=1,6)
READ (4,14) ( PA3(I), I=1,6)
READ (4,10) ( YA1(I), I=1,3)
READ (4,11) ( YA2(I), I=1,7)
READ (4,10) ( YAN1(I), I=1,3)
READ (4,11) ( YAN2(I), I=1,7)

C
C          READ IN NEW CALIBRATION DATA
C
C
DO 100 I=1,13
PHI(I)=15.*(FLOAT(I)-7.)
XPHI(I)=PHI(I)
DO 100 J=1,13
READ(4,15) DELTA(J),XCPP(I,J),XCPY(I,J),XCPT(I,J),XCPS(I,J)
100 CONTINUE
DO 101 J=1,13
XCPP(1,J)=-XCPY(1,J)/14.7
XCPP(14,J)=-XCPY(13,J)/14.7
XCPP(13,J)=0.
101 XCPY(14,J)=XCPY(13,J)
PHI(14)=PHI(13)
PHI(13)=86.
DELTA(1)=-43.
DELTA(2)=-36.
DELTA(3)=-28.5
DO 104 J=1,7
JX=J+6
FP1(1,J)=XCPP(13,J)
FP1(2,J)=XCPP(14,J)
FY1(1,J)=XCPY(13,J)
FY1(2,J)=XCPY(14,J)
FP2(1,J)=XCPP(13,JX)
FP2(2,J)=XCPP(14,JX)
FY2(1,J)=XCPY(13,JX)
FY2(2,J)=XCPY(14,JX)
YHN(J)=DELTA(J)
YHP(J)=DELTA(JX)
104 CONTINUE
DO 105 I=1,13
XH2(I)=PHI(I)
DO 105 J=1,7
JX=J+6
FP4(1,J)=XCPP(I,J)
FY4(1,J)=XCPY(I,J)
FP5(1,J)=XCPP(I,JX)
FY5(1,J)=XCPY(I,JX)
105 CONTINUE
XH1(1)=86.
XH1(2)=90.
WRITE(6,19)

C
C          READ IN YAW-HEAD DATA
C
C
1002 READ(5,20) NRUN,Q
IF (NRUN .EQ.0) GO TO 1000
WRITE(6,21) NRUN,Q
WRITE(6,22)
1001 READ(5,23) NPOINT,T,P,X,Y,Z,P1,P2,P3,P4,P5
ICAL=2
IF (NPOINT.EQ.0.) GO TO 1002
A=P1-(P2+P3+P4+P5)/4.
CPY=(P2-P3)/A
CPP=(P4-P5)/A

```

```

C
C
C           INTERPOLATION WITH OLD CALIBRATION DATA
C
C
200 IF (ABS(CPP)-.8) 200,200,201
200 IF (ABS(CPY)-2.0) 204,204,499
201 IF (ABS(CPP)-2.0) 202,202,499
202 IF (ABS(CPY)-.8) 203,203,499
203 CALL IBCIEU (PA,9,PC1,9,PC,11,CPY,1,CPP,1,PAFL,1,PAWK1,IER)
      IF (IER-129) 211,499,499
204 CALL IBCIEU (PB,11,PC,11,PC1,9,CPY,1,CPP,1,YAFL,1,PAWK2,IER)
      IF (IER-129) 213,499,499
211 TPA=PAFL(1,1)
      CALL IBCIEU (YA,9,PC1,9,PC,11,CPY,1,CPP,1,PAFL,1,PAWK1,IER)
      IF (IER-129) 212,499,499
212 TYA=PAFL(1,1)
      GO TO 300
213 TPA=YAFL(1,1)
      CALL IBCIEU (YB,11,PC,11,PC1,9,CPY,1,CPP,1,YAFL,1,PAWK2,IER)
      IF (IER-129) 214,499,499
214 TYA=YAFL(1,1)
300 IF (ABS(TPA)-35.) 310,310,499
310 IF (ABS(TYA)-35.) 311,311,499
311 IF (TYA-0.) 320,321,321
320 IF (ABS(TPA)-12.5) 330,330,331
321 IF (ABS(TPA)-12.5) 430,430,431
330 CALL IBCIEU (CPSYN2,6,PA2,6,YAN2,7,TPA,1,TYA,1,TCPS,1,CPWK2,IER)
      IF (IER-129) 340,499,499
331 IF (ABS(TYA)-15.) 336,336,499
332 CALL IBCIEU (CPSYN1,6,PA1,6,YAN1,3,TPA,1,TYA,1,TCPS,1,CPWK1,IER)
      IF (IER-129) 335,499,499
333 CALL IBCIEU (CPSYN3,6,PA3,6,YAN1,3,TPA,1,TYA,1,TCPS,1,CPWK1,IER)
      IF (IER-129) 360,499,499
335 CPS=TCPS(1,1)
      CALL IBCIEU (CPTYN1,6,PA1,6,YAN1,3,TPA,1,TYA,1,TCPT,1,CPWK1,IER)
      IF (IER-129) 341,499,499
336 IF (TPA-0.) 332,332,333
340 CPS=TCPS(1,1)
      CALL IBCIEU (CPTYN2,6,PA2,6,YAN2,7,TPA,1,TYA,1,TCPT,1,CPWK2,IER)
      IF (IER-129) 341,499,499
341 CPT=TCPT(1,1)
      GO TO 500
360 CPS=TCPS(1,1)
      CALL IBCIEU (CPTYN3,6,PA3,6,YAN1,3,TPA,1,TYA,1,TCPT,1,CPWK1,IER)
      IF (IER-129) 341,499,499
430 CALL IBCIEU (CPSYP2,6,PA2,6,YA2,7,TPA,1,TYA,1,TCPS,1,CPWK2,IER)
      IF (IER-129) 440,499,499
431 IF (ABS(TYA)-15.) 436,436,499
432 CALL IBCIEU (CPSYP1,6,PA1,6,YA1,3,TPA,1,TYA,1,TCPS,1,CPWK1,IER)
      IF (IER-129) 435,499,499
433 CALL IBCIEU (CPSYP3,6,PA3,6,YA1,3,TPA,1,TYA,1,TCPS,1,CPWK1,IER)
      IF (IER-129) 460,499,499
435 CPS=TCPS(1,1)
      CALL IBCIEU (CPTYP1,6,PA1,6,YA1,3,TPA,1,TYA,1,TCPT,1,CPWK1,IER)
      IF (IER-129) 441,499,499
436 IF (TPA-0.) 432,432,433
440 CPS=TCPS(1,1)
      CALL IBCIEU (CPTYP2,6,PA2,6,YA2,7,TPA,1,TYA,1,TCPT,1,CPWK2,IER)
      IF (IER-129) 441,499,499
441 CPT=TCPT(1,1)
      GO TO 500
460 CPS=TCPS(1,1)
      CALL IBCIEU (CPTYP3,6,PA3,6,YA1,3,TPA,1,TYA,1,TCPT,1,CPWK1,IER)
      IF (IER-129) 441,499,499
499 WRITE(6,30) NPOINT,X,Y,Z,P1,P2,P3,P4,P5
      ICAL=1

```

```

C
C      INTERPOLATION WITH NEW CALIBRATION DATA
C
C
500 RAD=SQRT(CPP*CPP+CPY*CPY)
  IF (CPP.GT.0.AND.RAD.GE.2.8) GO TO 899
  IF (CPP.LE.0.AND.RAD.GE.3.2) GO TO 899
  IF(CPY.EQ.0.) CPY=.0001
  ANG=CPP/CPY
  NHALF=0
  IF(ANG.LT.0..AND.ANG.GT.-.0681) GO TO 501
  GO TO 504
501 DELTAL=0.
  PHIR=86.
  PHIL=90.
  XL=88.
  IF(CPY) 511,512,512
511 YL=-21.
  DELTAR=-43.
  IQ=1
  831 CALL IBCIEU(FP1,2,XH1,2,YHN,7,XL,1,YL,1,FL,1,WK1,IER)
  IF (IER.GE.129) GO TO 899
  YCPP=FL(1,1)
  CALL IBCIEU(FY1,2,XH1,2,YHN,7,XL,1,YL,1,FL,1,WK1,IER)
  IF (IER.GE.129) GO TO 899
  YCPY=FL(1,1)
  GO TO 821
512 YL=21.
  DELTAR=42.
  IQ=2
  832 CALL IBCIEU(FP2,2,XH1,2,YHP,7,XL,1,YL,1,FL,1,WK1,IER)
  IF (IER.GE.129) GO TO 899
  YCPP=FL(1,1)
  CALL IBCIEU(FY2,2,XH1,2,YHP,7,XL,1,YL,1,FL,1,WK1,IER)
  IF (IER.GE.129) GO TO 899
  YCPY=FL(1,1)
  GO TO 821
504 DELTAL=0.
  PHIR=90.
  PHIL=-90.
  XL=0.
  IF(CPP.EQ.0.) CPP=.0001
  ANG=CPY/CPY
  IF(CPP) 514,514,515
514 YL=-21.
  DELTAR=-43.
  IQ=4
  834 CALL IBCIEU(FP4,13,XH2,13,YHN,7,XL,1,YL,1,FL,1,WK2,IER)
  IF (IER.GE.129) GO TO 899
  YCPP=FL(1,1)
  CALL IBCIEU(FY4,13,XH2,13,YHN,7,XL,1,YL,1,FL,1,WK2,IER)
  IF (IER.GE.129) GO TO 899
  YCPY=FL(1,1)
  GO TO 824
515 YL=21.
  DELTAR=42.
  IQ=5
  835 CALL IBCIEU(FP5,13,XH2,13,YHP,7,XL,1,YL,1,FL,1,WK2,IER)
  IF (IER.GE.129) GO TO 899
  YCPP=FL(1,1)
  CALL IBCIEU(FY5,13,XH2,13,YHP,7,XL,1,YL,1,FL,1,WK2,IER)
  IF (IER.GE.129) GO TO 899
  YCPY=FL(1,1)
  GO TO 824
821 IF(YCPY.EQ.0.) YCPY=.0001
  YANG=YCPP/YCPY

```

```

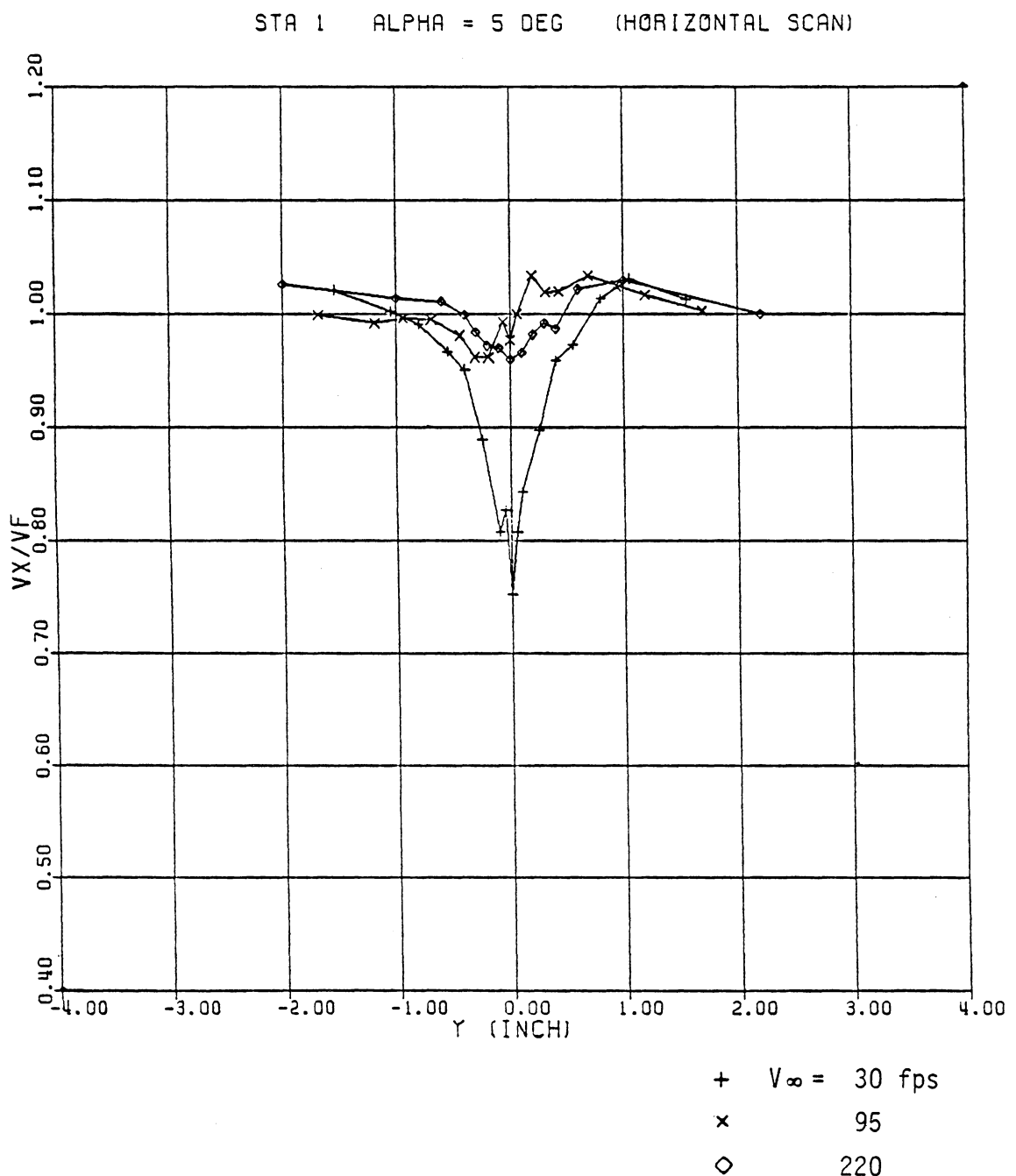
GO TO 803
824 IF(YCPP.EQ.0.) YCPP=.0001
YANG=YCPY/YCPP
GO TO 803
803 TDELTAL=YL
TPHI=XL
NHALF=NHALF+1
DISC=SQRT((CPP-YCPP)**2+(CPY-YCPY)**2)
IF(DISC-.001) 700,700,805
805 IF(NHALF-20) 804,804,700
804 YRAD=SQRT(YCPP*YCPP+YCPY*YCPY)
IF(RAD-YRAD) 811,812,813
811 DELTAR=YL
812 YL=(DELTAL+DELTAR)/2.
GO TO 850
813 DELTAL=YL
GO TO 812
850 IF(ANG-YANG) 851,852,853
851 PHIR=XL
852 XL=(PHIL+PHIR)/2.
IF(IQ.EQ.1) GO TO 831
IF(IQ.EQ.2) GO TO 832
IF(IQ.EQ.4) GO TO 834
IF(IQ.EQ.5) GO TO 835
853 PHIL=XL
GO TO 852
700 CALL IBCIEU(XCPT,13,XPHI,13,DELTA,13,TPHI,1,TDELTAL,1,XFL,1,XWK,IER
$)
IF (IER.GE.129) GO TO 899
ZCPT=XFL(1,1)
CALL IBCIEU(XCPS,13,XPHI,13,DELTA,13,TPHI,1,TDELTAL,1,XFL,1,XWK,IER
$)
IF (IER.GE.129) GO TO 899
ZCPS=XFL(1,1)
GO TO 900
899 WRITE(6,40)
GO TO 1001
C
C
C          CALCULATION OF VELOCITY COMPONENTS
C
900 R=1715.
RHO=P/(R*(T+460.))
VF=SQRT(2.*Q/RHO)
IF (ICAL.EQ.1) GO TO 901
PT=(P1-A*CPT)*144.
PS=(P1-A*(1.0+CPS))*144.
THETA=TPA/57.3
PSI=TYA/57.3
V=SQRT(2.*(PT-PS)/RHO)
VX=V*COS(THETA)*COS(PSI)/VF
VY=V*COS(THETA)*SIN(PSI)/VF
VZ=V*SIN(THETA)/VF
WRITE(6,50) NPOINT,X,Y,Z,P1,P2,P3,P4,P5,TPA,TYA,V, VF, VX, VY, VZ
901 PT=(P1-A*ZCPT)*144.
PS=(P1-A*(1.0+ZCPS))*144.
TTP=TPHI/57.3
TTD=TDELTAL/57.3
THETA=ATAN(TAN(TTD)*COS(TTP))
PSI=ARSIN(SIN(TTD)*SIN(TTP))
V=SQRT(2.*(PT-PS)/RHO)
VX=V*COS(THETA)*COS(PSI)/VF
VY=V*COS(THETA)*SIN(PSI)/VF
VZ=V*SIN(THETA)/VF
THETA=THETA*57.3
PSI=PSI*57.3

```

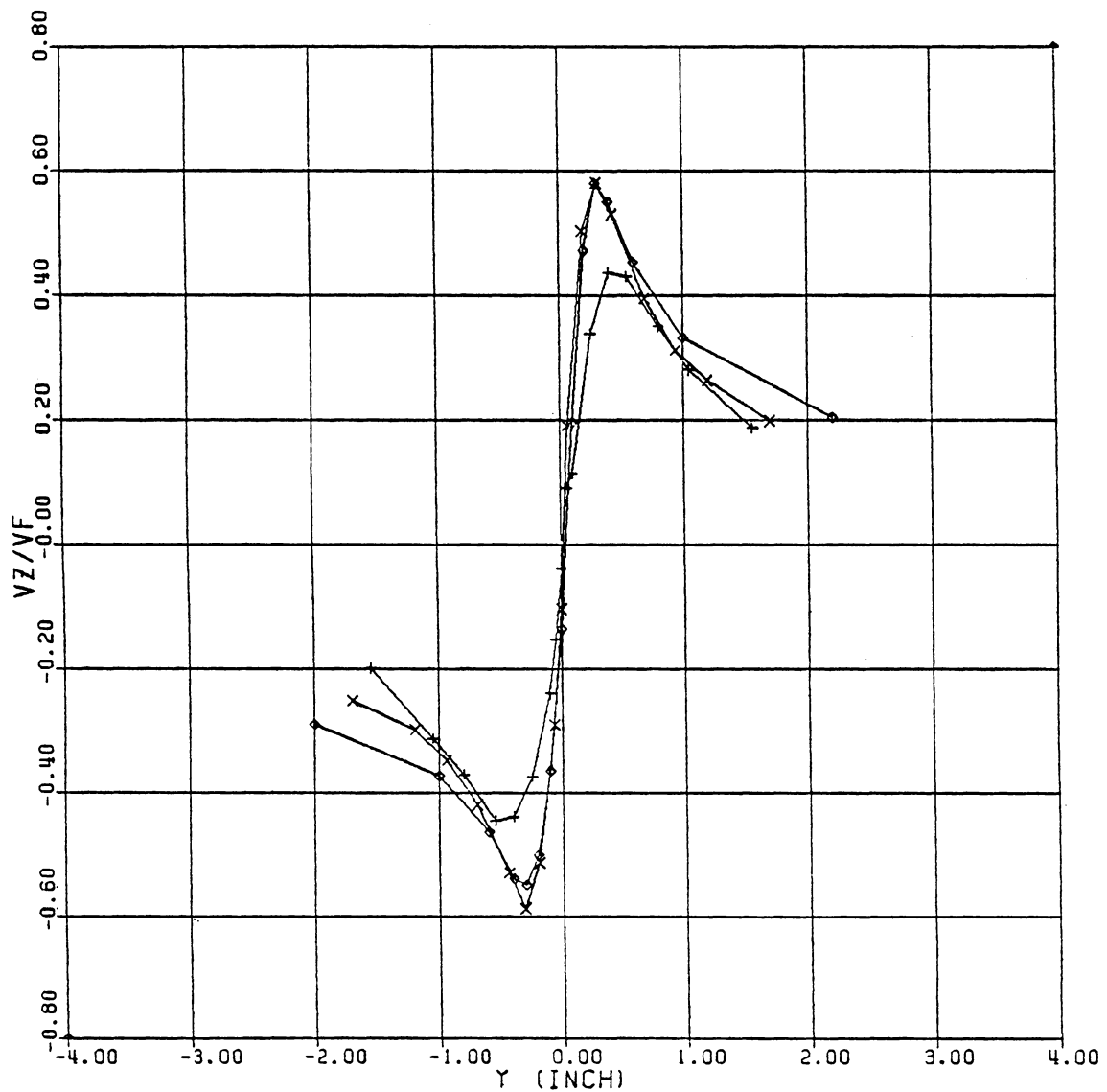
```
      WRITE(6,60) THETA,PSI,V,VF,VX,VY,VZ
      GO TO 1001
C
C
C
10 FORMAT(3F7.3)
11 FORMAT(7F7.3)
12 FORMAT(11F7.3)
13 FORMAT(9F7.3)
14 FORMAT(6F7.3)
15 FORMAT(5F10.3)
19 FORMAT('1',//)
20 FORMAT(12,5X,F4.1)
21 FORMAT('1',//,50X,'RUN',2X,12,7X,'Q = ',F4.1,///)
22 FORMAT(3X,'POINT',105H   X   Y   Z   P1   P2   P3
      $ P4   P5   PITCH   YAW   VEL   VF   VX/VF   VY/VF   VZ/VF,/)
23 FORMAT(12,10F7.0)
30 FORMAT(/,6X,12,3F7.2,5F7.3,10X,'OUT OF OLD CALIBRATION RANGE')
40 FORMAT(74X,'OUT OF NEW CALIBRATION RANGE')
50 FORMAT(/,6X,12,3F7.2,5F7.3,4F7.1,3F7.2)
60 FORMAT(64X,4F7.1,3F7.2,/)

1000 CONTINUE
STOP
END
```

Appendix C
EXPERIMENTAL DATA IN THE NEAR-WAKE

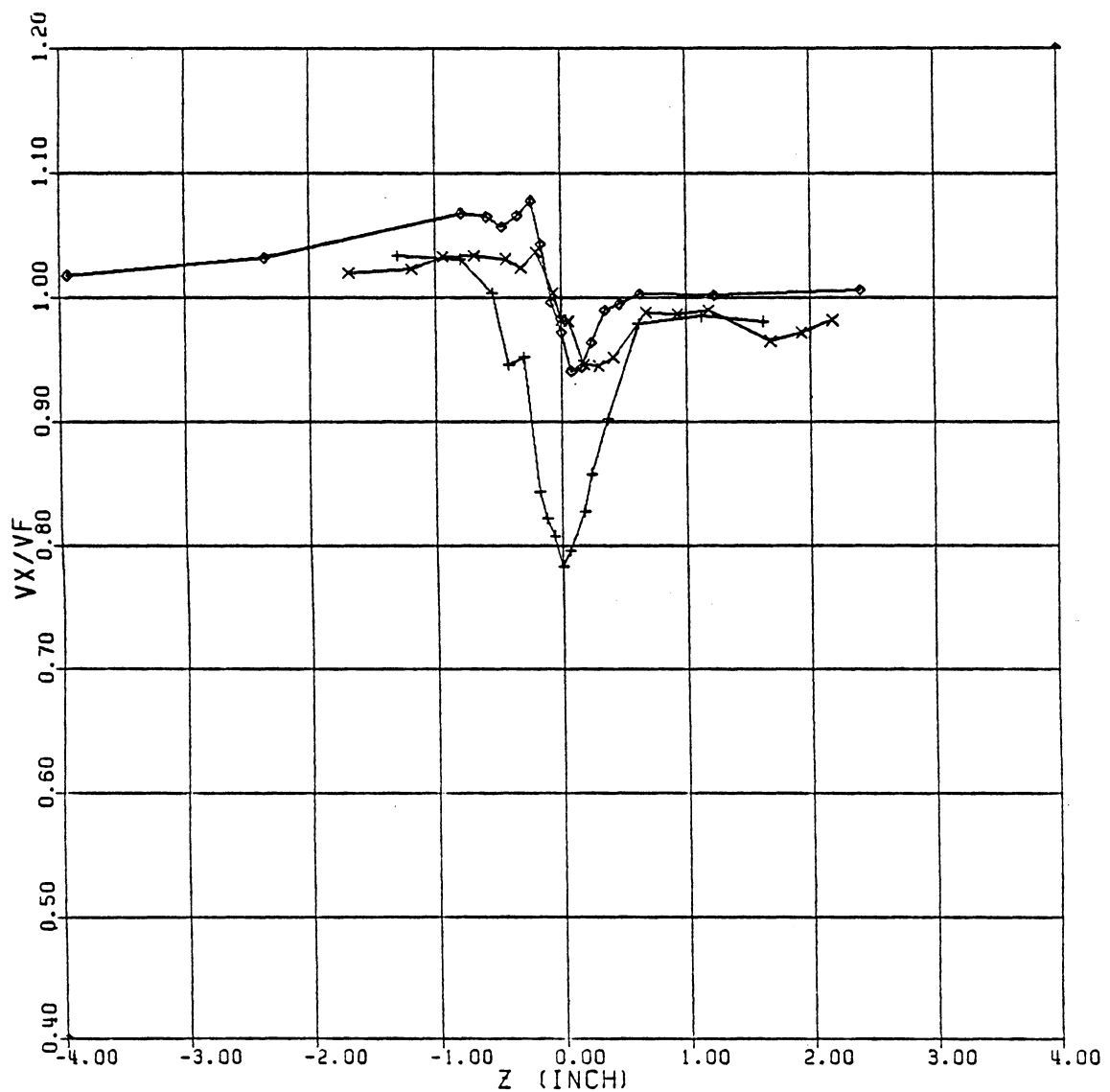


STA 1 ALPHA = 5 DEG (HORIZONTAL SCAN)

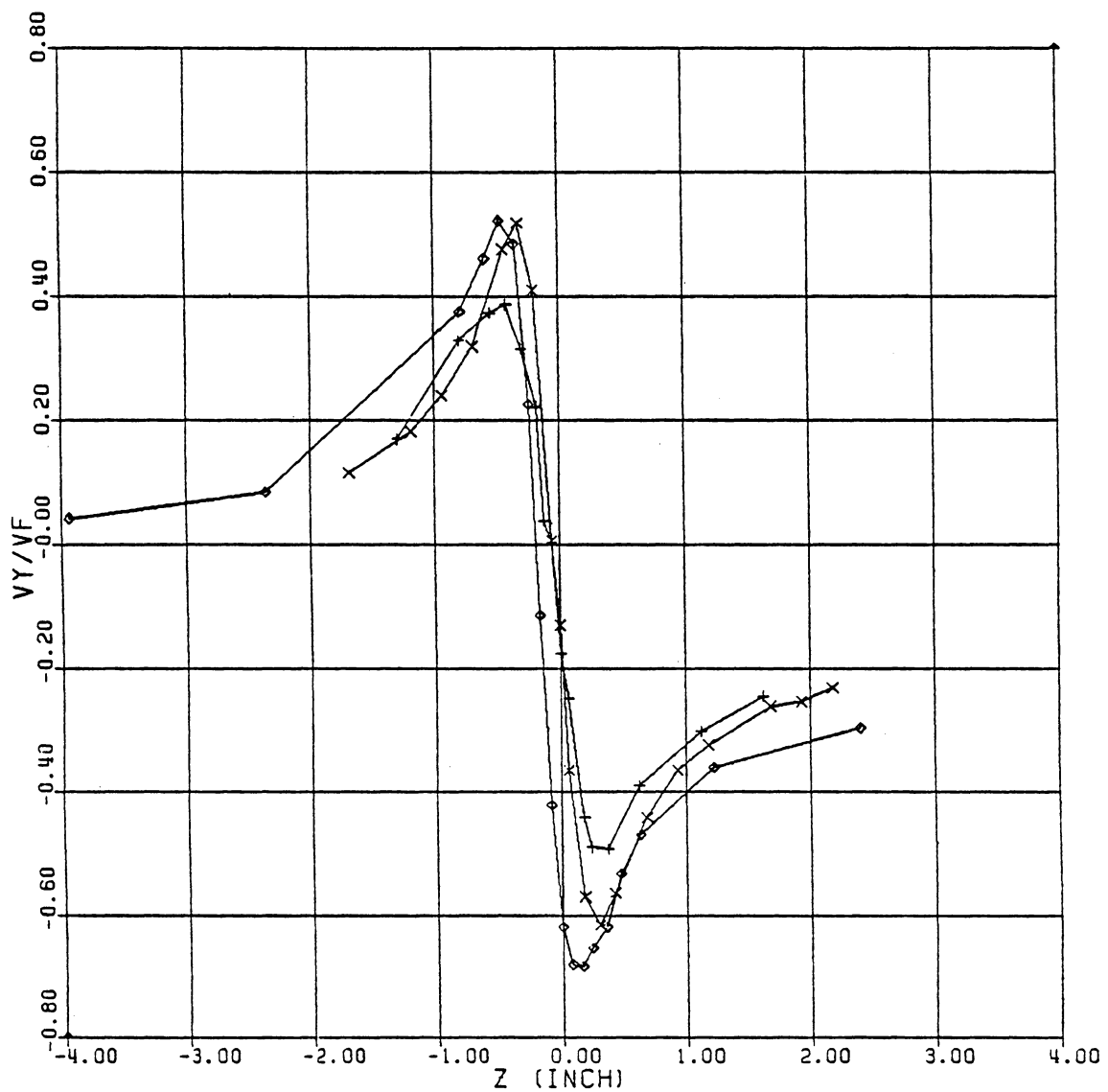


+ $V_\infty = 30 \text{ fps}$
x 95
◊ 220

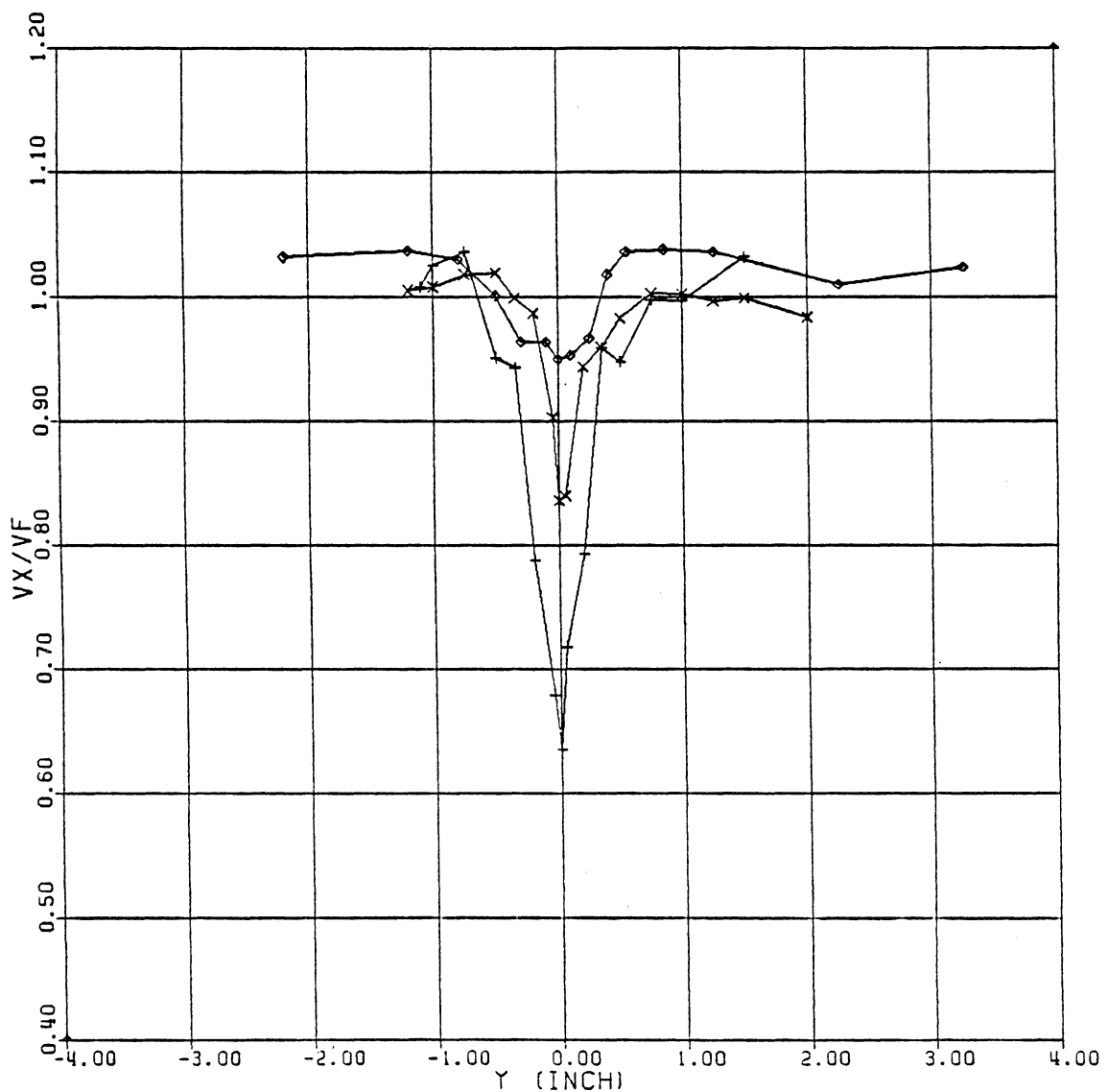
STA 1 ALPHA = 5 DEG (VERTICAL SCAN)

+ $V_\infty = 30 \text{ fps}$ \times 95 \diamond 220

STA 1 ALPHA = 5 DEG (VERTICAL SCAN)

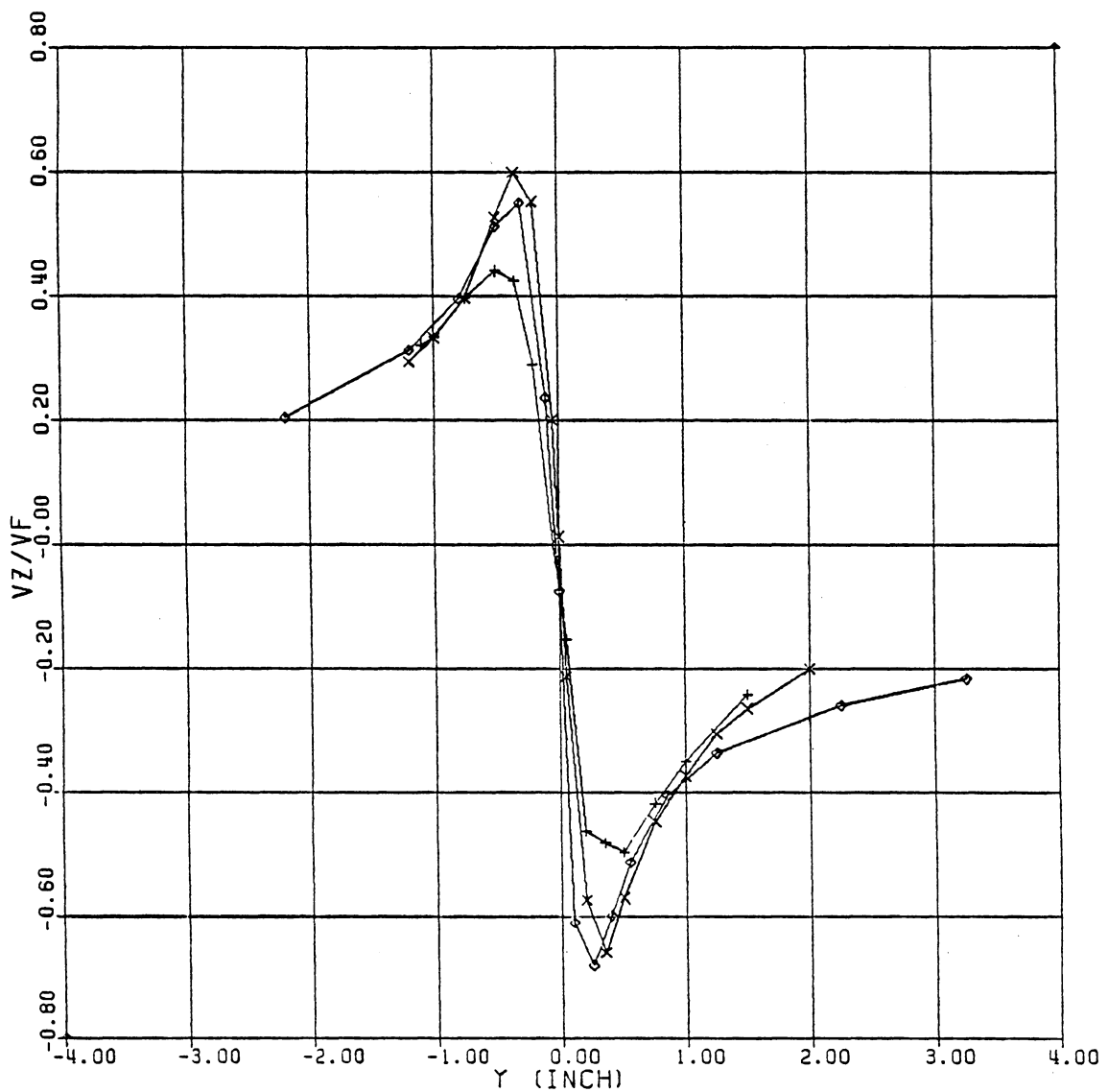
 $+$ $V_\infty = 30$ fps \times 95 \diamond 220

STA 1 ALPHA = -10 DEG (HORIZONTAL SCAN)



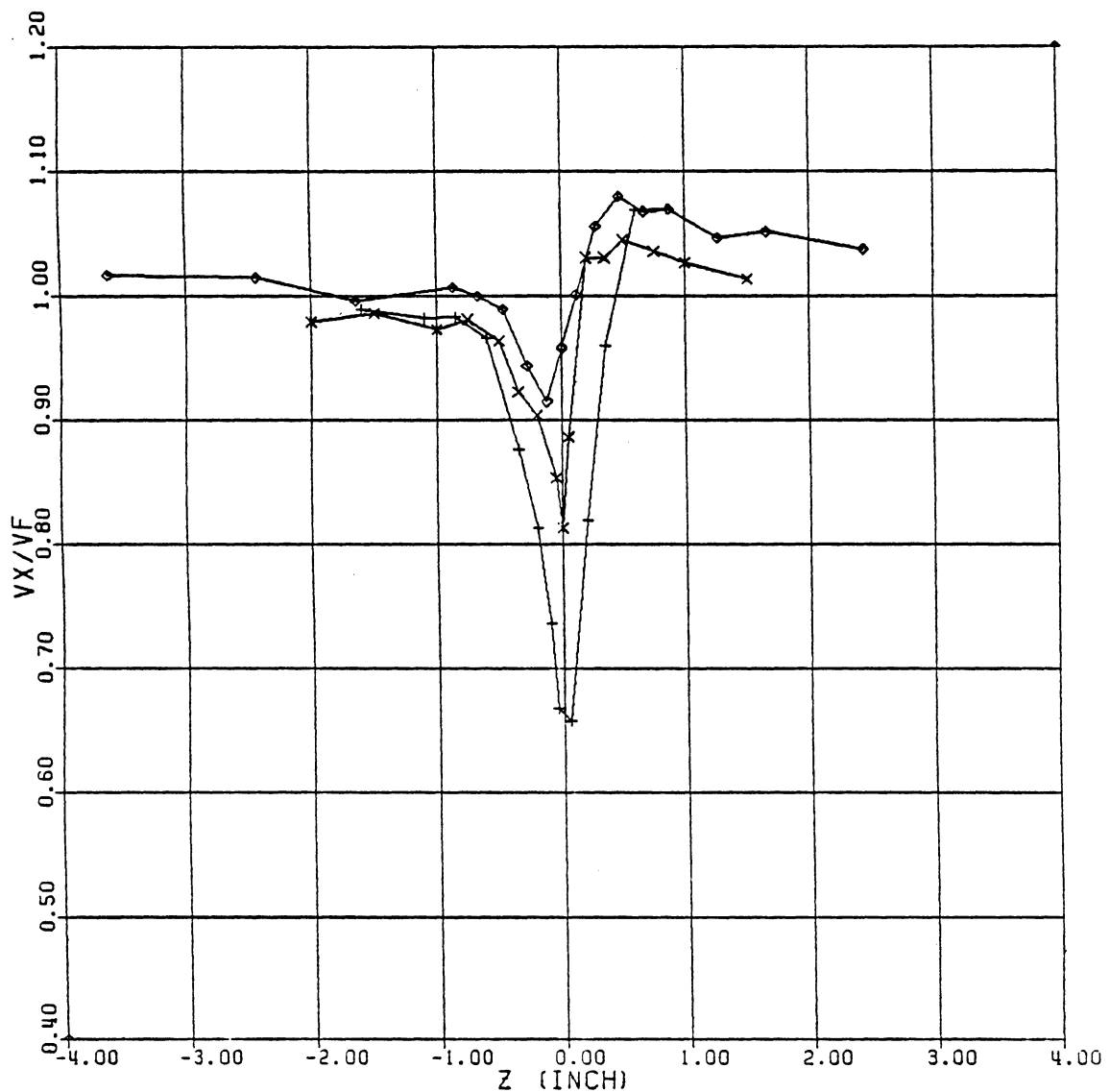
+ $V_\infty = 30 \text{ fps}$
x 95
 \diamond 220

STA 1 ALPHA = -10 DEG (HORIZONTAL SCAN)



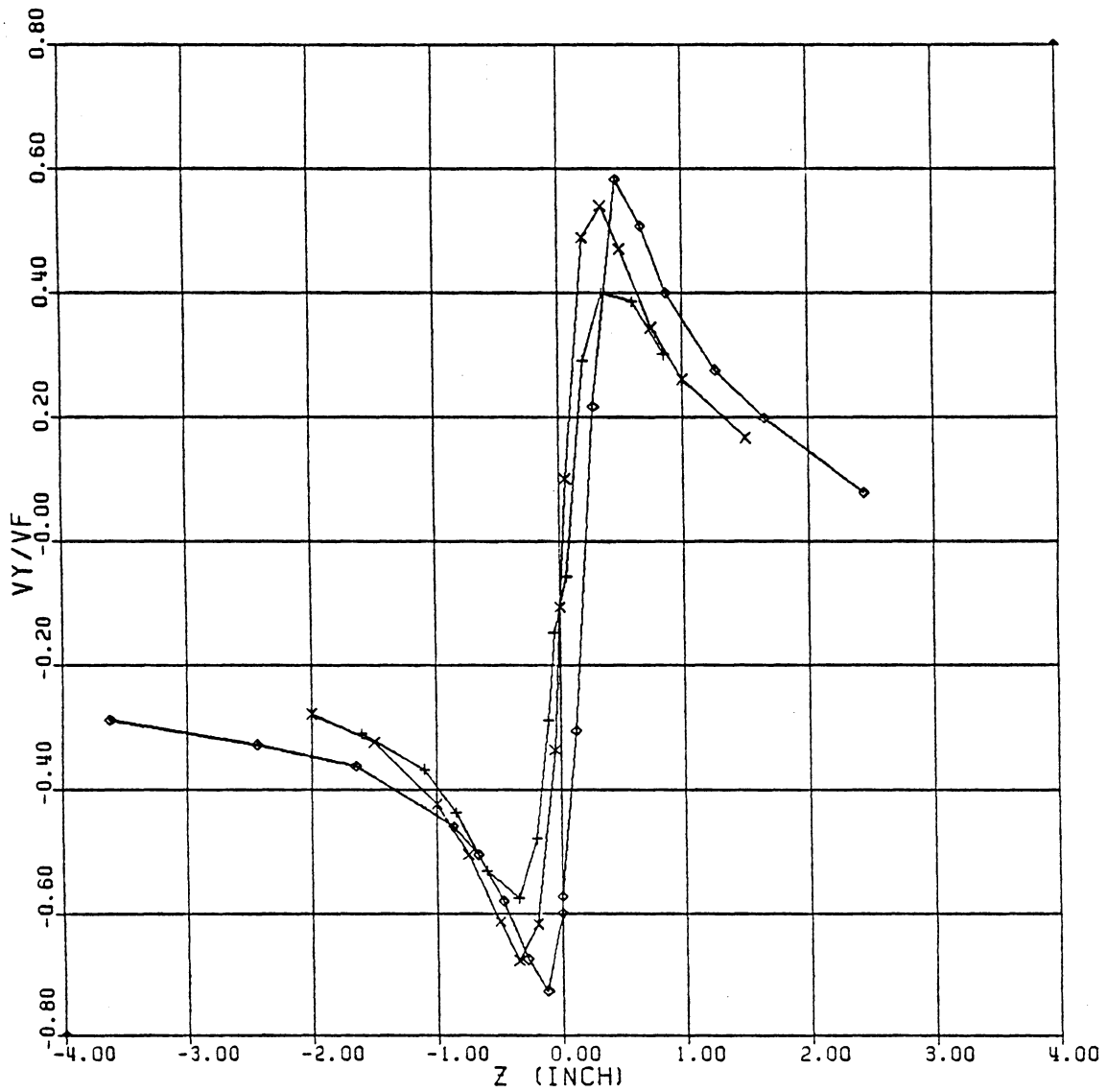
+ $V_\infty = 30 \text{ fps}$
x 95
 $\diamond \quad 220$

STA 1 ALPHA = -10 DEG (VERTICAL SCAN)



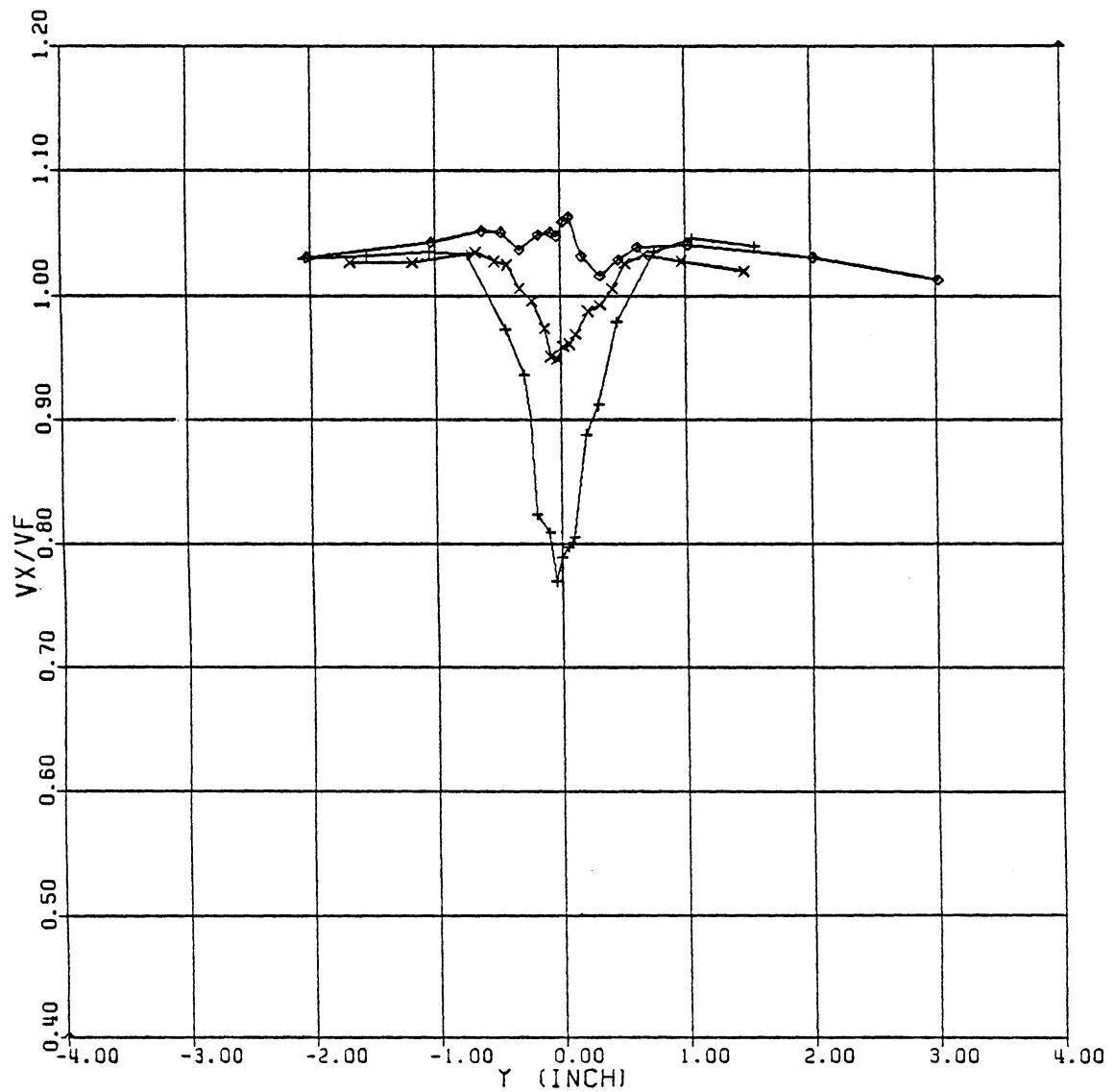
+ $V_\infty = 30 \text{ fps}$
x 95
◊ 220

STA 1 ALPHA = -10 DEG (VERTICAL SCAN)



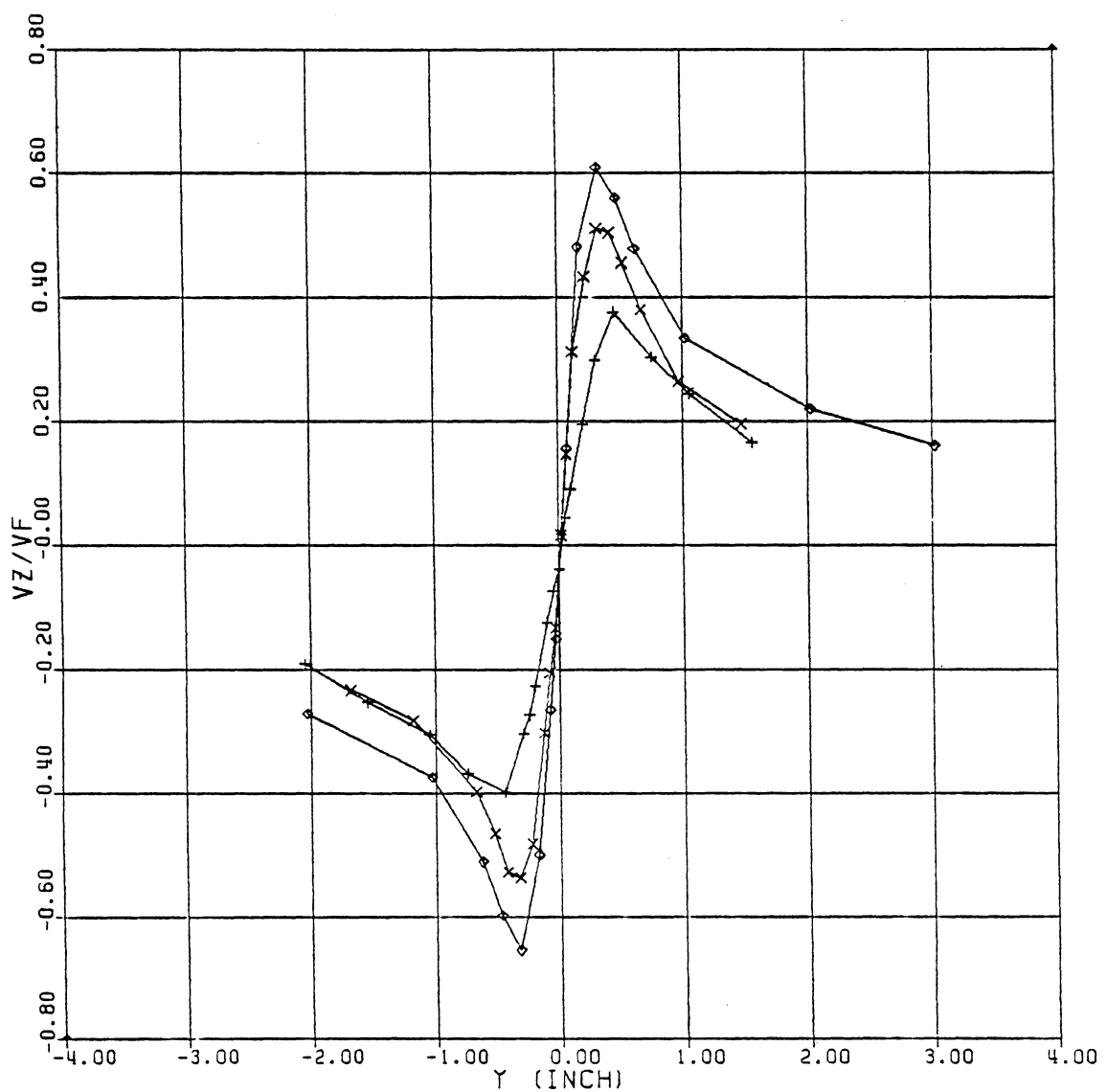
+ $V_\infty = 30$ fps
x 95
◊ 220

STA 2 ALPHA = 5 DEG (HORIZONTAL SCAN)



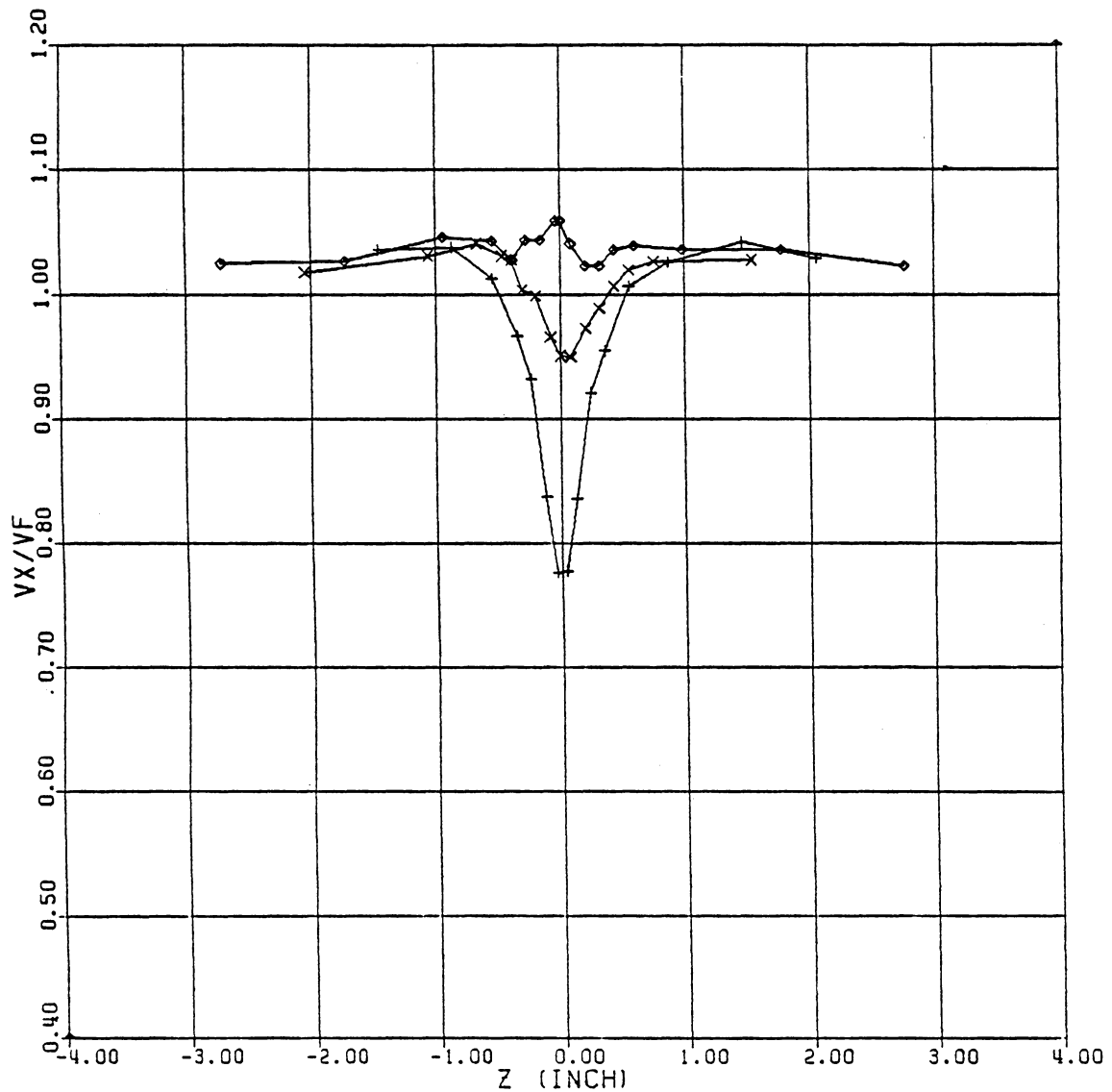
+ $V_\infty = 30 \text{ fps}$
x 95
◊ 220

STA 2 ALPHA = 5 DEG (HORIZONTAL SCAN)



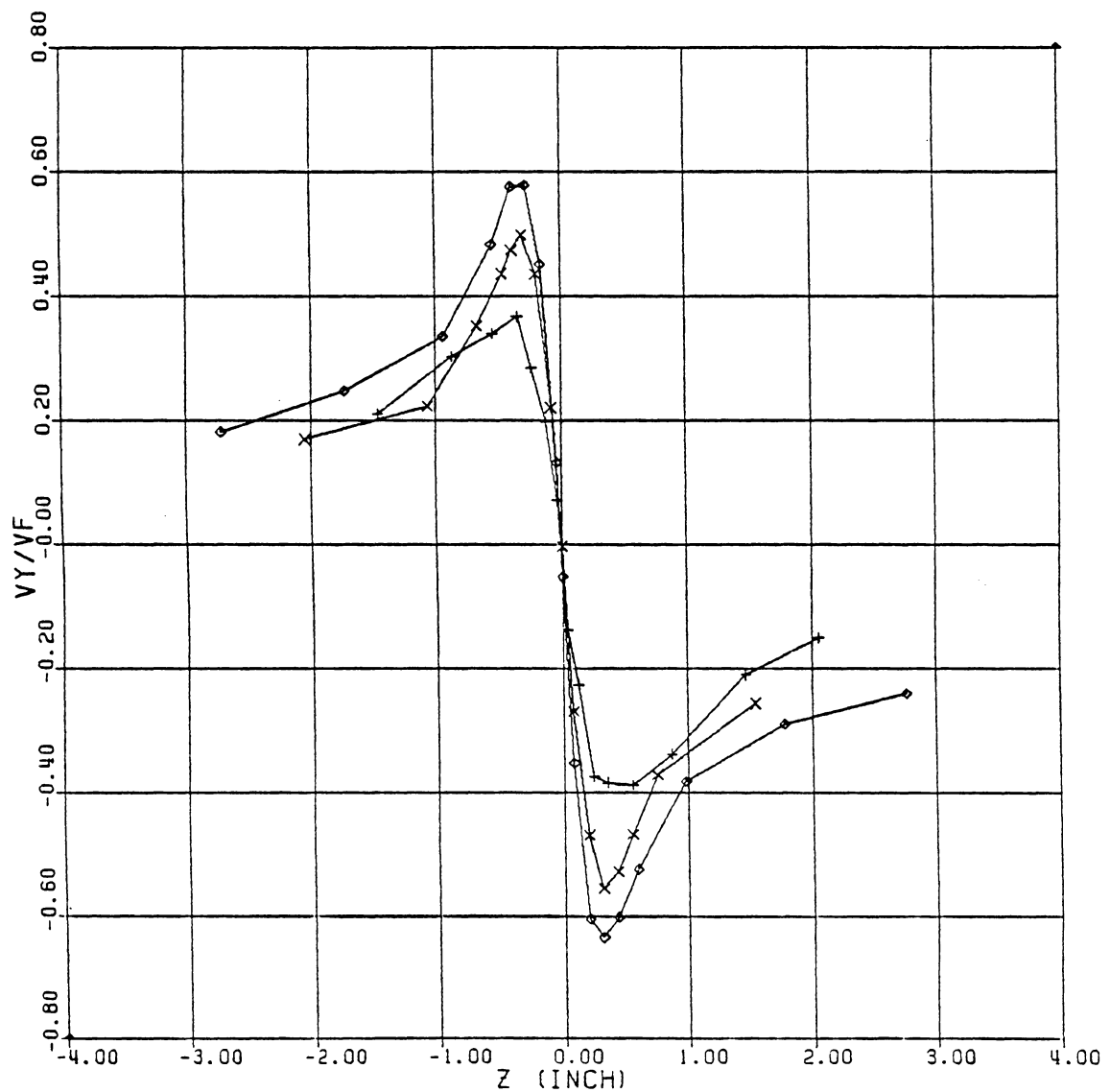
+ $V_\infty = 30 \text{ fps}$
x 95
◊ 220

STA 2 ALPHA = 5 DEG (VERTICAL SCAN)



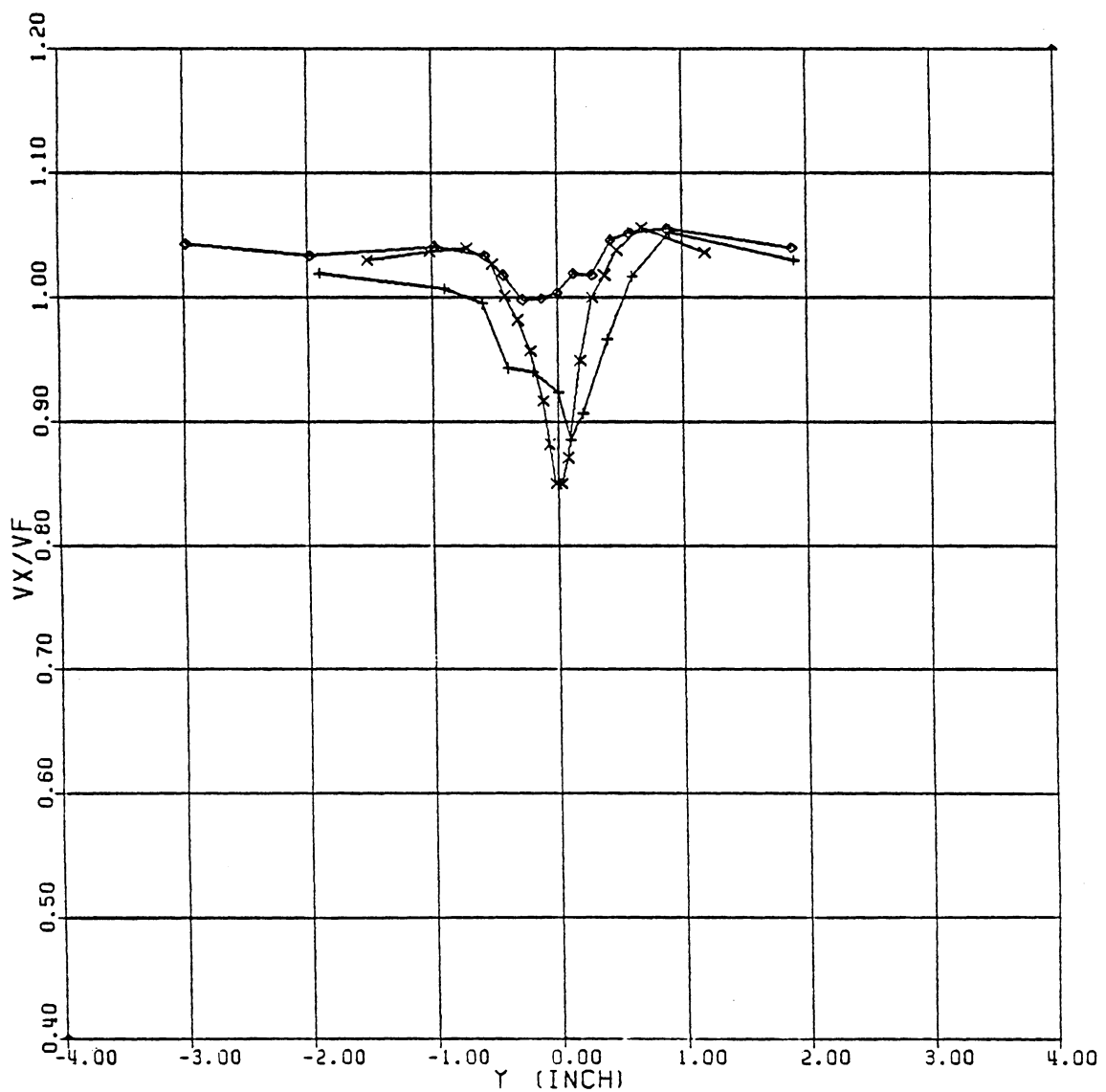
+ $V_\infty = 30$ fps
x 95
◊ 220

STA 2 ALPHA = 5 DEG (VERTICAL SCAN)



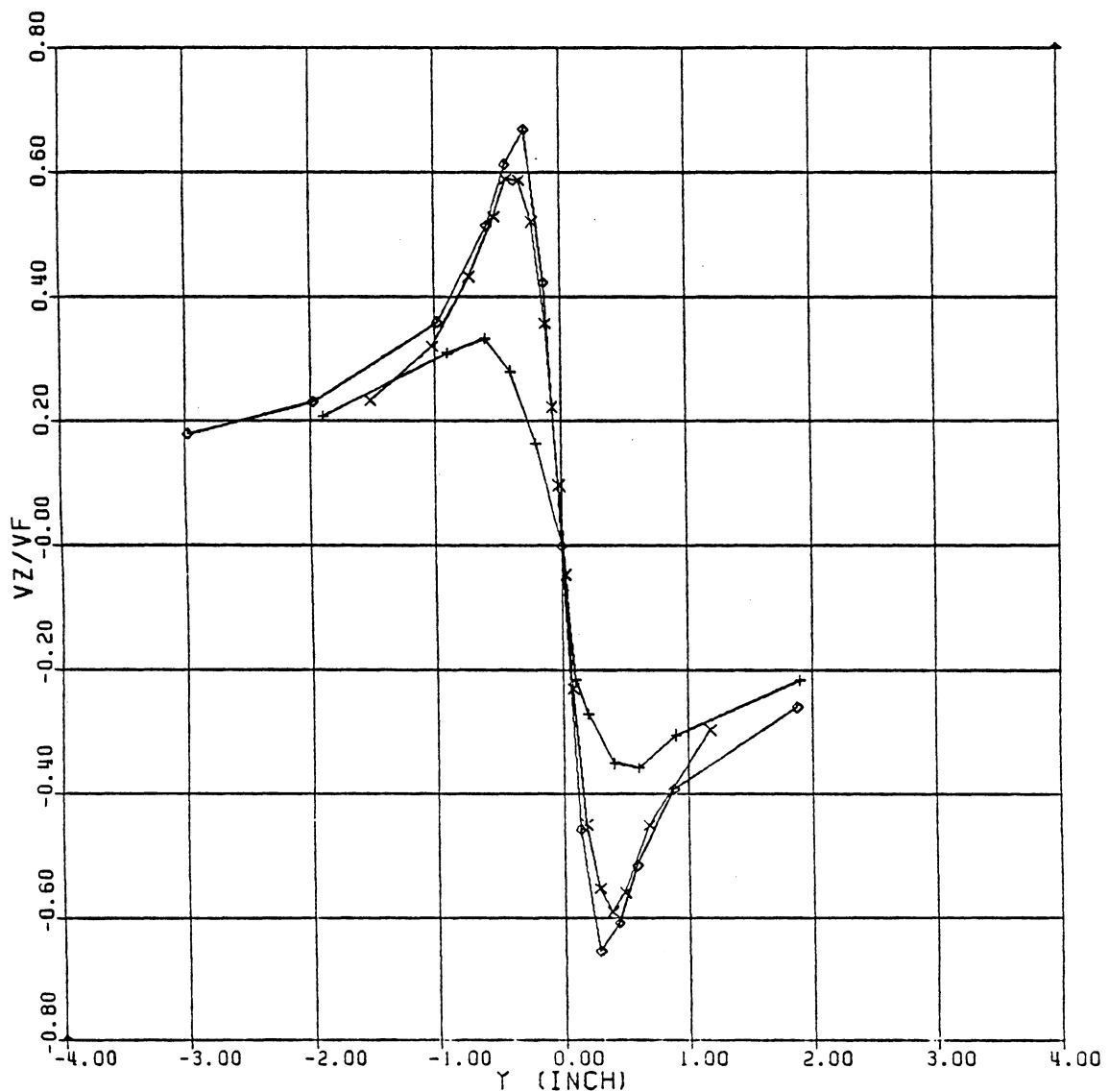
+ $V_\infty = 30 \text{ fps}$
x 95
◊ 220

STA 2 ALPHA = -10 DEG (HORIZONTAL SCAN)



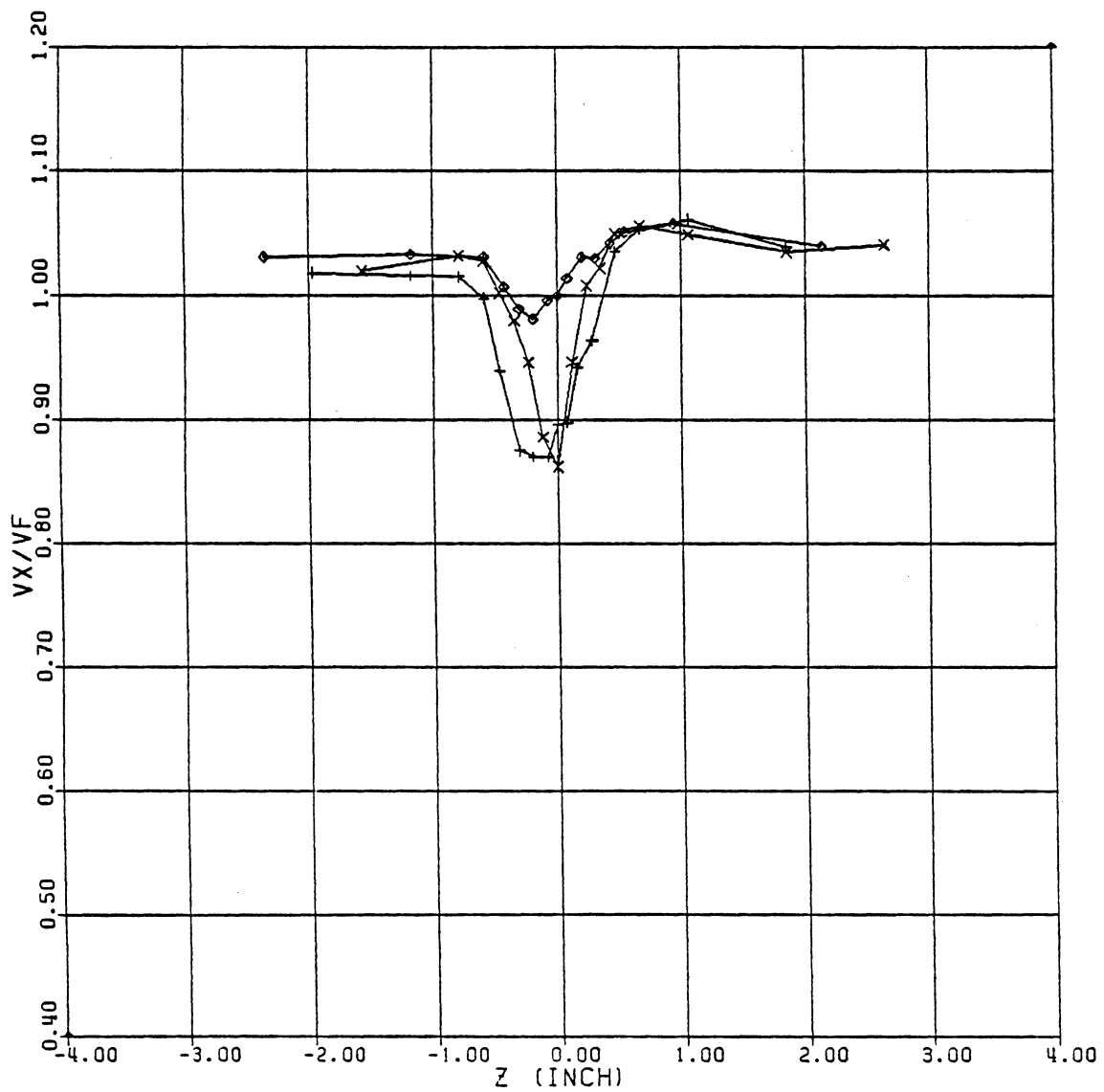
+ $V_\infty = 30$ fps
x 95
 \diamond 220

STA 2 ALPHA = -10 DEG (HORIZONTAL SCAN)



+ $V_\infty = 30$ fps
x 95
 \diamond 220

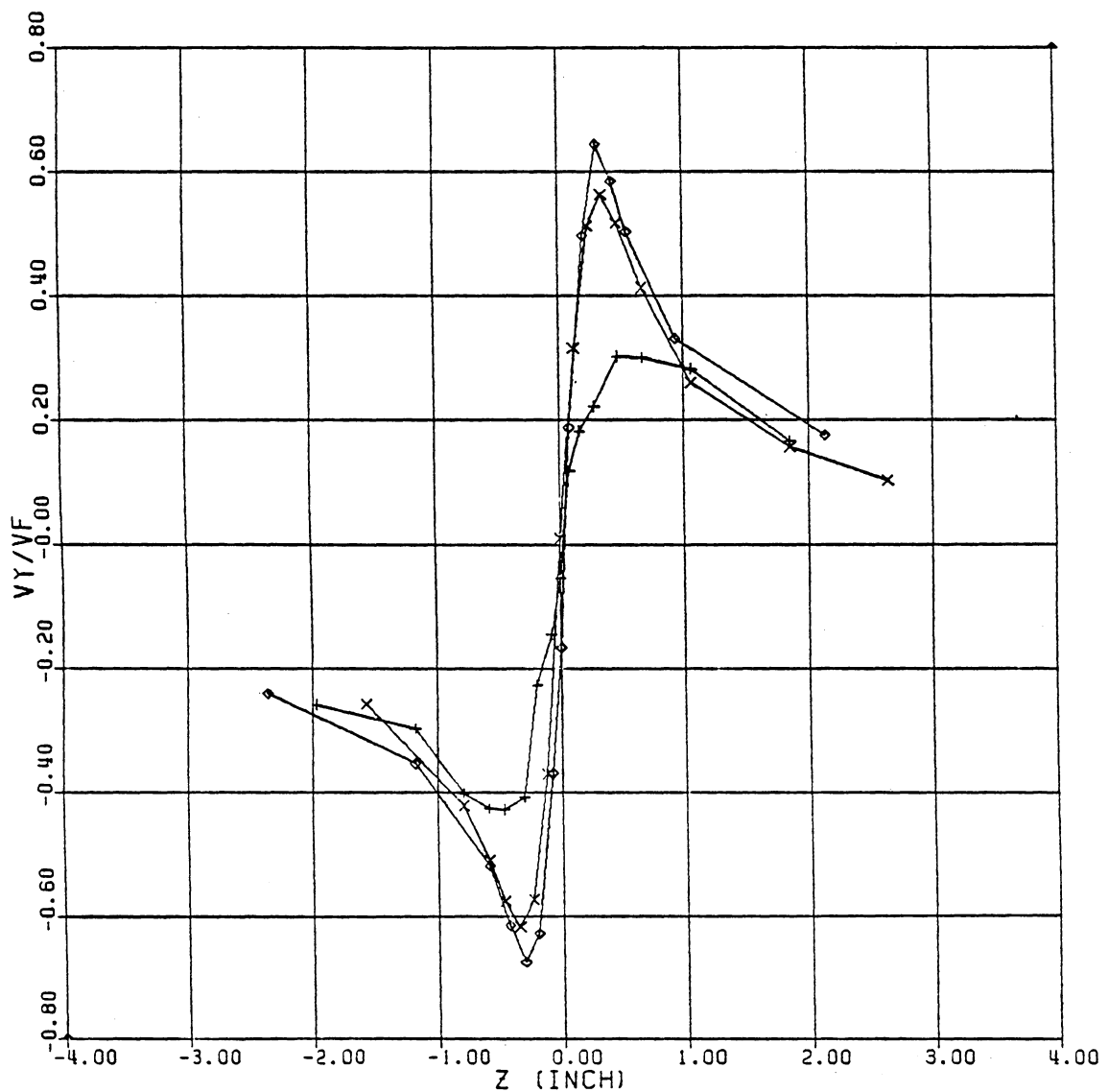
STA 2 ALPHA = -10 DEG (VERTICAL SCAN)

+ $V_\infty = 30$ fps

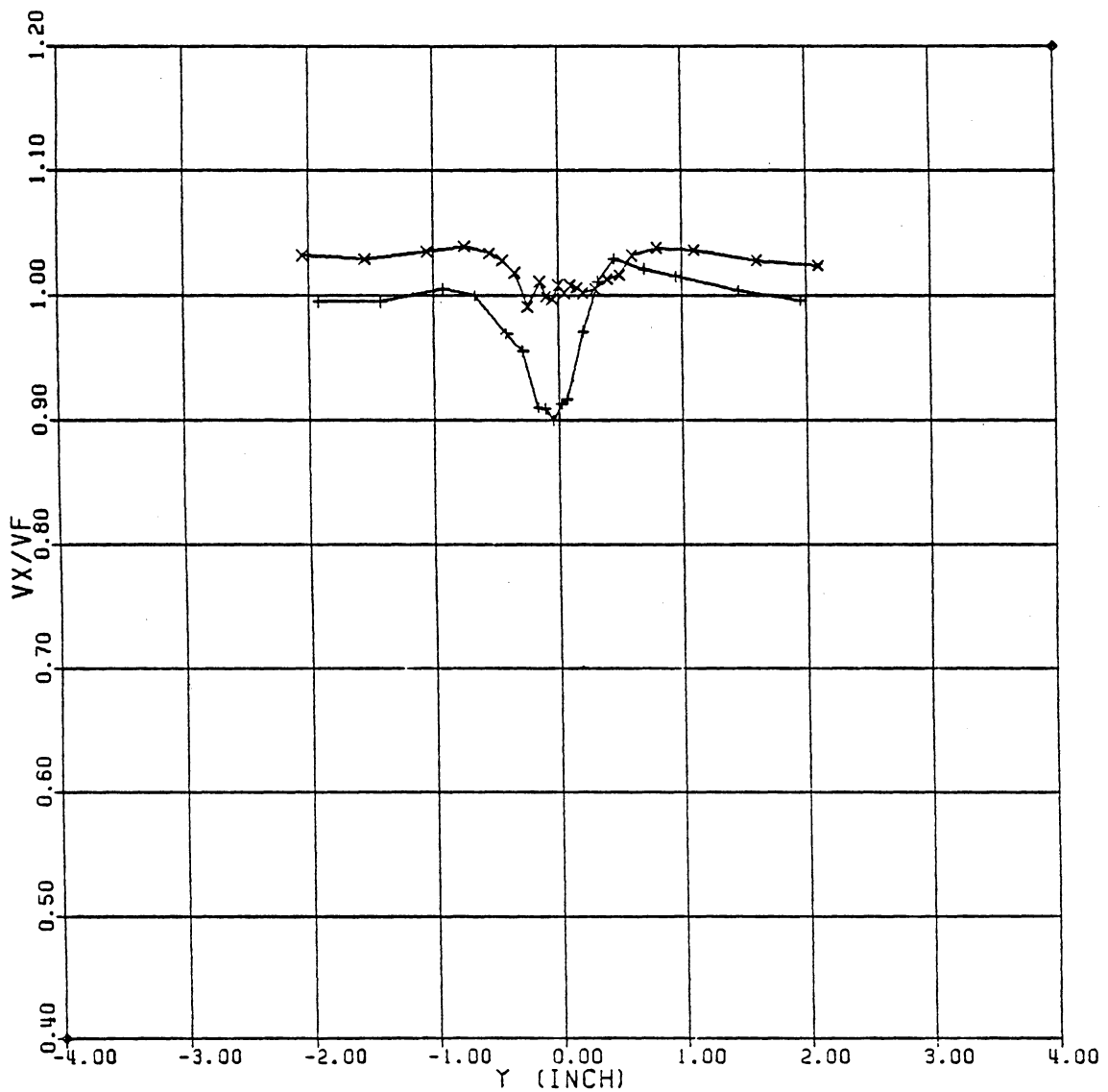
x 95

◊ 220

STA 2 ALPHA = -10 DEG (VERTICAL SCAN)

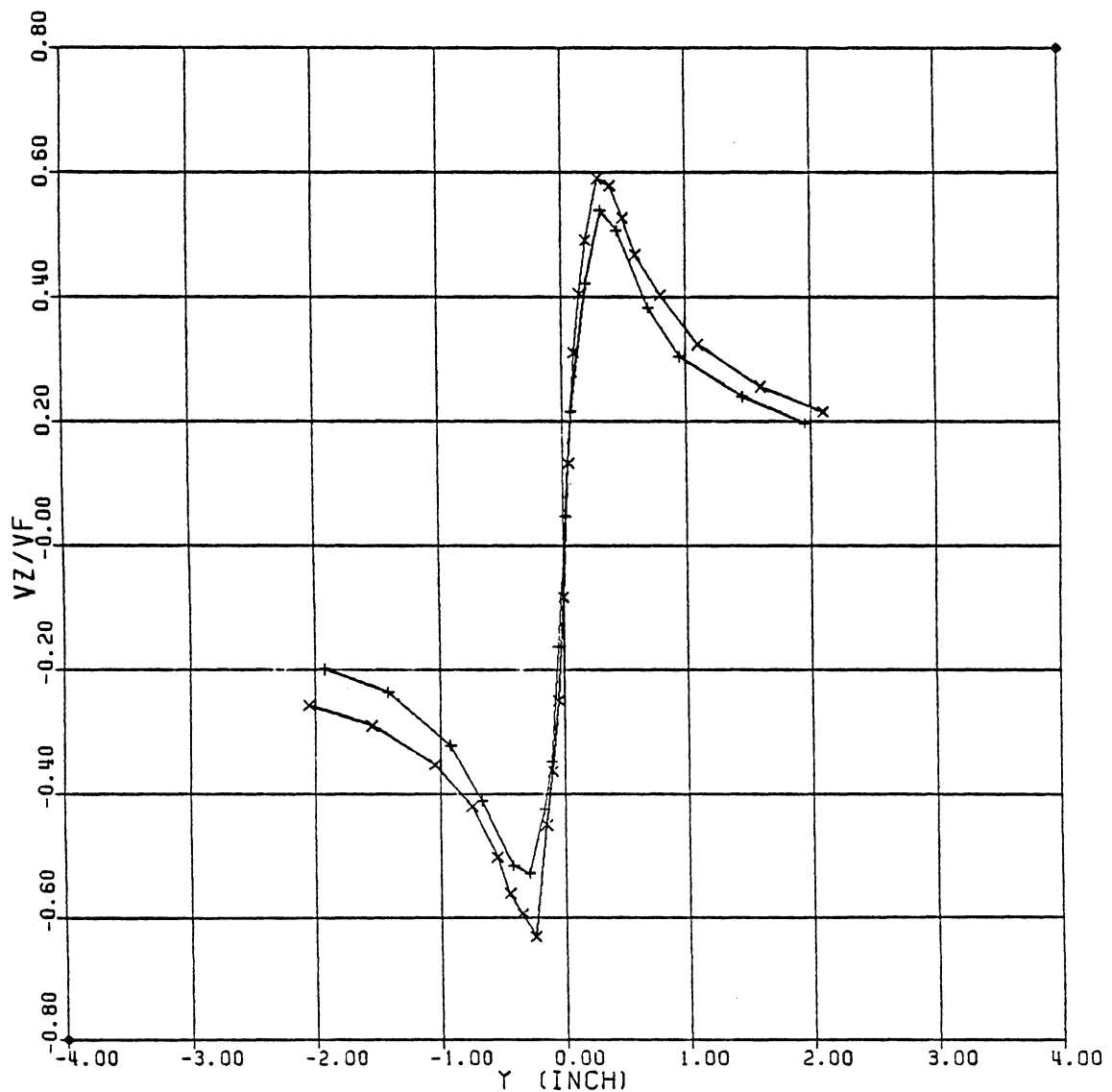
+ $V_\infty = 30 \text{ fps}$ \times 95 \diamond 220

STA 3 ALPHA = 5 DEG (HORIZONTAL SCAN)



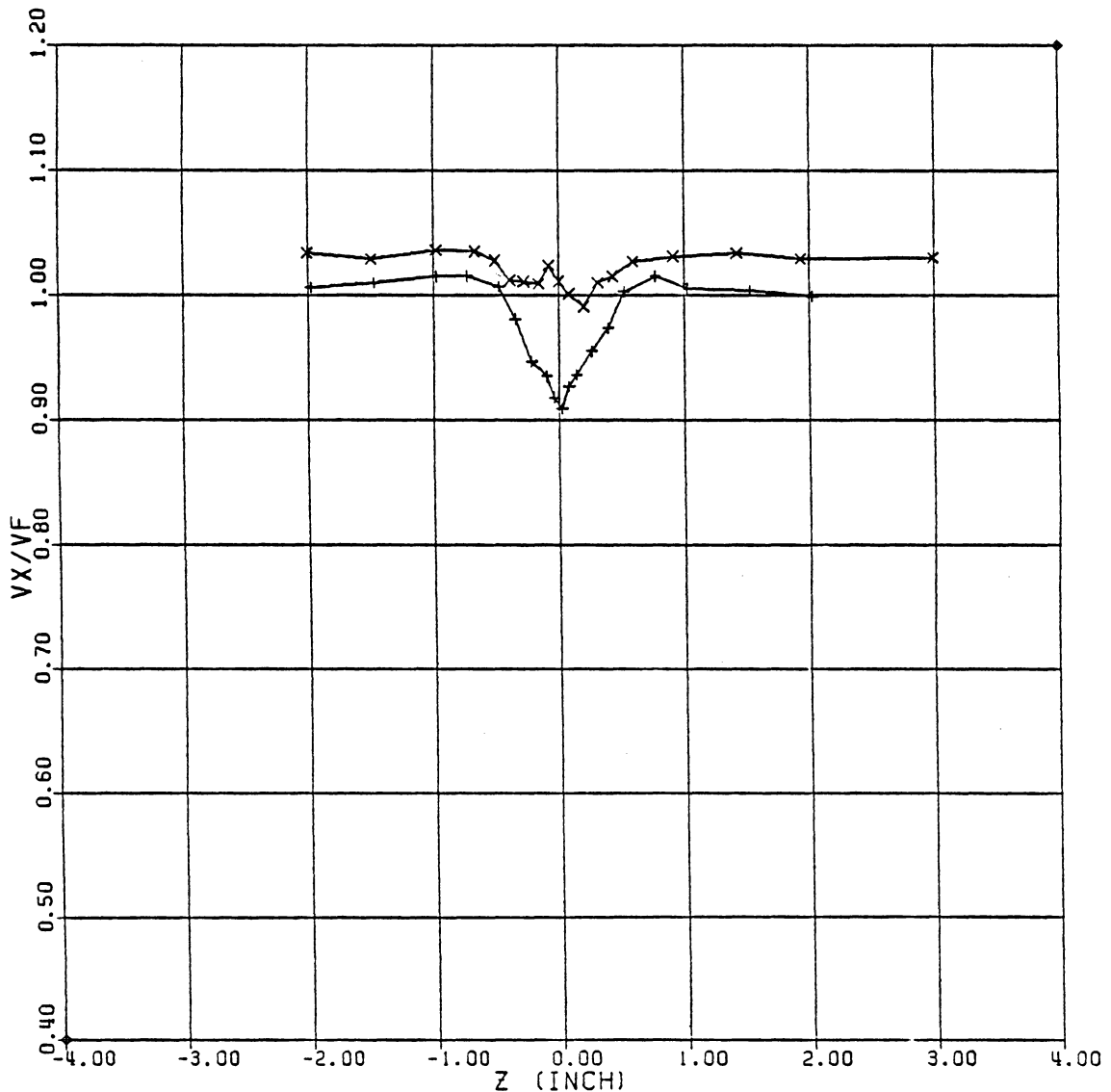
+ $V_\infty = 95$ fps
x 220

STA 3 ALPHA = 5 DEG (HORIZONTAL SCAN)



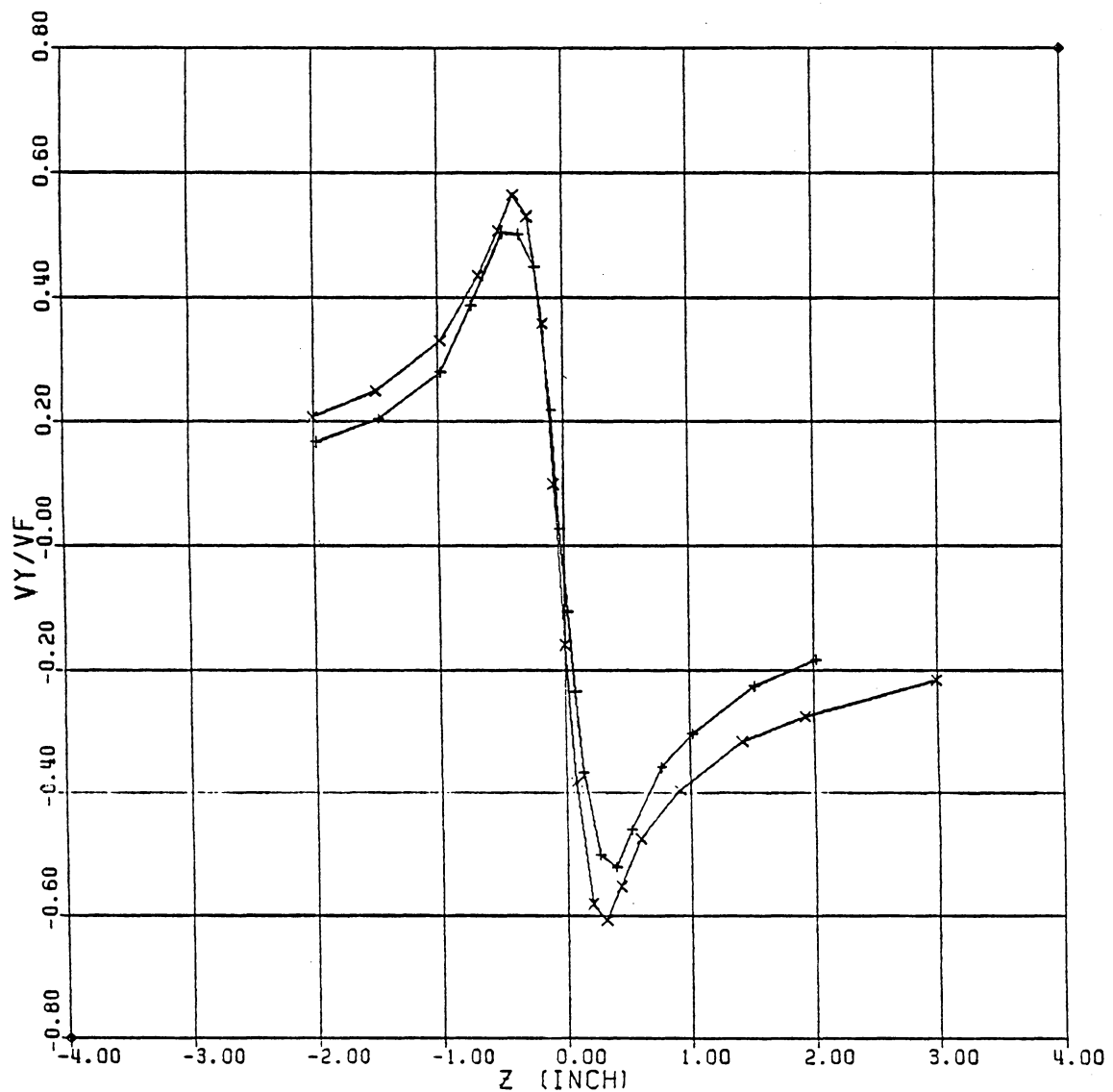
+ $V_\infty = 95$ fps
x 220

STA 3 ALPHA = 5 DEG (VERTICAL SCAN)



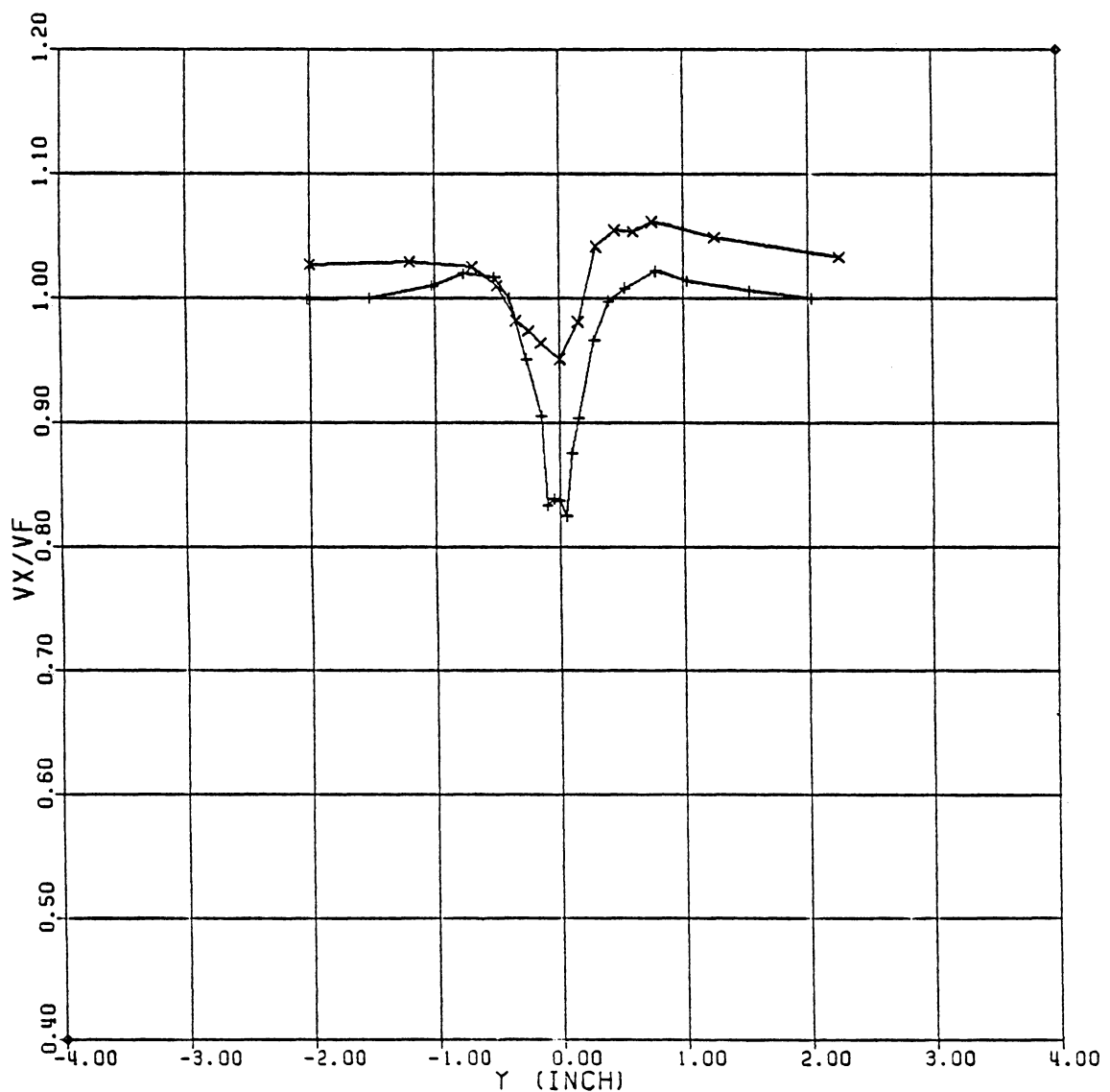
+ $V_\infty = 95$ fps
x 220

STA 3 ALPHA = 5 DEG (VERTICAL SCAN)



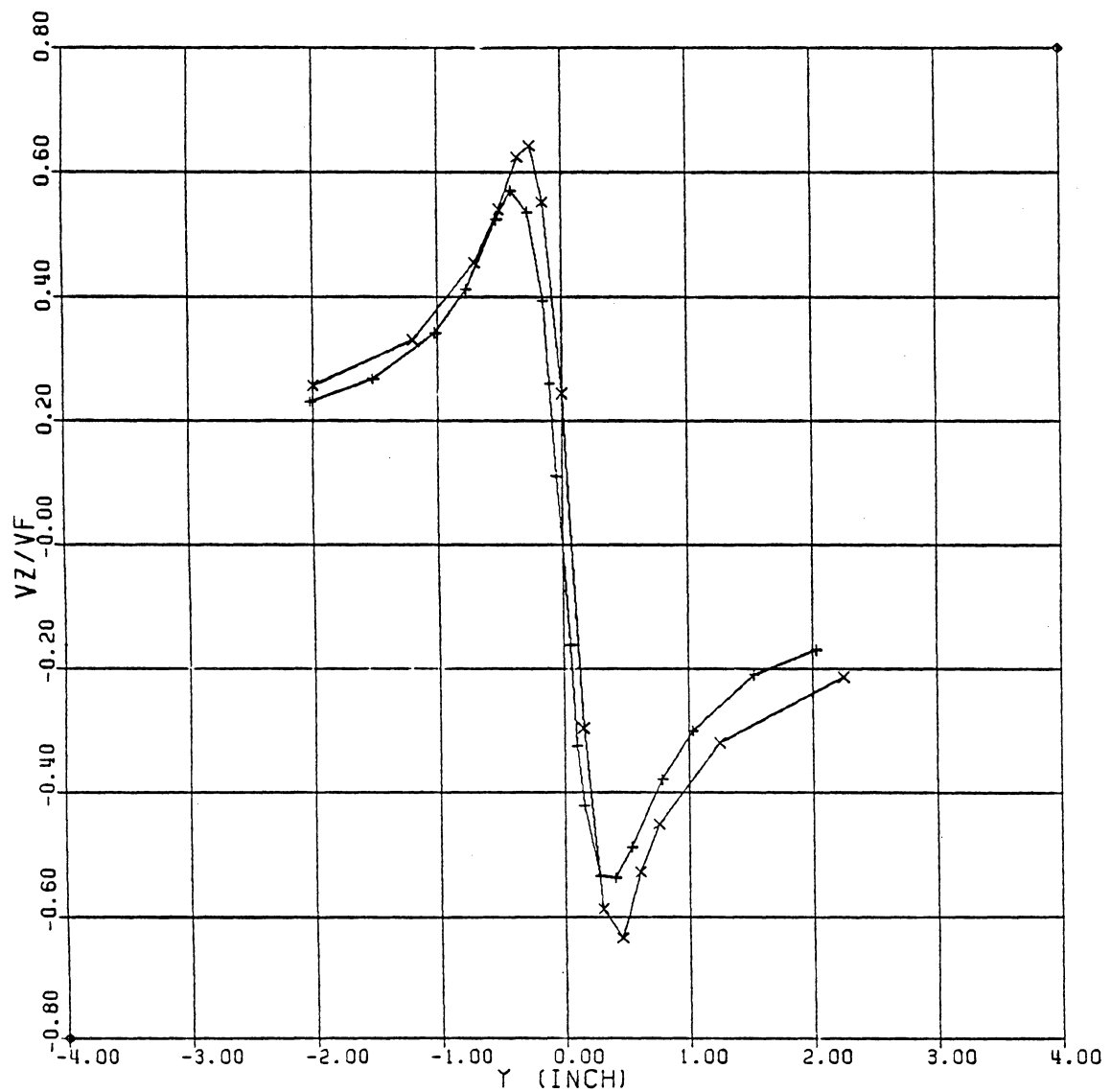
+ $V_\infty = 95$ fps
x 220

STA 3 ALPHA = -10 DEG (HORIZONTAL SCAN)



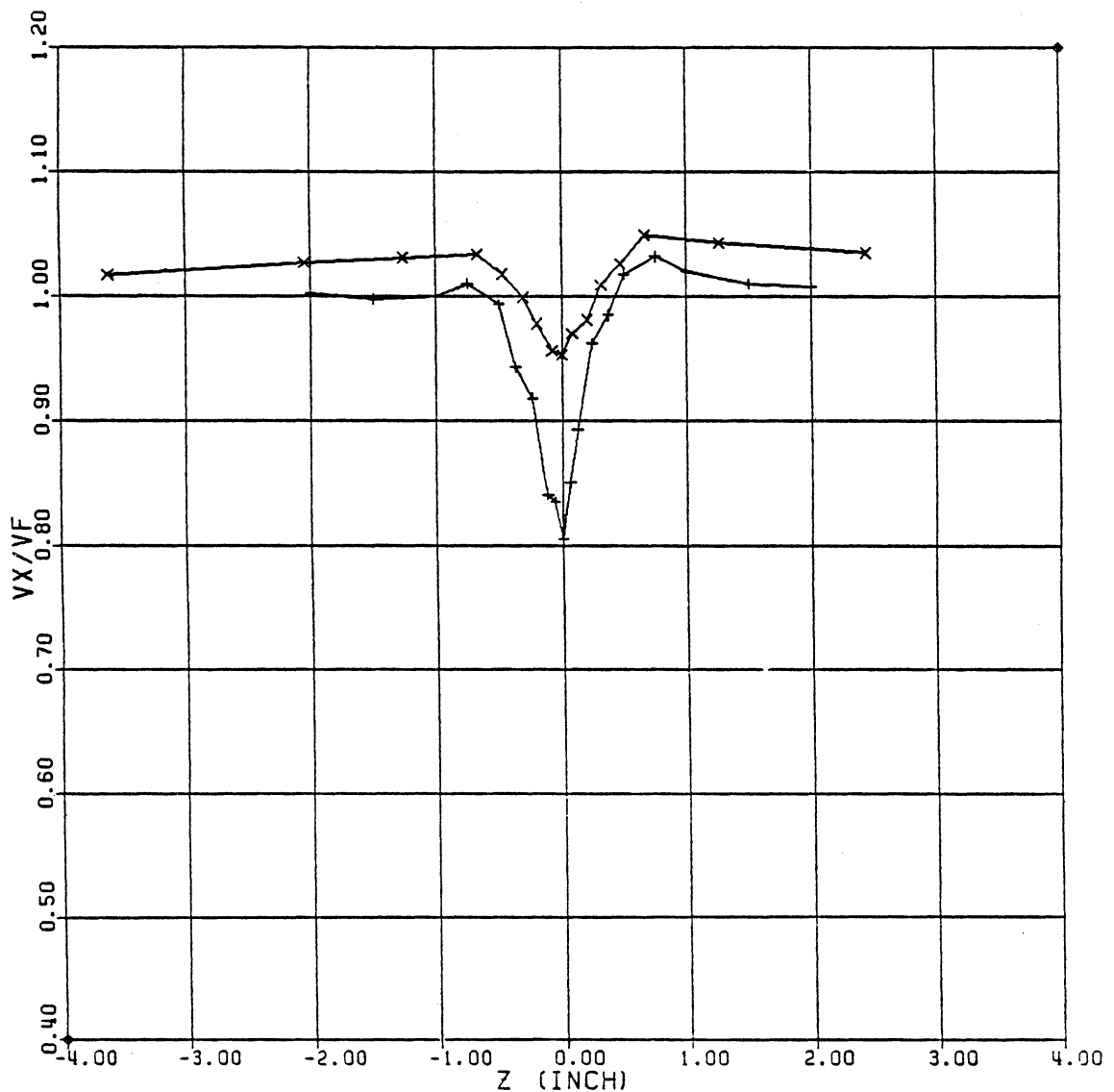
+ $V_\infty = 95 \text{ fps}$
x 220

STA 3 ALPHA = -10 DEG (HORIZONTAL SCAN)



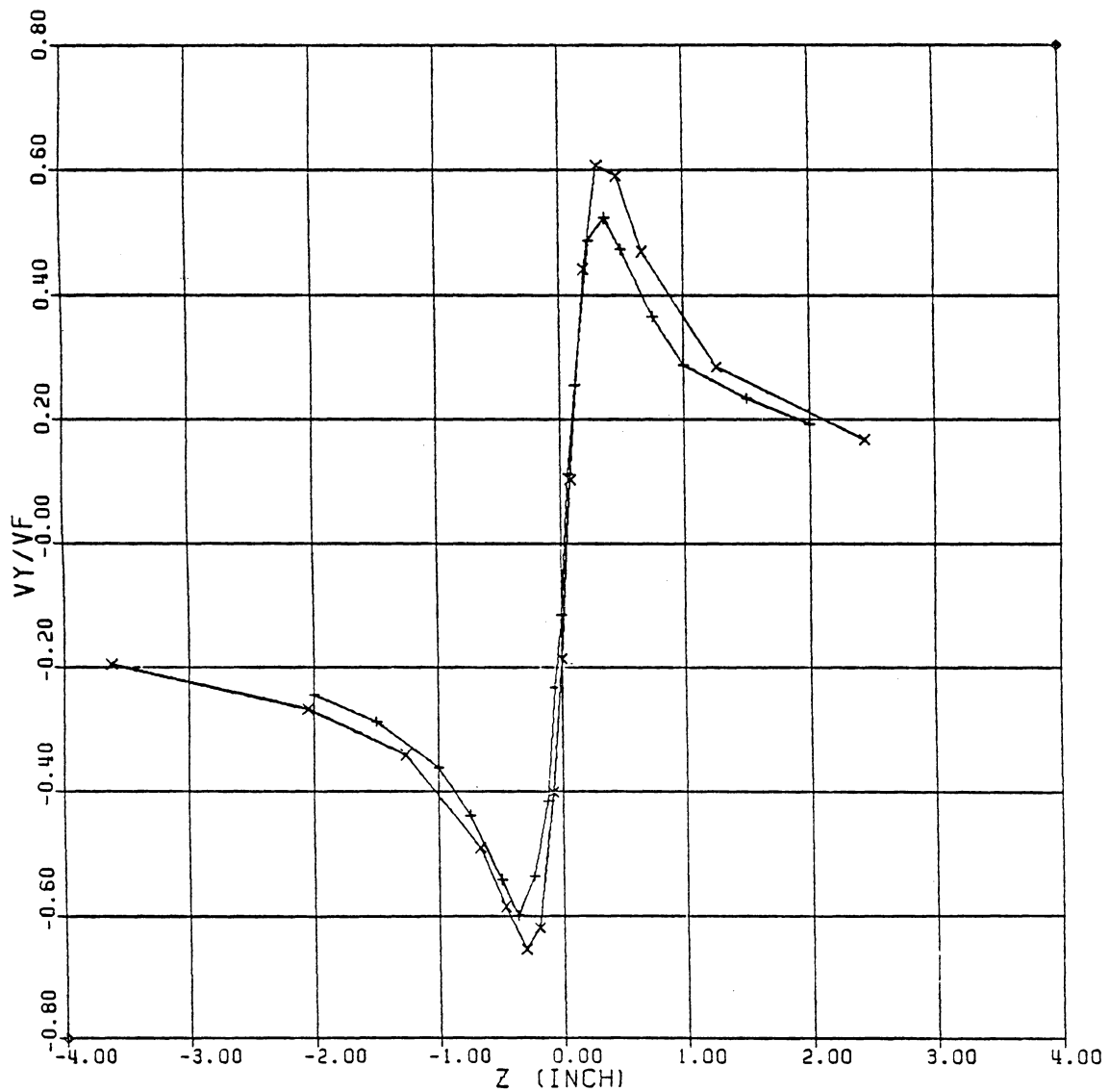
+ $V_\infty = 95$ fps
x 220

STA 3 ALPHA = -10 DEG (VERTICAL SCAN)



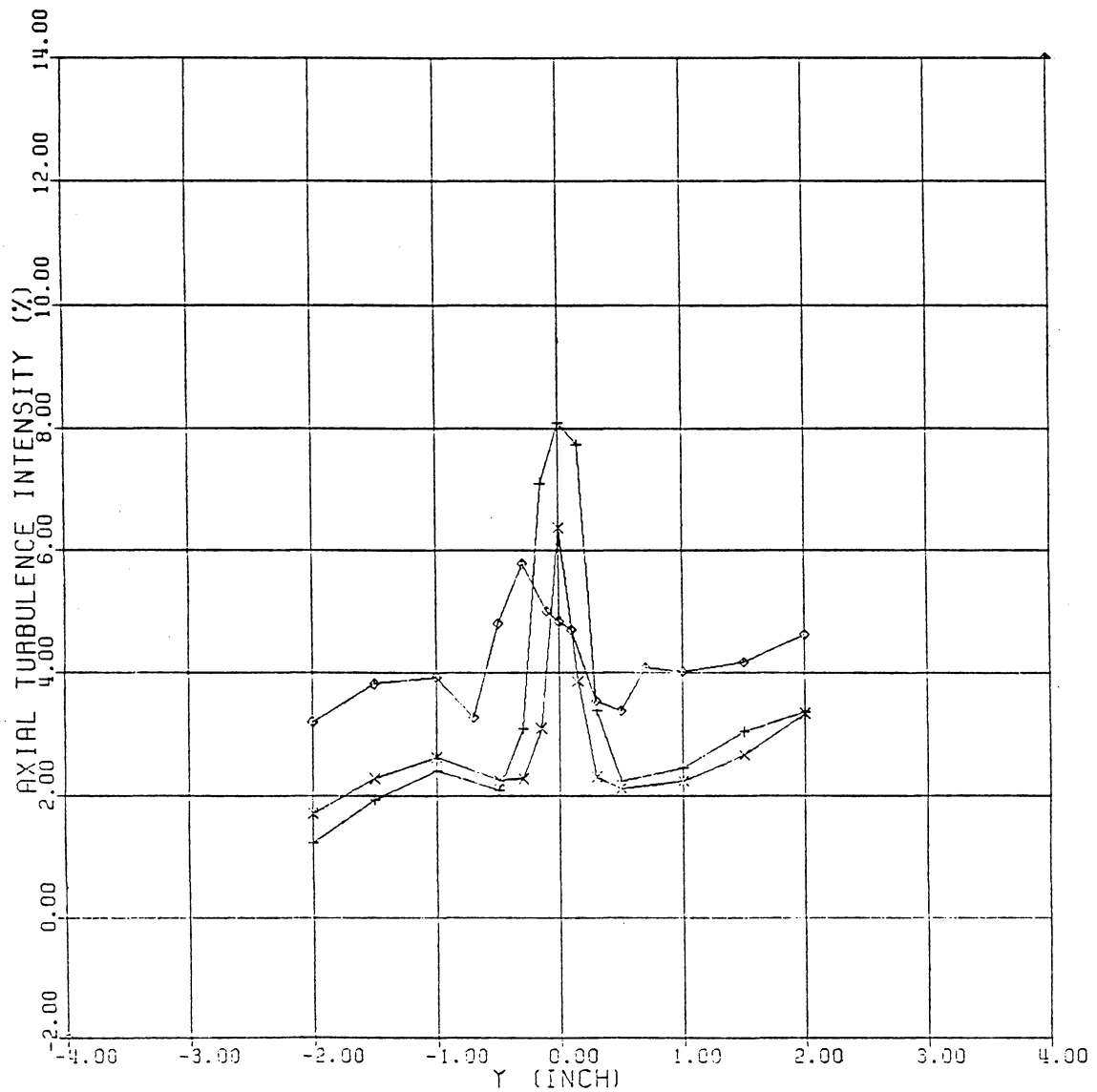
+ $V_\infty = 95$ fps
x 220

STA 3 ALPHA = -10 DEG (VERTICAL SCAN)

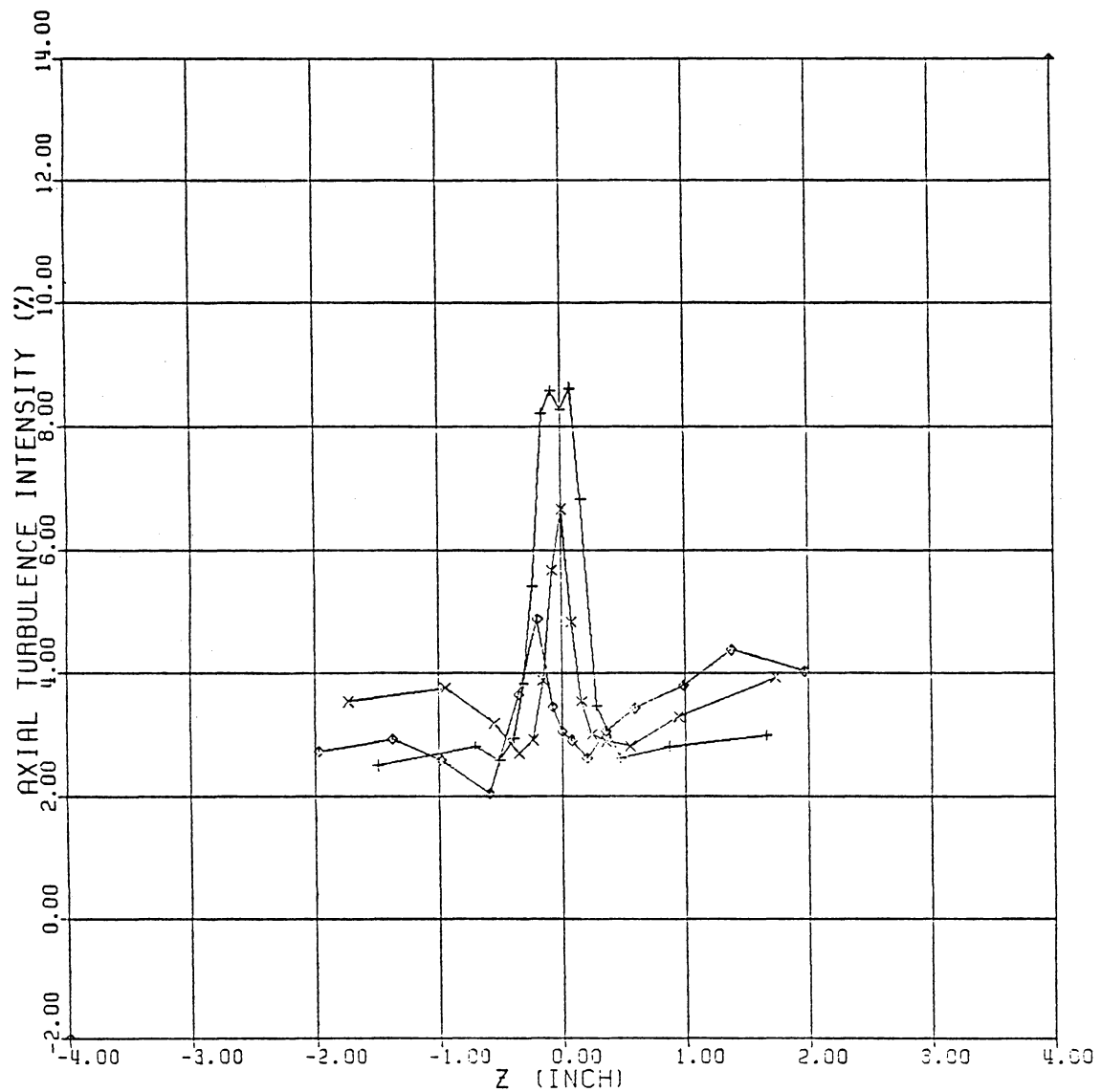
+ $V_\infty = 95$ fps

x 220

STA 1 ALPHA = 5 DEG (HORIZ. SCAN : VERT. WIRE)

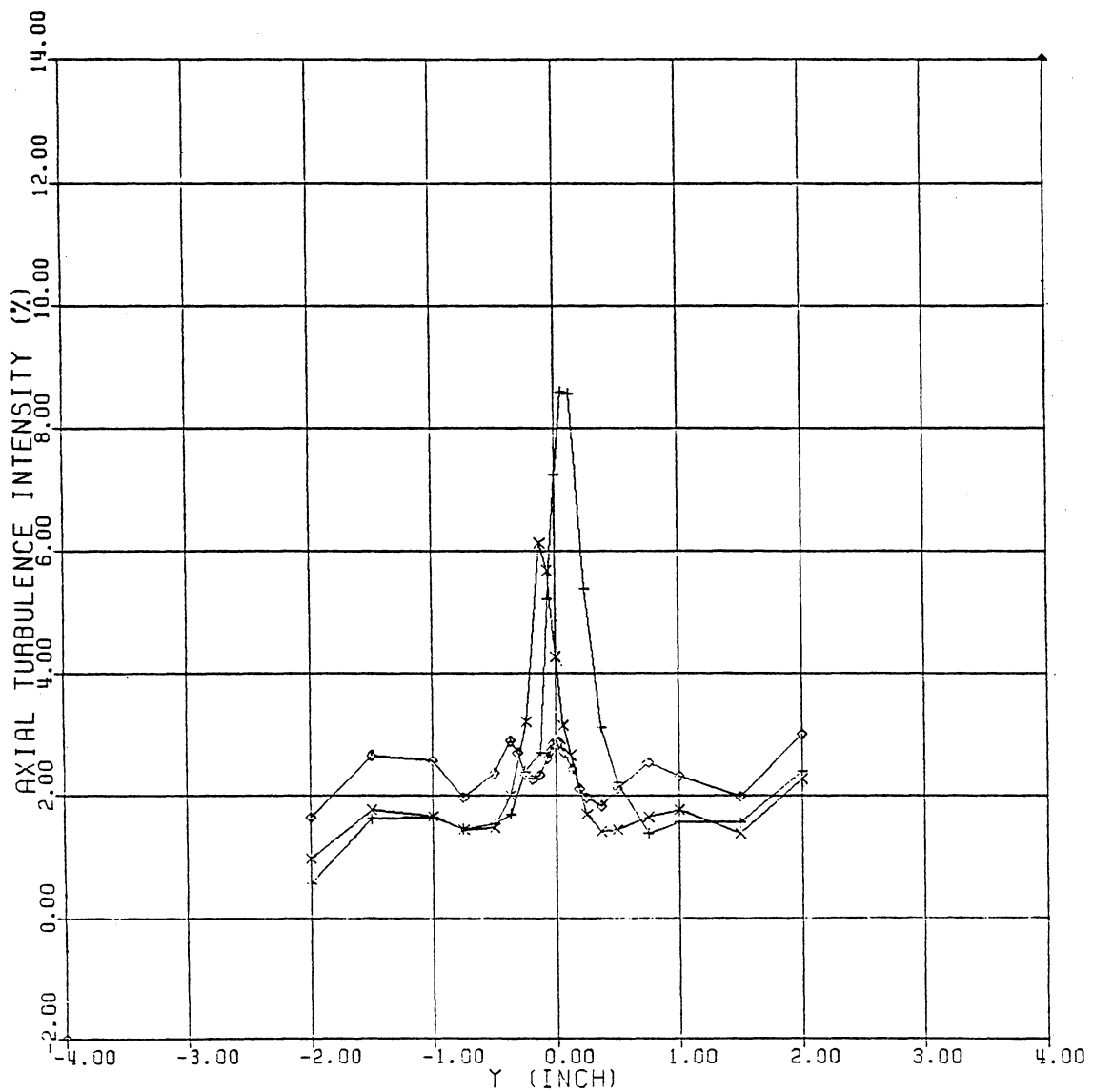
+ $V_\infty = 30$ fps \times 95 \diamond 220

STA 1. ALPHA = 5 DEG (VERT. SCAN : HORIZ. WIRE)



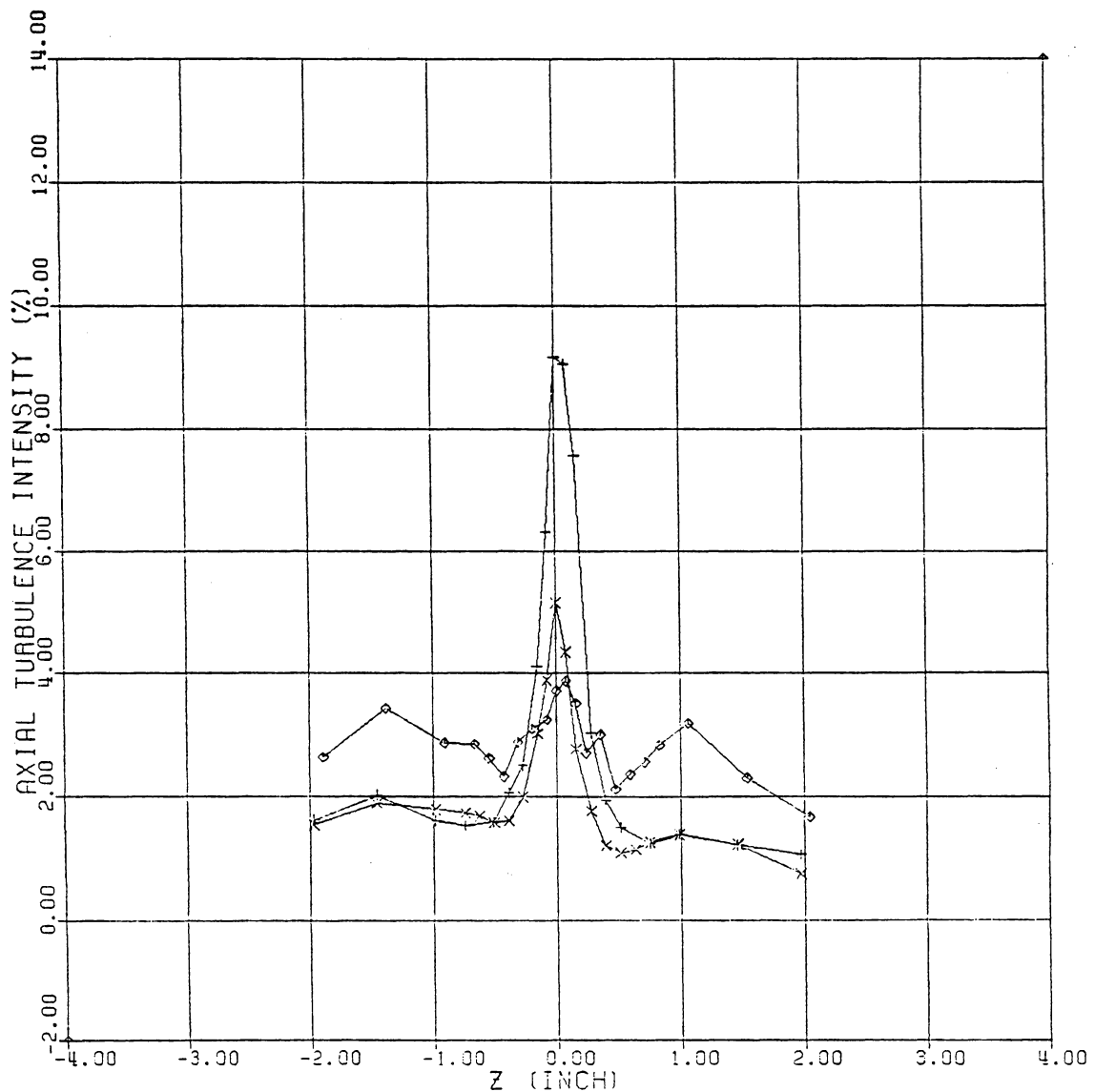
+ $V_\infty = 30$ fps
x 95
◊ 220

STA 1 ALPHA = -10 DEG (HORIZ. SCAN : VERT. WIRE)



+ $V_\infty = 30$ fps
x 95
◊ 220

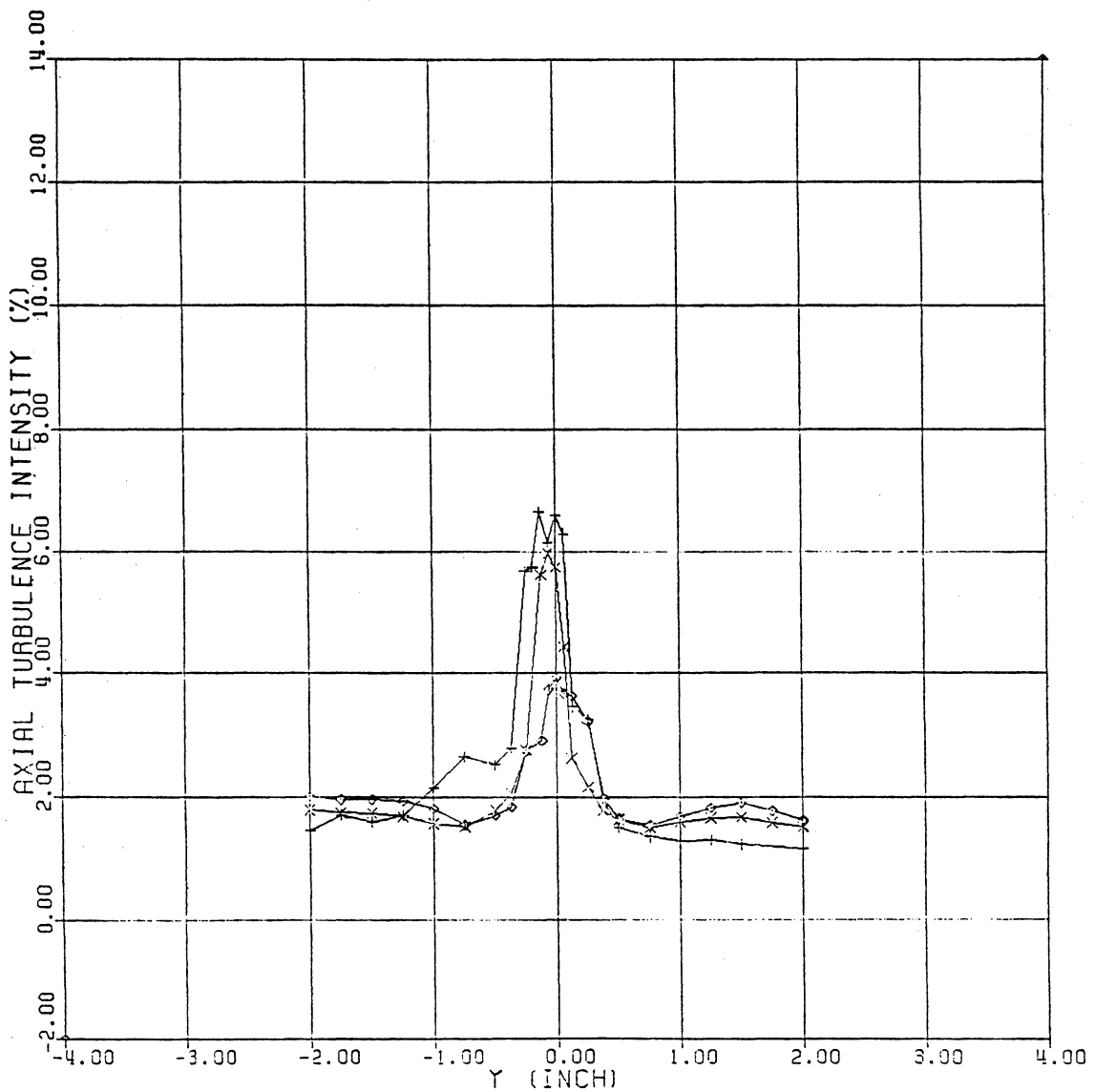
STA 1 ALPHA = -10 DEG (VERT. SCAN : HORIZ. WIRE)

+ $V_\infty = 30 \text{ fps}$

x 95

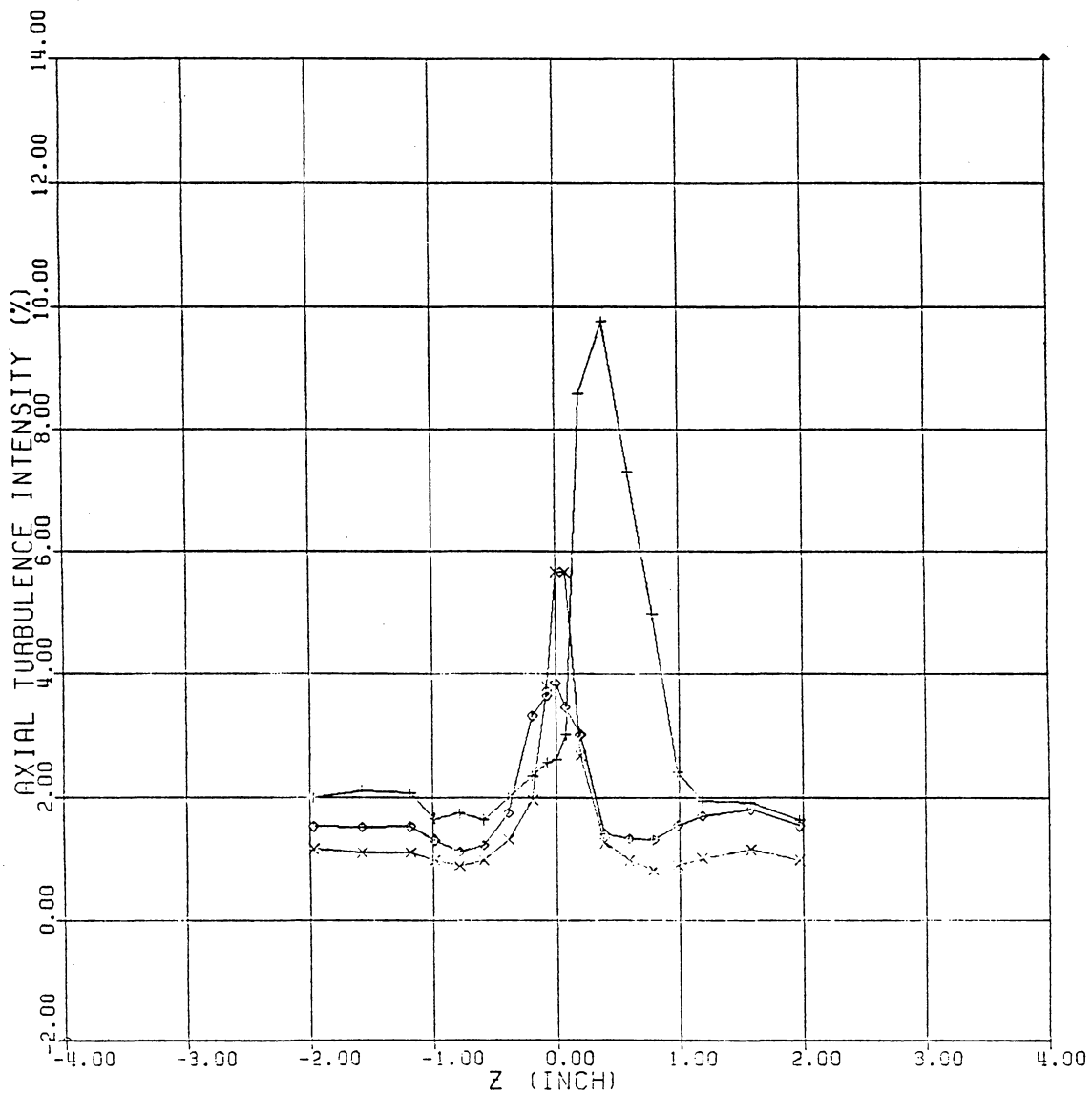
◊ 220

STA 2 ALPHA = -10 DEG (HORIZ. SCAN : VERT. WIRE)



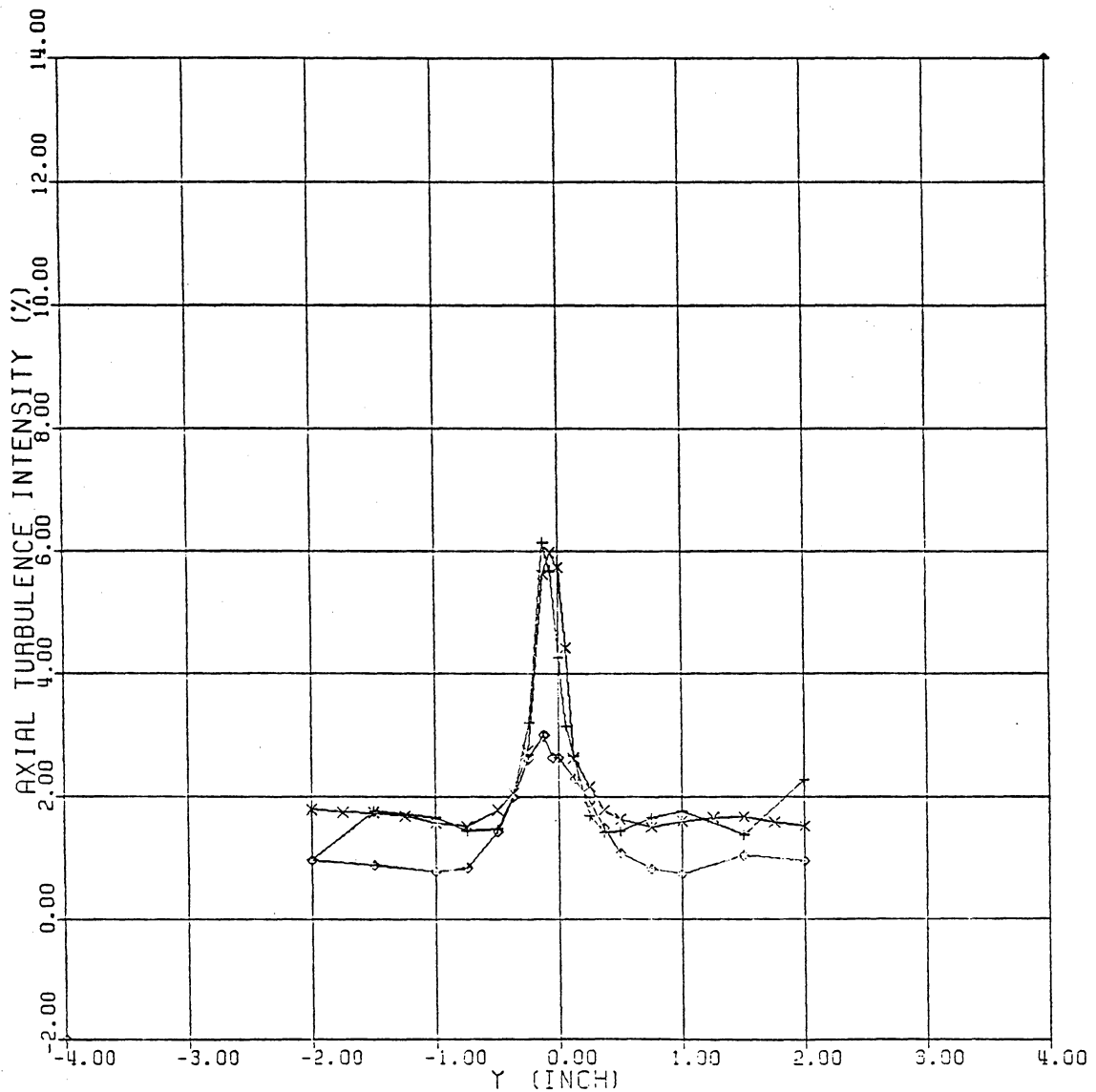
+ $V_\infty = 30 \text{ fps}$
x 95
◇ 220

STA 2 ALPHA = -10 DEG (VERT. SCAN : HORIZ. WIRE)



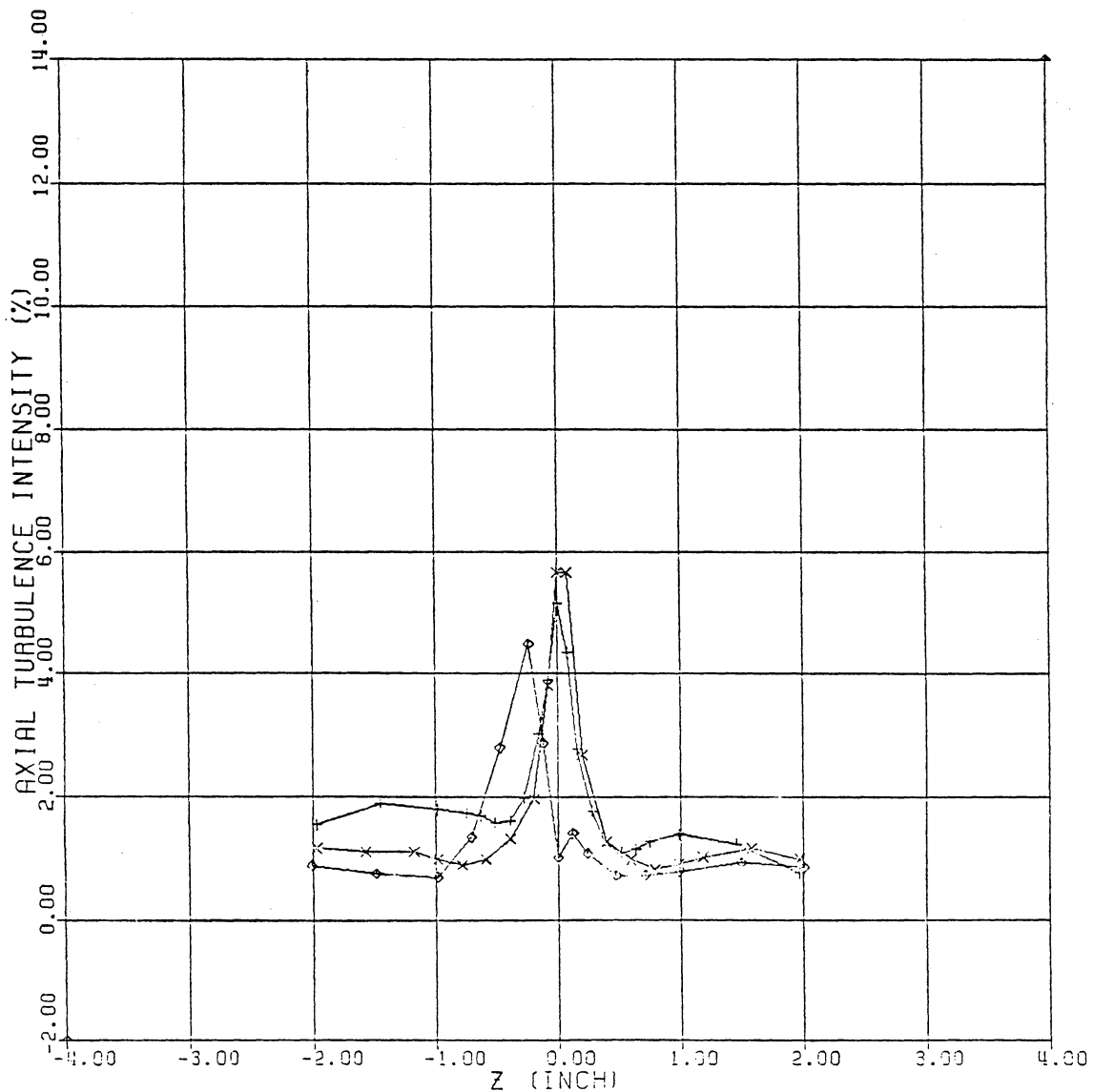
+ $V_\infty = 30 \text{ fps}$
x 95
◊ 220

$Q = 2.0$ $\text{ALPHA} = -10 \text{ DEG}$ (HORIZ. SCAN : VERT. WIRE)



+ $x/c = 3$
x 6
◊ 9

$Q = 2.0$ $\text{ALPHA} = -10 \text{ DEG}$ (VERT. SCAN : HORIZ. WIRE)



+	$x/c = 3$
\times	6
\diamond	9

Appendix D

PROGRAM LISTING FOR FAR-FIELD COMPUTATION

PROGRAM FAR-FIELD

THIS PROGRAM COMPUTES THE FAR-FIELD DECAY OF
AN ISOLATED TRAILING VORTEX

CONFER CHAPTER III FOR DETAIL

**INPUT : VELOCITY AND AXIAL TURBULENCE INTENSITY PROFILES
AT AN INITIAL STATION
EDDY VISCOSITY COEFFICIENT (C)
NON-ISOTROPY CONSTANT (STHETA)
DISSIPATION COEFFICIENT (CD)**

**OUTPUT : VELOCITY COMPONENTS AND AXIAL TURBULENCE INTENSITY
AT SPECIFIED DOWNSTREAM STATIONS**

* VARIABLES ARE DEFINED EXACTLY AS THEY ARE READ EXCEPT:

ATI	: AXIAL TURBULENCE INTENSITY
CORE	: L (LENGTH SCALE)
DIF	: DIFFUSION TERM IN TKE EQUATION
DIS	: DISSIPATION TERM IN TKE EQUATION
E	: EPSILON (EDDY VISCOSITY)
PRO	: PRODUCTION TERM IN TKE EQUATION
S	: SIGMA
TKE	: K (TURBULENT KINETIC ENERGY)
XCON	: AXIAL STEP SIZE CONTROL
()N	: INDICATES REVISED VALUES
()P	: INDICATES PRINTING VALUES

```

IMPLICIT REAL*8 (A-H,O-Z)
REAL*4 XP,RP,UP,VP,WP,ATIP,WMAXP,COREP
REAL*8 NU
DIMENSION R(50), U(50), V(50), W(50), ATI(50)
DIMENSION WR(50), WRR(50), WX(50)
DIMENSION XI(50), XIR(50), XIRR(50), XIX(50)
DIMENSION TKE(50), TKER(50), TKERR(50), TKEX(50)
DIMENSION E(50), ER(50), ERR(50), EX(50), ETHETA(50)
DIMENSION PSI(50), PSIN(50), DIF(50), PRO(50), DIS(50)
DIMENSION RP(50), UP(50), VP(50), WP(50), ATIP(50)
DIMENSION XPRINT(20)

I IS X-COUNTER
J IS R-COUNTER

K IS USED FOR PRINT CONTROL

READ (3,1) IMAX,JR
READ (3,2) CPRIME,STHETA,CD
READ (3,2) VF,XCON

```

```

      READ (3,3) KPRINT
      DO 8 K=1,KPRINT
 8 READ (3,5) XPRINT(K)
      WRITE (6,6) VF,CPRIME,STHETA,CD,XCON
      NU=1.6D-4
      SK=0.7D0
      J1=JR-1
      DR=0.2D0/JR
      TDR=2.0D0*DR
      DR2=DR*DR

C
C      READ IN INITIAL CONDITIONS
C
C      DO 100 J=1,JR
      READ (5,10) R(J),U(J),V(J),W(J),ATI(J)
      TKE(J)=1.5D0*(VF*ATI(K))**2
 100 CONTINUE
      PSI(1)=0.0D0
      DO 110 J=2,JR
      PSI(J)=PSI(J-1)+(U(J)*R(J)+U(J-1)*R(J-1))*DR/2.0D0
 110 CONTINUE
      DO 120 J=2,J1
      XI(J)=(U(J+1)-U(J-1))/TDR
 120 CONTINUE
      XI(1)=0.0D0
      XI(JR)=2.0D0*XI(J1)-XI(J1-1)
      I=1
      K=1
      X=0.0D0
      DLDX=0.0D0

C
C      COMPUTATION BEGINS
C
C      1001 CONTINUE
      DO 200 J=2,J1
      IF(W(J).GT.W(J-1)) GO TO 200
      IF(W(J).LE.W(J-1)) JWMAX=J-1
      GO TO 210
 200 CONTINUE
 210 CONTINUE
      DO 220 J=2,J1
      IF(TKE(J).GT.TKE(J-1)) GO TO 220
      IF(TKE(J).LE.TKE(J-1)) TKEMAX=TKE(J-1)
      GO TO 230
 220 CONTINUE
 230 COREN=R(JWMAX)+(W(JWMAX-1)-W(JWMAX+1))/(W(JWMAX-1)+W(JWMAX+1))
&      -2.0D0*W(JWMAX))*DR/2.0D0
      C=CPRIME*VF/W(JWMAX)
      DX=XCON*DR2*VF/(NU+CPRIME*DSQRT(TKEMAX)*COREN)
      IF(I.GT.1) DLDX=(COREN-CORE)/DX

C
C      TKE EQUATION
C
C      DO 300 J=2,J1
      WR(J)=(W(J+1)-W(J-1))/TDR
      TKER(J)=(TKE(J+1)-TKE(J-1))/TDR
      TKERR(J)=(TKE(J+1)-2.0D0*TKE(J)+TKE(J-1))/DR2
      E(J)=C*DSQRT(TKE(J))*COREN
      ETHETA(J)=E(J)/STHETA
      DIF(J)=(NU+E(J)/SK)*(TKERR(J)+TKER(J)/R(J))
&          +E(J)*TKER(J)**2/(2.0D0*TKE(J)*SK)

```

```

PRO(J)=E(J)*XI(J)**2+ETHETA(J)*(WR(J)-W(J)/R(J))**2
DIS(J)=-CD*TKE(J)**1.5/COREN
TKEX(J)=(-V(J)*TKER(J)+DIF(J)+PRO(J)+DIS(J))/U(J)
EX(J)=E(J)*TKEX(J)/(2.0D0*TKE(J))+E(J)*DLDX/COREN
300 CONTINUE
E(1)=C*DSQRT(TKE(1))*COREN
E(JR)=E(J1)
EX(1)=EX(2)
EX(JR)=EX(J1)
DIS(1)=-CD*TKE(1)**1.5/COREN
DIF(1)=(NU+E(1)/SK)*2.0D0*TKERR(2)
TKEX(1)=(DIF(1)+DIS(1))/U(1)
DO 400 J=2,J1
ER(J)=(E(J+1)-E(J-1))/TDR
ERR(J)=(E(J+1)-2.0D0*E(J)+E(J-1))/DR2
400 CONTINUE
C
C
C      W AND XI EQUATIONS
C
C
DO 500 J=2,J1
WRR(J)=(W(J+1)-2.0D0*W(J)+W(J-1))/DR2
BUNW1=WR(J)-W(J)/R(J)
BUNW=WR(J)+BUNW1/R(J)
WX(J)=(-V(J)*(WR(J)+W(J)/R(J))+(NU+ETHETA(J))*BUNW
&           +ER(J)*BUNW1/STHETA)/(U(J)-EX(J))
XIR(J)=(XI(J+1)-XI(J-1))/TDR
XIRR(J)=(XI(J+1)-2.0D0*XI(J)+XI(J-1))/DR2
BUNXI=XIR(J)-XI(J)/R(J)
BUNXI1=XIRR(J)+BUNXI/R(J)
BUNXI2=XIR(J)+XI(J)/(2.0D0*R(J))
XIX(J)=(-V(J)*BUNXI-2.0D0*W(J)*WX(J)/R(J)
&           +(NU+E(J))*BUNXI1+2.0D0*ER(J)*BUNXI2
&           +ERR(J)*XI(J))/(U(J)-2.0D0*EX(J))
500 CONTINUE
C
C
C      PRINTING RESULTS AT SPECIFIED STATION
C
C
IF(X.LT.XPRINT(K)) GO TO 700
DO 600 J=1,JR
RP(J)=R(J)
UP(J)=U(J)
VP(J)=V(J)
WP(J)=W(J)
ATIP(J)=DSQRT(TKE(J)/1.5D0)/VF
600 CONTINUE
WMAXP=W(JWMAX)
COREP=COREN*12.0
XP=X
WRITE (6,20) I,XP,DX,COREP,WMAXP
DO 610 J=1,J1
WRITE (6,30) J,RP(J),UP(J),VP(J),WP(J),ATIP(J)
610 CONTINUE
K=K+1
IF (I.GT.IMAX) GO TO 1000
IF (K.GT.KPRINT) GO TO 1000
C
C
C      REVISION OF VARIABLES
C
C
700 CONTINUE
I=I+1
X=X+DX

```

```

CORE=COREN
DO 800 J=2,J1
W(J)=W(J)+WX(J)*DX
XI(J)=XI(J)+XIX(J)*DX
TKE(J)=TKE(J)+TKEX(J)*DX
800 CONTINUE
W(1)=0.0D0
W(JR)=W(J1)*R(J1)/R(JR)
XI(1)=0.0D0
XI(JR)=XI(J1)+XIR(J1)*DR
TKE(1)=TKE(1)+TKEX(1)*DX
TKE(2)=TKE(1)-(TKE(1)-TKE(3))/4.0D0
TKE(JR)=TKE(J1)

C
C      INTEGRATION OF XI TO GET U (START FROM FREESTREAM) AND
C      INTEGRATION OF U TO GET PSI (START FROM AXIS)
C
C      U(JR)=VF
V(1)=0.0D0
PSIN(1)=0.0D0
DO 900 J=1,J1
KK=JR-J
U(KK)=U(KK+1)-(XI(KK)+XI(KK+1))*DR/2.0D0
900 CONTINUE
DO 910 J=2,JR
PSIN(J)=PSIN(J-1)+(U(J)*R(J)+U(J-1)*R(J-1))*DR/2.0D0
V(J)=-(PSIN(J)-PSI(J))/(R(J)*DX)
PSI(J)=PSIN(J)
910 CONTINUE
GO TO 1001
1000 CONTINUE
C
C
1 FORMAT(2I5)
2 FORMAT(3F10.0)
3 FORMAT(15)
5 FORMAT(F10.0)
6 FORMAT(10X,'VF = ',F5.2,5X,'CPRIME = ',F7.4,5X,'STHETA = ',F5.1,
&                                5X,'CD = ',F5.2,5X,'XCON = ',F5.2)
10 FORMAT(10X,5F10.0)
20 FORMAT(//,10X,'I = ',15,5X,'X = ',F7.1,' + ',F5.2,5X,
&                                'CORE = ',F5.2,' INCH',5X,'WMAX = ',F5.2,//,
&                                5X,'J ',6X,'R ',10X,'U ',10X,'V ',10X,'W ',10X,'ATI ',/)
30 FORMAT(1X,15,5D11.4)
STOP
END

```

**The vita has been removed from
the scanned document**

COMPUTATIONAL AND EXPERIMENTAL STUDY OF TRAILING VORTICES

by

Heehwan Lee

(ABSTRACT)

A coordinated computational and experimental study was undertaken to investigate the behavior of the vortices trailing from low aspect ratio lifting surfaces. Vortex formation in the near-wake was measured in a wind tunnel with yaw-head and hot-wire probes at three different Reynolds numbers, the highest of which was greater than most previous studies. These near-wake measurements provided initial conditions for the far-field computation with the parabolized Navier-Stokes equations written in terms of vorticity and stream function. Turbulent transport was modeled through the turbulent kinetic energy and the Prandtl-Kolmogorov hypothesis to give an eddy viscosity. The experimental results showed that the effects of Reynolds number are significant for vortex formation in the near-wake, and the computation adequately predicted these effects. However, the decay trend in the far-field is essentially unaffected by the Reynolds number, and the predicted decay for maximum tangential velocity agreed very well with Iversen's correlation.